

CODED APERTURE PHASE CONTRAST TOMOSYNTHESIS

By

MAGDALENA BOGUMILA SZAFRANIEC



Supervisors:

Dr Alessandro Olivo

Professor Robert Speller

A THESIS SUBMITTED TO THE UNIVERSITY OF LONDON
FOR THE DEGREE OF DOCTOR OF PHILOSOPHY
DEPARTMENT OF MEDICAL PHYSICS AND BIOENGINEERING
UNIVERSITY COLLEGE LONDON

2013

Abstract

X-ray Phase Contrast (PC) Imaging has the potential to greatly improve radiography. Conventional radiography is based on the imaginary part of the refractive index, whereas PC imaging is based on the unit decrement of the real part, which can be up to 1000 times larger. This is particularly important in soft tissue imaging (e.g. mammography), where the differences in the imaginary part of the refractive index are small. Combining PC with tomosynthesis (TS) would also allow for the differentiation of overlapping tissues, thus leading to improved detection of breast lesions. Coded Aperture X-ray Phase Contrast Imaging (CAXPCi) is a technique which enables PC imaging with conventional lab sources, and which could thus be translated into a clinical environment. In this work the feasibility of a combined CAXPCi/Tomosynthesis approach is demonstrated, both on simulated and experimental data. The results of the simulations of the phase contrast signal in TS geometry are in good agreement with the experimental data. The simulator can be used in the future to understand and predict the phase contrast signal for other 3D implementations of phase contrast imaging. The implementation of the new method in the laboratory conditions is presented and four tomosynthesis reconstruction algorithms are proposed and compared: filtered backprojection (FBP), separable paraboloidal surrogates (SPS), conjugate gradient (CG) and penalized conjugate gradient (penalized-CG). The analytical reconstruction (FBP) of the phase contrast data results in noisy images. This can be greatly improved by using iterative statistical methods (SPS, CG and penalized CG), at a cost of a decreased image contrast but with an overall benefit in terms of contrast to noise ratio. CAXPCi Tomosynthesis scans of various samples, including a sample containing two superimposed TORMAM phantoms as well as breast biopsy samples, were carried out to evaluate the method's performance under realistic mammographic conditions. Strong phase contrast (PC) signal was observed in all reconstructions, and the overlapping structures were effectively separated.

Key words: Coded Aperture Phase Contrast Imaging, Tomosynthesis, flat panel x-ray detector, reconstruction, dosimetry.

I, Magdalena Bogumila Szafraniec, confirm that the work presented in this thesis is my own. Where information has been derived from other sources, I confirm that this has been indicated in the thesis.

Signed

Acknowledgments

First of all, I wish to thank my supervisors Dr Alessandro Olivo, Professor Robert Speller and Steve Naday for their continued support and academic guidance over the course of this thesis. The experience I have gained under their supervision is highly valuable and will benefit me in the future career in medical physics. I would like to thank them for the opportunity of witnessing the Coded Apertures Phase Contrast Imaging technique to be developed and improved over the last three years. Furthermore, I wish to express my gratitude for letting me to work on two imaging techniques simultaneously – Coded Aperture Phase Contrast Imaging and digital breast Tomosynthesis, which made my work diverse and fulfilling.

Special thanks go to Spencer Gunn from Dexela Ltd., John Hipwell and Martin Schweiger from UCL CMIC for their ongoing help and patience while working on the image reconstruction. I am grateful for their time and effort, as well as for the enlightening suggestions.

Most of my PhD project has taken place in the lab. Anastasios Konstantinidis and Charlotte Hagen – thank you for the long hours spent together in the lab doing the measurements and experiments. You are not only bright scientists but also very good friends. I would like to thank especially Anastasios for sharing with me his broad knowledge on detector characterization and for his contributions to this work.

I owe huge thank you to Konstantin Ignatyev and Peter Munro for the endless discussions about the phase contrast imaging. Thank you for your support and for the valuable advice.

I want to thank Dexela's team: Ed Bullard, Roland Neal, Eoin O'Tuairisg, Alan McArthur, Hamdan Amin and James Broderick for their help while starting my PhD, as well as for their continuous technical support until the end of the project.

Without the love and support of my parents, my sister Marta, and my brother Michal, as well as, without the true encouragement from my fiancé, Konrad Szalinski, this thesis could simply not be finished. They have always been great to me and during the last three years they have done their best to keep me on track.

And last, but certainly not least, I want to thank, Andria Hadjipanteli, Marco Endrizzi, Paul Diemoz, Cesar Zapata, Christiana Christodoulou, Dan O'Flynn, Tom Millard, Paul Doolan, Spyros Gkoumas, Essam Banoqitah, Ireneos Drakos, George Randall, Kate Ricketts, Ben Price and Caroline Reid, for being fantastic friends.

Contents

Abstract	ii
Acknowledgments.....	iv
Contents	v
List of Figures	ix
List of Tables.....	xv
Glossary of Terms	xvi
1 Introduction	18
1.1 Current state and limitations of a conventional breast imaging	18
1.2 Project motivation.....	21
1.3 Key contributions made to the field.....	23
1.4 Thesis overview	25
2 Theory	26
2.1 Phase Contrast Imaging	26
2.1.1 Introduction to Phase Contrast Imaging	26
2.1.1.1 Conventional radiography vs. Phase Contrast imaging	26
2.1.1.2 Theoretical approaches in phase Contrast imaging.....	29
2.1.1.3 Edge enhancement	32
2.1.2 Generation of phase contrast effects.....	33
2.1.2.1 Free space propagation	34
2.1.2.2 Bonse/Hart interferometer	34
2.1.2.3 Diffraction Enhanced/Analyzer based imaging	35
2.1.2.4 Talbot/Lau interferometer	36
2.1.3 Coded Apertures Phase Contrast Imaging.....	37
2.1.3.1 Edge illumination method.....	37
2.1.3.2 Coded Apertures Phase Contrast Imaging	38
2.1.3.3 Source size and coherence requirement	41
2.2 Digital Tomosynthesis	42
2.2.1 Introduction	42
2.2.2 Geometry.....	43

2.2.3	Reconstruction methods	46
2.2.3.1	Analytical reconstruction.....	46
2.2.3.2	Iterative reconstruction	53
2.2.3.3	The choice of the best reconstruction algorithm.....	66
2.3	Image quality evaluation.....	67
2.3.1	Contrast-to-Noise Ratio (CNR).....	67
2.3.2	Artefact Spread Function (ACR).....	67
3	Detector performance evaluation	69
3.1	Introduction and chapter overview	69
3.2	Flat panel detectors under investigation.....	70
3.2.1	Anrad SMAM.....	70
3.2.2	Dexela.....	71
3.2.3	Hamamatsu.....	72
3.2.4	Direct and indirect conversion	73
3.3	Optical characterization	73
3.3.1	Photon Transfer Curve	73
	Read noise.....	75
	Gain 75	
	Full well capacity.....	75
	Dynamic range	75
3.3.2	Experimental methods and results.....	76
3.4	X-ray characterization of the detectors	78
3.4.1	Modulation Transfer Function (MTF).....	78
3.4.2	Noise Power Spectrum (NPS)	81
3.4.3	Detective Quantum Efficiency (DQE)	84
3.5	Influence of the signal spill out on the phase contrast signal.....	91
3.6	Conclusions and choice of the detector for CAXPC Tomosynthesis	97
4	Comparison between the Free-space-propagation Phase Contrast Tomosynthesis and clinical Tomosynthesis.....	98
4.1	Introduction.....	98
4.2	Experimental methods	99
4.3	Results and discussion	102
4.4	Conclusions.....	108
5	Proof-of-concept results of Coded-Aperture Phase Contrast Tomosynthesis.....	109

5.1	Introduction and chapter overview	109
5.2	Setting up the Coded Apertures Phase Contrast system	110
5.2.1	X-ray source	110
5.2.2	Masks alignment.....	111
5.2.3	Dose measurements.....	115
5.3	Phase Contrast signal simulations.....	118
5.3.1	Planar simulation.....	118
5.3.1.1	Description of the simulators	118
5.3.1.2	Experimental conditions	122
5.3.1.3	Results and discussion	123
5.3.2	Tomosynthesis simulations	124
5.3.2.1	Description of the simulations	124
5.3.2.2	Experimental validation.....	124
5.4	Coded Apertures Phase Contrast Tomosynthesis	127
5.4.1	CAXPC Tomosynthesis of a “double” TORMAM phantom	127
5.4.2	Results of the clinical Tomosynthesis of the “double” TORMAM phantom.....	131
5.5	Summary and discussion.....	132
6	Comparison between different reconstruction algorithms	135
6.1	Introduction.....	135
6.2	Quantitative comparison between FBP, CG and SPS algorithms.....	138
6.2.1	CNR.....	138
6.2.2	ASF.....	139
6.2.3	Regularization study.....	140
6.2.4	Number of iterations.....	142
6.3	GPU vs. CPU implementation of the iterative methods	142
6.4	Optimization of the acquisition geometry.....	143
6.5	Optimization of the acquisition geometry.....	145
7	Proposed applications of the developed method.....	147
7.1	Mammography.....	147
7.2	Small animal imaging	148
8	Summary and suggestions for the future work	152
8.1	Summary and key contribution to the field.....	152
8.1.1	Choice of the detector for CAXPC Tomosynthesis	152
8.1.2	CSetting-up the CAXPC Tomosynthesis system and dose measurements.	153

8.1.3 Simulations of the phase contrast signal and their experimental verification	153
8.1.4 Imaging of complex samples.....	154
8.1.5 Comprehensive study of different reconstruction algorithms for the new method ...	154
8.2 Future work.....	155
References	157

List of Figures

Figure 1.1 A world map showing a standardized number of breast cancer per 100,000 people. Figure adopted from (Ferlay et al. 2010)	18
Figure 1.2 Incidence and mortality rate per 100,000 population. Figure adopted from (Ferlay et al. 2010)	19
Figure 1.3 Breast anatomy. 1 – chest wall, 2 – pectoralis muscles, 3 – lobules, 4 – nipple, 5 – areola, 6 – milk duct, 7 – fatty tissue, 8 – skin. Figure adopted from (Lynch 2009).	20
Figure 1.4 World map showing the major synchrotron sources around the world. Figure adopted from (www.diamond.ac.uk)	23
Figure 2.1 The real (f_1) and imaginary part (f_2) of the atomic scattering factor for PMMA, as a function of photon energy.	28
Figure 2.2 Phase contrast imaging geometry.	29
Figure 2.3 Mechanism of the phase contrast signal creation from an object with a circular cross-section. Due to the phase gradient at the edges of the detail, x-rays are refracted and change their original direction. The measured intensity profile shows loss in intensity in the forward direction, and an increase in the direction corresponding to the refraction angle. Note that the refraction angles have been highly exaggerated for easiness of display.	33
Figure 2.4 Schematic of a fundamental idea of the free space propagation technique. The setup used to image the sample (red), consists only of a detector (green) with suitable spatial resolution. On the image, different positions of the detector are shown and corresponding PC signals.....	34
Figure 2.5 Schematic of a fundamental idea of the interferometric technique. The setup, which is used to scan a sample (red), consists of 3 crystals (grey) and a detector (green).	35
Figure 2.6 Schematic of the Analyser based PC technique. The setup used to image the sample (red) consists of an “analyser” crystals (grey) placed between the sample, and the detector (green). An additional crystal (the monochromator, not shown in the picture) must be present upstream of the sample to provide the necessary degree of temporal coherence. ...	36
Figure 2.7 Schematic of the grating-based PC method. The setup used to image the sample (red) consists of 3 gratings (purple), one before the sample (G1) and two behind the sample (G2 and G3) and a detector (green).	37
Figure 2.8 Schematic of the basic principle of the edge illumination technique.	38
Figure 2.9 Coded Aperture Phase Contrast setup. Dotted arrows indicate photon directions in the absence of the sample.....	39

Figure 2.10 Phase Contrast signal of a 100 μ m wire obtained at 40keV with the experimental setup shown in Figure 5. Dots describe the experimental data while solid line is the simulated data.	39
Figure 2.11 Full illumination (a) and no illumination (b) of the detector.	40
Figure 2.12 Effect of partial pixel illumination on the simulated PC signal (left) of a 100 μ m polyethylene fibre and the corresponding illumination conditions (right). The solid, dashed and dotted line of the acquired signal corresponds to illumination of the full pixel (fullbeam), half of the pixel (“half” beam) and a quarter of the pixel (“quarter” beam). Figure adopted from (Olivo and Speller 2008).	41
Figure 2.13 Schematic of the tomosynthesis scan (a) and its limitations (b).....	43
Figure 2.14 Tomosynthesis geometries. (a) parallel opposing motion of the x-ray source and the detector, (b) complete isocentric motion with an isocenter located in the centre of the patient, (c) partial isocentric motion, in which the x-ray tube is rotated within angular range and the detector moves in one plane, (d) partial isocentric motion, in which the detector remains stationary while the x-ray tube moves around a central axis with an isocenter located above the patient (Figures a, b and c adopted from (Dobbins and Godfrey 2003) and figure d adopted from (Niklason et al. 1997)).	44
Figure 2.15 Tomosynthesis geometry using a complete isocentric motion (a) and geometric configuration for transforming the complete isocentric geometry into planar Tomosynthesis reconstruction (Figures a adopted from (Dobbins and Godfrey 2003) and figure b adopted from (Kolitsi et al. 1992)).	45
Figure 2.16 The Fourier slice theorem. Figure adapted from (Kak and Slaney 2001).	48
Figure 2.17 The object function in the Fourier domain sampled along radial lines and a Cartesian square grid.....	49
Figure 2.18 Fan- beam (a) and cone – beam (b) geometries. Figures adapted from (Kak and Slaney 2001)	50
Figure 2.19 Radon data for a cone beam geometry. Figure adopted from (Turbell 2001)	52
Figure 2.20 System model.	53
Figure 2.21 Example of an algebraic reconstruction for an array of 2x2 pixels. a) The problem is to find values $f_1 - f_4$ given six projected values; in first step an initial estimate (zeros) is projected, the ART algorithm is applied and pixel values are updated, b) the process is repeated for oblique rays, and d) fo horizontal rays; the solution is obtained after 1 iteration	56
Figure 2.22 Optimization transfer in 1D. Figure adapted from (Sonka (2009))	61
Figure 2.23 Schematic of a basic principle of gradient algorithms. Vertical axis corresponds to a difference between estimated and measured projections. Figure adopted from (Bruyant 2002)	65

Figure 3.1 Flat panel detectors under investigation: Anrad SMAM (a), Dexela (b) and Hamamatsu (c).....	70
Figure 3.2 Selenium system schematic of direct conversion detector. Figure adopted from (Pisano and Yaffe 2005)	71
Figure 3.3 Dexela detector (right) and a pixel architecture of a 3T APS, R, SF and RS denotes the reset, source follower and row select transistors, respectively. Figure adopted from (El Gamal and Eltoukhy 2005).	72
Figure 3.4 Schematic of conversion of x-ray photons into an electric charge in direct conversion systems (Anrad detector) and indirect conversion systems (Dexela and Hamamatsu). Figure adopted from (Chotas et al. 1999), modified.	73
Figure 3.5 Ideal PTC with four classical noise regimes. Figure adopted from (Janesick 2007), modified.	74
Figure 3.6 PTC curve for HFW (a) and LFW (b) for Dexela detector	76
Figure 3.7 Schematic of the steps required to calculate the MTF of a system.....	79
Figure 3.8 MTF obtained at 28kV for Dexela (blue line), Anrad (red line) and Hamamatsu (green line) detectors.....	80
Figure 3.9 Schematic of the steps required to calculate the NPS of a system.	81
Figure 3.10 NPS for Dexela (diamonds), Anrad(squares) and Hamamatsu (triangles) detectors obtained at low (a), middle (b) and high (c) exposures used in mammography.	83
Figure 3.11 DQE curves for Dexela (diamonds), Anrad (squares) and Hamamatsu (triangles) detectors obtained at low (a), middle (b) and high (c) exposures used in mammography..	88
Figure 3.12 Steps required to obtain the LSF.	91
Figure 3.13 Effect of selected filters on the LSF curve (black line) and LSF obtained by smoothing the ESF prior to differentiation to the LSF (blue line).	92
Figure 3.14 Filtered LSFs of three detectors tested: Anrad (a), Dexela (b) and Hamamatsu (c).93	
Figure 3.15 Dexela detector's LSF; y-axis corresponds to normalised signal while x-axis corresponds to detector pixels dimensions (mm).	94
Figure 3.16 Signal spill out (%) of three detectors: Anrad, Dexela and Hamamatsu. For each system signal spill out was calculated in two directions: horizontal and vertical.	95
Figure 3.17 Effect of the signal spill out on PC signal at 20% (a), 35% (b) and 50% (c) illumination levels, respectively. For all graphs, the relative intensity is given in a function of displacement.	96
Figure 4.1 Elettra SYRMEP beam-line experimental setup.	99
Figure 4.2 Mammography facility at SYRMEP beamline: patient support (a) and positioning of the sample (b).....	100
Figure 4.3 IMS digital tomosynthesis system.....	101

Figure 4.4 Schematics of: (a) American College of Radiology accreditation phantom containing six fibres (F1 to F6), five microcalcification specks (S1 to S5) and five tumour-like masses (M1 to M5), (b) stereotactic biopsy phantom	102
Figure 4.5 Images of an ACR phantom with a selected ROI (left) obtained with a) a laboratory system and b) using synchrotron radiation.....	104
Figure 4.6 Planar image of a ROI in the biopsy phantom obtained a) with conventional mammography system and b) using synchrotron radiation	105
Figure 4.7 Selected reconstructions of the biopsy phantom obtained with the clinical tomosynthesis system (a) and using synchrotron radiation (b). Different features are in focus when slicing through the reconstructed volume from left to right. The objects that are not in the plane of focus appear as multiple replicas causing blurring artefacts.....	105
Figure 4.8 Single projections at 0° (a, d) and corresponding horizontal (b, e) and vertical (c, f) profile plots obtained with a conventional TS system (a, b, c) and with synchrotron radiation (d, e, f).....	106
Figure 4.9 Reconstructions (a, d) and corresponding horizontal (b, e) and vertical (c, f) profile plots obtained with a conventional TS system (a, b, c) and with synchrotron radiation (d, e, f).....	107
Figure 4.10 Contrast and CNR calculated for the clinical and synchrotron projection and reconstructed image from Figure 4.8 and Figure 4.9.	107
Figure 5.1 CAXPCi Tomosynthesis setup.	110
Figure 5.2 Coded apertures	111
Figure 5.3 Moiré pattern of the two misaligned masks rotated by an angle φ with respect to each other	112
Figure 5.4 Moiré pattern of two masks aligned with respect to φ but not correctly positioned along the z axis.....	112
Figure 5.6 Geometry of the z distance calculations.	114
Figure 5.7 Masks alignment check diagram.	115
Figure 5.8 Schematic drawing of the experimental setup for dose measurements.	117
Figure 5.9 Schematic drawing of the CAXPCi simulation scheme with two “overlapping” wires. The maximum angular range of the photons leaving the x-ray source is from Φ_{\min} to Φ_{\max} . Numbers 1-4 indicate examples of possible photon paths (see text for description). The angles α and β are the refraction angles for photon “3” caused by the large and the small sample, respectively.	119
Figure 5.10 Schematic of the mechanism used to calculate the refraction angles caused by two wires overlapping in the x-direction.	122

Figure 5.11 Simulated phase contrast signals of two wires in four different relative positions: the wires overlap (a), the wires are completely separated on the x axis (c) and the wires are in intermediate positions (b) and (d)	123
Figure 5.12 Schematic drawing of the CAXPCi setup for TS simulations and experiments. Dotted arrows indicate the direction of scanning.....	124
Figure 5.13 Simulated phase contrast tomosynthesis projections (a-e) of the wires and the corresponding profiles (f-j)	126
Figure 5.14 Reconstructed simulated (a) and experimental (b) images of the large wire, and corresponding profiles (c); reconstructed simulated (d) and experimental (e) images of the thin wire, and corresponding profiles (f).....	127
Figure 5.15 TORMAM phantom with an ROI selected for experiments.....	128
Figure 5.16 Single projection image and two reconstructed slices of the sample built of two TORMAM phantoms ((a), (b), (c), respectively). The visible horizontal lines are due to defects in the masks.	129
Figure 5.17 Single projection extracted from the tomosynthesis scan (a) and tomosynthesis reconstructions (b - e), and the corresponding profile plots (f - j) of an ROI of the double TORMAM phantom. (b) and (c) are reconstructed slices from “dithered” projections, while (d) and (e) are the reconstructed slices from a single frame with no dithering. The arrows in the profile plots indicate the peaks of the phase contrast signal at the edges of the details. The white spot visible in the planar image is due to a defect in one of the masks. This is blurred in the reconstructions.....	130
Figure 5.18 Mammography image obtained with IMS system (a) and two reconstructed tomosynthesis slices (b) and (c) of the sample built of two TORMAM phantoms.....	131
Figure 5.19 Experimental clinical profiles of a mass and a fibre taken along the lines in Figure 5.17. The arrow indicates the position of the fibre.	132
Figure 6.1 Tomosynthesis reconstructions of a ROI of the “double” TORMAM phantom performed with FBP (a, b), CG (c, d) and SPS (e, f) algorithms. The white horizontal lines are defects in the masks, and are thus not included in the evaluation of the reconstruction-induced image artefacts (see definition of ASF).....	136
Figure 6.2 Profile plots extracted from the tomosynthesis reconstructions along the red lines in Figure 6.1 obtained with the FBP (a, b), CG (c, d) and SPS (e, f) algorithms. Note that the scale on the y-axis is substantially different for the analytical (FBP) and the iterative (CG and SPS) methods.	138
Figure 6.3 Contrast shown in % (a) and CNR (b) calculated for the fibre and mass object obtained with the three evaluated reconstruction methods: FBP, SPS and CG.	139

Figure 6.4 Example of a ghosting artefact of the tumour-like object (a-d) and an artefact spread function (ASF) versus distance from the in-focus plane of a tumour-like object measured from FBP, CG and SPS reconstructions	140
Figure 6.5 Contrast (a, c) and CNR (b, d) as a function of parameter β calculated from regularized CG (a, b) and SPS (c, d) algorithms	141
Figure 6.6 Contrast (a) and CNR (b) as a function of parameter ϵ of the Huber function.....	141
Figure 6.7 CNR as a function of iteration number.....	142
Figure 6.8 Reconstruction time of CPU and GPU implementation of the penalized CG algorithm. Absorption tomosynthesis data was used for this study.	143
Figure 6.9 Schematic of an angular sampling. 15 angles evenly spread in 1° steps (diamonds), 8 angles evenly spread in 2° steps (squares) and 11 angles with non-equiangular sampling (triangles)	144
Figure 7.1 Photo of two breast samples stacked together mounted on the imaging system, (a), mammography image of the overlapping samples, (b), and three reconstructed planes (c-e), extracted from each sample (c, e) and one intermediate plane (d).....	148
Figure 7.2 Absorption image (a) and phase contrast image of a mouse (b).....	149
Figure 7.3 Head of the mouse acquired in the absorption mode (a) and in the phase contrast mode (b).....	150
Figure 7.4 Phase contrast tomosynthesis reconstructions of a mouse.	151

List of Tables

Table 3.1 Summary of the performance parameters of the sensor.....	77
Table 3.2 Values related to the used beam qualities	86
Table 3.3 Comparison of physical parameters of different mammographic systems	90
Table 3.4 Image contrast at different illumination levels for 3 detectors tested	97
Table 6.1 Contrast and CNR for fibre and tumour calculated for different angular samplings.	144

Glossary of Terms

Al	Aluminium
APS	Active Pixel Sensor
a-Se	Amorphous Selenium
ASF	Artefact Spread Function
ART	Algebraic Reconstruction Technique
CAXPCi	Coded Apertures X-ray Phase Contrast imaging
CG	Conjugate Gradient
CMOS	Complementary Metal Oxide Semiconductor
CNR	Contrast to Noise Ratio
CsI	Caesium Iodide
DICOM	Digital Imaging and Communications in Medicine
DQE	Detective Quantum Efficiency
DTS	Digital Tomosynthesis
ESAK	Entrance Surface Air Kerma
ESF	Edge Spread Function
FBP	Filtered Backprojection
FFT	Fast Fourier Transform
FWHM	Full Width at Half Maximum
HFW	High Full Well
HVL	Half Value Layer
IEC	International Electrotechnical Commission
K	Air kerma
LFW	Low Full Well
LSF	Line Spread Function
MGD	Mean Glandular Dose

ML	Maximum Likelihood
NNPS	Normalized Noise Power Spectrum
PC	Phase Contrast
PMMA	Poly(methyl methacrylate)
pMTF	Presampled Modulation Transfer Function
PTC	Photon Transfer Curve
PPS	Passive Pixel Sensor
PSF	Point Spread Function
SDD	Source to Detector Distance
SNR	Signal to Noise Ratio
SPS	Separable Paraboloidal Surrogates
SOD	Source to Object Distance
TFT	Thin Film Transistor
TS	Tomosynthesis
W	Tungsten
XPCi	X-ray Phase Contrast imaging

Chapter 1

1 Introduction

1.1 Current state and limitations of a conventional breast imaging

Breast cancer was the second most commonly diagnosed type of cancer in 2008 worldwide and the most often diagnosed cancer in the UK (Ferlay et al. 2010). A standardized number of incidences per 100,000 people differ for various regions around the world (see Figure 1.1). In Western Europe a high rate of 90 out of 100,000 women were diagnosed with breast cancer in 2008 compared to a rate of 20 out of 100,000 women diagnosed in Middle Africa. The incidence rate in the UK in 2008 was 11th highest out of 184 countries under the investigation. The incidence rate is generally higher in the developed regions of the world and lower in the developing regions.

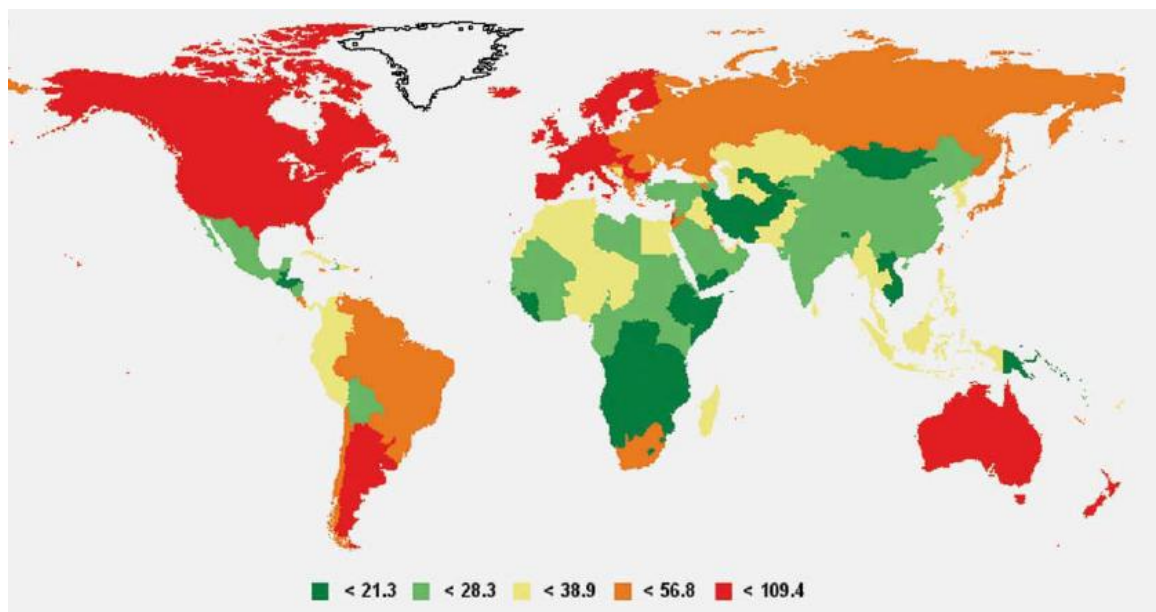


Figure 1.1 A world map showing a standardized number of breast cancer per 100,000 people. Figure adopted from (Ferlay et al. 2010)

Breast cancer is n°1 cause of women's deaths worldwide (see Figure 1.2). It was estimated that in 2008 a total of 460,000 deaths worldwide was caused by breast the cancer (Ferlay et al. 2010).

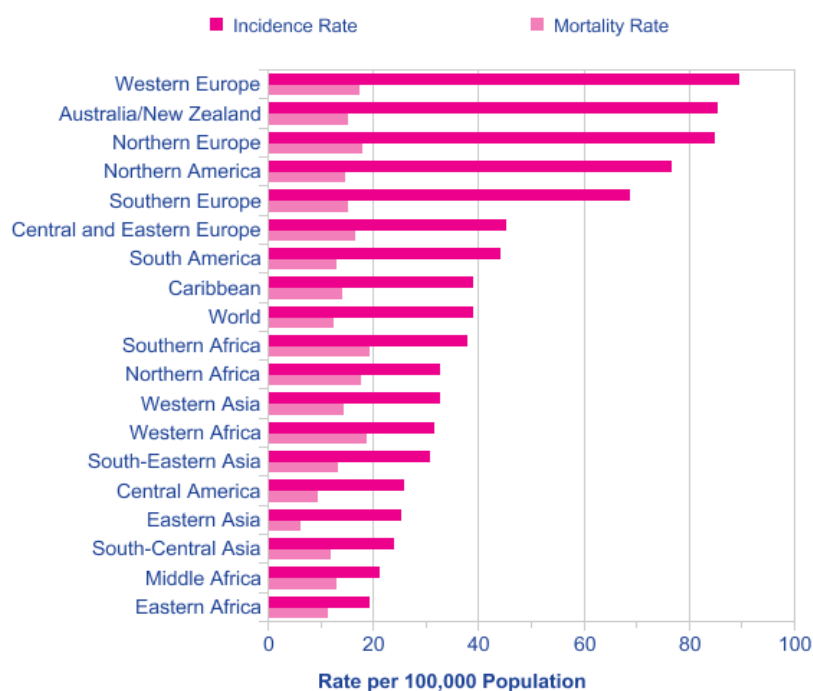


Figure 1.2 Incidence and mortality rate per 100,000 population. Figure adopted from (Ferlay et al. 2010)

X-ray mammography is currently the most effective method used for breast diagnosis, and the only tool used for the screening of breast cancer. Conventional mammography is a two-dimensional (2D) imaging method. During the procedure, the breast is compressed with a compression paddle, and typically two images are taken - one that shows a mediolateral oblique (MLO) view of the breast, and one in the cranial-caudal (CC) plane. Figure 1.3 shows the anatomy of a healthy breast. One immediately notices the complexity of the breast. The breast is composed of layers of two main types of tissue: adipose tissue and glandular tissue. The aim of mammography is to detect all abnormal structures within the breast that may indicate a malignancy. The suspicious structures that are characteristic for breast cancer are radio-opaque masses, clusters of microcalcifications and structural distortions of the fibrous breast architecture. The challenges of conventional 2D mammography are limited sensitivity, overlapping of healthy tissue (dense fibroglandular tissue) which can prevent an effective detection of underlying lesions, and overlapping of tissue that may look like a suspicious structure leading to a false positive diagnosis. Therefore, more than two standard mammographic views are often needed to completely visualize the area of interest.

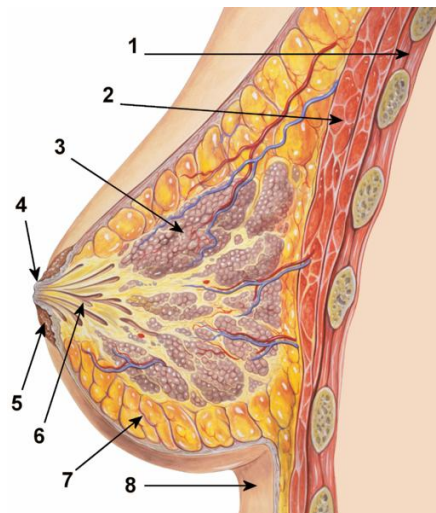


Figure 1.3 Breast anatomy. 1 – chest wall, 2 – pectoralis muscles, 3 – lobules, 4 – nipple, 5 – areola, 6 – milk duct, 7 – fatty tissue, 8 – skin. Figure adopted from (Lynch 2009).

There are different breast imaging modalities which try to address the limitations of conventional mammography. For example, breast ultrasonography (US) has been used for diagnosis of the dense breast since the 1950s. US is also at the basis of Doppler techniques, in which the ability of the sound waves to change their frequency when reflected from a moving object is used to image the red blood cells within the vessels. In order to detect the small vessels, often an ultrasound contrast agent is used, which increases the acoustic scattering from the medium it perfuses (Cassano et al. 2006; Sehgal et al. 2006; Forsberg et al. 2007). US techniques can thus provide the depth information about the breast, however their limited spatial resolution alongside the fact that they require a time-consuming examination by an experienced practitioner, prevents their use for breast screening. Another breast imaging modality, magnetic resonance imaging (MRI), has been an object of interest since the 70s. MRI has proven very sensitive in the detection of invasive breast cancers; however, it requires the use of a contrast agent, which makes it an invasive procedure. Another downside of MRI is the need to compromise between temporal and spatial resolution (Orel and Schnall 2001; Kuhl et al. 2005). Computed tomography has a great potential to visualize breast lesions in 3D, has better spatial resolution and is cheaper and less time consuming than MRI (Boone et al. 2006). However, it is not recommended due to high radiation dose. Moreover, some geometrical problems must be solved, such as a CT dedicated patient support must be designed and fabricated to achieve an acquisition geometry allowing the imaging of the part of the patient's thorax, for example one where the patient is positioned prone with respect to the x-ray beam (Boone et al. 2006). Optical breast

imaging has also been studied by a number of researchers (Fantini et al. 2005; Tromberg 2005), as it is inexpensive compared to other mammographic techniques and does not use ionizing radiation (Boone et al. 2006). The problem is the low spatial resolution caused by the fact that visible photons are significantly scattered by breast tissue. Finally, imaging modalities, like electrical impedance tomography (EIT) (Cherepenin et al. 2001; Holder 2002; Martin et al. 2002) and positron emission tomography (PET) (Berghammer et al. 2001) have been under investigation as potentially useful for mammography. In EIT, a difference in electrical resistivity between various breast tissues is used as a diagnostic tool. A series of small currents are applied to the breast, and a distribution of impedance in a cross-section of the breast is measured. EIT is a non-invasive technique, and can provide some tomographic information about the breast. The EIT research is still at its relatively early stage, and presents problems especially in spatial resolution which at present appears very difficult to solve. PET, which is also capable of providing 3D information of the breast, not only has the potential to detect breast lesions, but it can be also used to follow some metabolic processes within the breast, and therefore be useful for the prognosis of the disease. However, there are significant downsides. Firstly, PET requires specialized and costly equipment. The radioactive material, usually fluorine 18-labeled glucose (FDG), which is injected to the breast before the examination, needs to be produced using a cyclotron. Due to the short lifetime of FDG, the cyclotron needs to be on-site, which makes the overall costs of the technique even higher. Secondly, PET is not suitable for detection of small lesions (under 1cm) (Bourne 2010).

1.2 Project motivation

Digital Tomosynthesis is a well known three-dimensional (3D) imaging technique which removes the effect of the overlapping structures within tissue. During a short scan, the x-ray tube moves around the patient within a limited angular range, and a number of 2D projection images are acquired. The reconstruction of the projections leads to detailed 3D information about the object. Unlike CT, which involves rotation over an arc of more than 180°, tomosynthesis requires only a smaller number of images acquired at selected angles to produce a 3D image. This enables shorter exposure times and lower radiation dose. Therefore imaging techniques such as mammography,

angiography, chest imaging, dental examinations and orthopaedic imaging can benefit from this technique (Dobbins and Godfrey 2003).

Hard x-ray Phase Contrast (PC) imaging has been an exciting research direction in the last 15 years. Research carried out in material science, biology and medicine has shown that conventional absorption-based x-ray imaging is not sufficient when it comes to weakly attenuating objects (Lewis 2004; Groso et al. 2006; Zhou and Brahme 2008). The problem particularly significant in mammography is that low contrast masses and small size calcifications can be missed in the examinations. Phase Contrast imaging can offer a solution to these problems. The physical phenomenon responsible for image contrast is a phase change of the x-rays that cross the sample, that in a simplified representation can be seen as refraction, determined by the different indices of refraction of different regions in the object. As a result, the signal near the edges of all details in the imaged objects become enhanced. Therefore, objects that would be invisible in absorption-based scanning can be detected in PC imaging. Initially, PC imaging seemed possible only with synchrotron radiation, which can only be obtained at a limited number of highly specialized facilities around the world (see Figure 1.4). Generally, PC imaging requires high spatial and temporal coherence of the x-ray beam, as provided by synchrotron radiation. In the last few years, however, intense research has carried out in order to transfer the PC techniques from the specialized synchrotron environment into laboratory practice. One of the most promising approaches, Coded Aperture X-ray Phase Contrast imaging (CAXPCi), has been recently developed at University College London. It has been demonstrated to work with conventional polychromatic and divergent beams, as well as with detectors having limited spatial resolution.

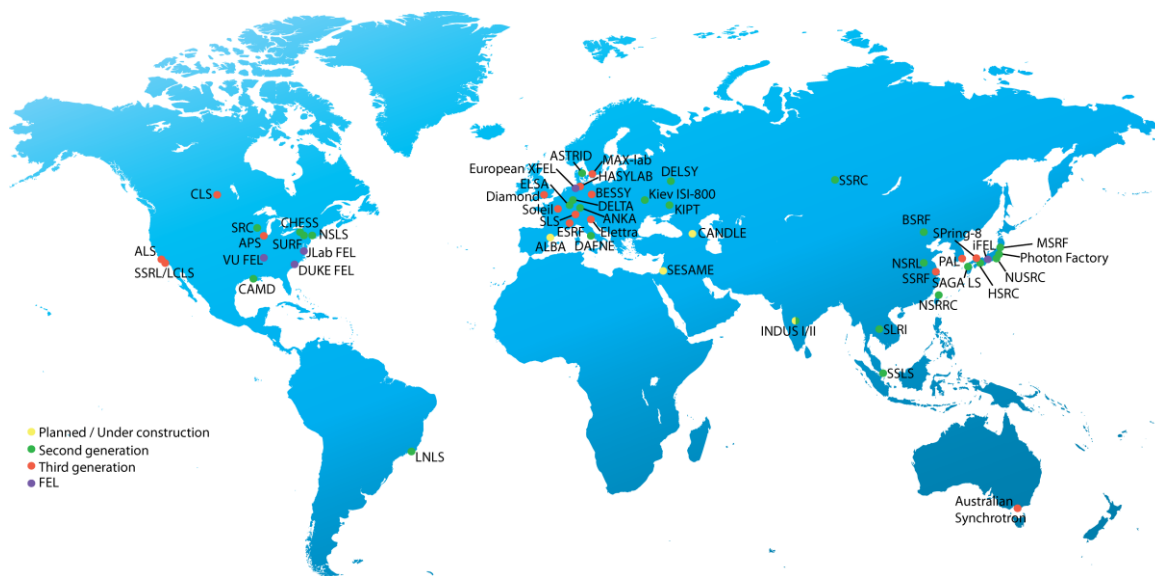


Figure 1.4 World map showing the major synchrotron sources around the world. Figure adopted from (www.diamond.ac.uk)

The aim of this work is to implement the Coded-Aperture Phase Contrast Imaging technique in Tomosynthesis geometry. A number of experiments of this type, which involved different phase contrast techniques, have been performed so far in CT (Momose and Fukuda 1995; Cloetens et al. 1999; Dilmanian et al. 2000; Fiedler et al. 2004; Wang et al. 2006; Maksimenko et al. 2007; Pfeiffer et al. 2007) and Tomosynthesis geometries (Maksimenko et al. 2007; Kang et al. 2009; Wang et al. 2009). The results of these studies show that the tomographic geometry combined with the high image contrast from PC imaging efficiently extends the enhanced detail visibility typical of PC to a 3D geometry. Most of the current experimental PC systems enabling 3D tomographic scanning, however, are unlikely to be used in a standard clinical environment, as they require the use of synchrotron radiation. CAXPCi is a technique that can be used with polychromatic divergent beams available from a conventional x-ray tube, and with an off-the-shelf detector with limited spatial resolution. Finally, the system, unlike other laboratory phase contrast setups, is not sensitive to environmental vibrations, which, together with an effective management of the radiation dose, makes it a good candidate for clinical applications.

1.3 Key contributions made to the field

This thesis presents the proof of concept results of the CAXPCi based Tomosynthesis. To the best of the author's knowledge, the only attempts to perform a phase contrast

based tomosynthesis outside the synchrotron, was made by Wang et al (2009) and Hammonds et al (2010). The first one was performed using a Talbot-Lau interferometry and conventional x-ray source. An absorption grating was used in front of the x-ray source to produce an array of individually coherent but mutually incoherent x-rays. This leads to problems with increased dose and exposure times (see Chapter 2.1.2.4). The imaged object was very simplistic (dryer balls). In the second paper (Hammond et al), the authors used a simpler free space propagation method to produce the phase contrast effects, and a more complicated sample of a broccoli flower. In this case, however, a microfocal x-ray source was employed with a focal spot size of 10 μm , which resulted in high dose and extremely long exposure times. In this work, a comprehensive study on the phase contrast tomosynthesis was performed for the CAXPCi system. Firstly, a study on the detection system was undertaken. Three detectors were tested according to some criteria being the highest spatial resolution and the smallest signal spill-out from a given pixel to adjacent ones. The one with best performance was chosen for the further experiments in the TS geometry. Next, a tomosynthesis imaging of a mammographic biopsy phantom was performed using a synchrotron radiation and the free space propagation technique with a flat panel detector. The phase contrast signal was clearly visible in the reconstructed slices throughout the object volume and different features located at various depths in the phantom were well separated. The CAXPCi based tomosynthesis was firstly simulated with a dedicated script in MATLAB for two thin cylindrical plastic objects. The simulated data was then compared with an experiment and good agreement was achieved. The simulator can be used to simulate the three dimensional phase contrast signal from more complex samples in the future. The new method was then tested for a range of different samples, starting from the mammographic TORMAM phantoms, mastectomy breast tissue samples and small animals. In all cases, the individual reconstruction planes were well separating while preserving the phase contrast information. The MGD for a double TORMAM phantom in the CAXPCi based TS setup was estimated to be roughly three times larger than that from a conventional absorption-based tomosynthesis system. The exposure time of 105 seconds of a full TS scan is the lowest of all the phase contrast imaging methods outside the synchrotron facilities. Much room for the improvement remains in order for the technique to be used in clinical practice and the reader will find some ideas for the possible solutions in Chapter 8 of this thesis.

This work also laid the foundations for the comparison of different reconstruction algorithms for the images containing both absorption and phase contrast information. Although all of the algorithms used in this study were developed for the reconstruction of images obtained with purely absorption-based imaging, they provided sufficiently good performances on the reconstruction of the images containing mixed information, i.e. the phase contrast and absorption signal simultaneously. It was found that the analytical FBP method resulted in very noisy images but preserved the phase contrast signal better than all other tested algorithms. The iterative statistical methods resulted in greatly enhanced CNR, but at the cost of smoothing of the phase contrast peaks and decreasing the overall image contrast. It was suggested that a dedicated statistical reconstruction method was needed for the phase contrast images in which the roughness function would need to be redefined.

1.4 Thesis overview

Chapter 2 of this thesis gives an overview of the theory and methods used in Phase Contrast imaging and in Tomosynthesis, as well as a description of the quantities used in this work for the evaluation of image quality. In Chapter 3, the characterization of the detectors is described, and a choice of the best one is made. Chapter 4 consists of a description of free space phase contrast imaging with the mammographic phantoms in planar and Tomosynthesis geometries. Chapter 5 presents the proof of concept results of laboratory-based phase contrast tomosynthesis. In that chapter, a description of how the CAXPCi system was set up is provided, and the results of simulations are given alongside their experimental verification. Chapter 6 presents of the results of three reconstruction algorithms used in CAXPCi TS. Chapter 7 includes examples of possible applications of the proposed method. Finally, chapter 8 summarizes the work done so far, and lists suggestions for future work.

Chapter 2

2 Theory

2.1 Phase Contrast Imaging

2.1.1 Introduction to Phase Contrast Imaging

2.1.1.1 Conventional radiography vs. Phase Contrast imaging

Conventional x-ray medical imaging is based on the difference in the attenuation of radiation by different regions within the sample. However, if an x-ray beam is considered as a wave it can be noted that not only its amplitude but also its phase changes. There are several ways of using the phase information in order to produce image contrast. A detailed description of the most popular phase contrast (PC) methods will be given in chapter 2.1.2. PC imaging enables detection of weakly absorbing materials that are invisible to conventional absorption-based radiography. For energies used in medical imaging, the image contrast can be orders of magnitude higher than for absorption.

The theory behind phase contrast imaging can be described by means of the complex refractive index, which is given by:

$$n = 1 - \delta + i\beta \quad (2.1)$$

The unit decrement δ of the real part $\Re = 1 - \delta$ describes the phase shift of the wave, while the imaginary part β is the attenuation index and describes the attenuation of the wave. The decrement δ can be further written as:

$$\delta = 2\pi\rho_z Z r_0 / k^2 \quad (2.2)$$

where ρ_z is the atomic density in m^{-3} , Z is the atomic number, $r_0 = 2.82 \cdot 10^{-15} [m]$ is the electron radius, and $k = 2\pi / \lambda$ is the wave number. The phase change can be calculated as (Wu and Liu 2003)

$$\Phi = -\frac{2\pi}{\lambda} \int_{\text{object}} \delta(s) ds \quad (2.3)$$

where the integral is over the ray path within the object.

The imaginary part in equation (2.1) is usually defined as:

$$\beta = \frac{\rho_z \sigma_a}{2k} \quad (2.4)$$

where σ_a is the absorption cross-section.

According to (Henke et al. 1993), equation (2.1) can also be rewritten in the form:

$$n = 1 - \frac{r_0}{2\pi} \lambda^2 \sum_{\rho_z} n_{\rho_z} f_{\rho_z}(0) \quad (2.5)$$

where n is the refractive index, r_0 is the electron radius, λ is the wavelength, n_{ρ_z} indicates a number of atoms with atomic number Z and density ρ and f_{ρ_z} is the forward scattering factor.

The complex atomic scattering factor in the forward scattering direction is:

$$f(0) = f_1 + if_2 \quad (2.6)$$

Both the real part f_1 , which corresponds to refraction, and the imaginary part f_2 , which refers to absorption, have been tabulated as a function of energy for different materials (Henke et al. 1993). Figure 1 illustrates the relation between f_1 and f_2 for PMMA (Polymethyl methacrylate), which is a material commonly used to build phantoms for x ray studies, as it has attenuation properties similar to those of human tissue. For an energy of 10keV, the real part of the above equation is $f_1 = 2.67 \cdot 10^{-6}$, and is 3 orders of magnitude larger than the imaginary part $f_2 = 3.71 \cdot 10^{-9}$. Therefore, it should be significantly easier to detect phase shift effects than the loss in beam intensity, which is the effect caused by absorption within the sample.

A theoretical formalism which describes the phase contrast image formation of weakly absorbing and low phase shifting samples was first given by (Pogany et al. 1997; Wilkins et al. 1997). It describes the interaction of the wave with the object by a two-dimensional transmittance function:

$$T(x, y) = \exp(i\Phi(x, y) - \frac{\mu(x, y)}{2}) = A(x, y)e^{i\Phi(x, y)} \quad (2.7)$$

where $A(x, y)$ is x-ray amplitude transmission, and $\Phi(x, y)$ and $\mu(x, y)$ are the projections over z of object phase shift and linear attenuation coefficient. If a

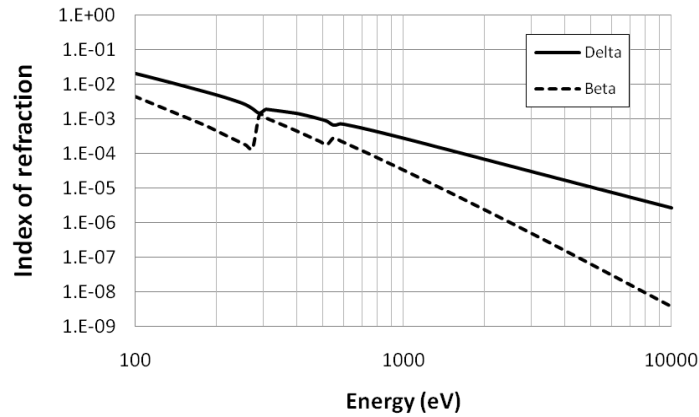


Figure 2.1 The real (f_1) and imaginary part (f_2) of the atomic scattering factor for PMMA, as a function of photon energy.

three-dimensional (3D) object is considered, then $\Phi(x, y)$ and $\mu(x, y)$ become:

$$\Phi(x, y) = \frac{-2\pi}{\lambda} \int \delta(x, y, z) dz, \quad (2.8)$$

$$\mu(x, y) = \frac{4\pi}{\lambda} \int \beta(x, y, z) dz \quad (2.9)$$

As a consequence of passing through the object, the wave will be phase shifted. The field of the diffracted wave can be described, by means of the paraxial Fresnel theory (Born and Wolf 1980; Wilkins et al. 1997), as:

$$f(x, z) = \sqrt{\frac{i}{\lambda z}} \exp(ikz) \int T(\eta) \exp(ik \frac{(x-\eta)^2}{2z}) d\eta \quad (2.10)$$

where η corresponds to the coordinates on the object plane (see Figure 2.2).

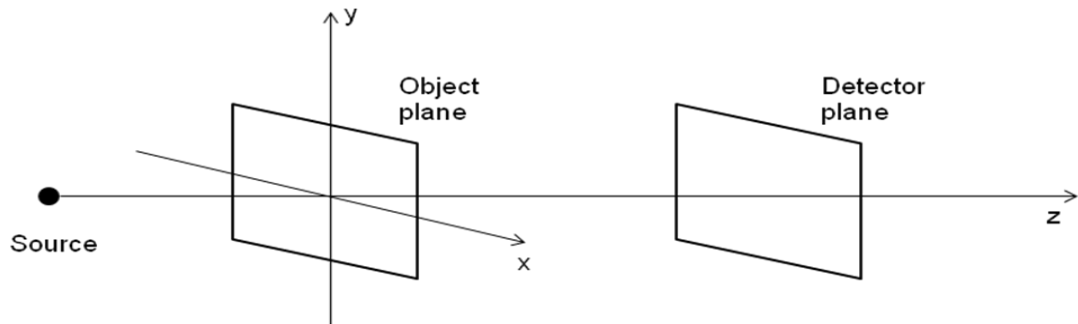


Figure 2.2 Phase contrast imaging geometry.

2.1.1.2 Theoretical approaches in phase Contrast imaging

There are two main mathematical approaches commonly used to describe phase contrast effects. The first one, the ray optical approach, is simpler but approximated. It describes phase contrast effects as a consequence of refraction of the x-rays inside the illuminated object. The second one, the wave optical approach, is more complex but rigorous, and it shows the phase contrast effect as part of the paraxial Fresnel diffraction theory. Both approaches for weakly absorbing objects will be described in this chapter to show that, although they start from different levels of approximation, they give similar results under certain simplified assumptions (Peterzol et al. 2005).

Ray optical approach

Consider a monochromatic parallel beam of initial intensity $I_i(x, y)$ propagating in the z direction. Assuming that the distance between the object and the detector d is larger than the object size, and that there is no attenuation of the x-rays by the object, one can estimate the coordinates of the point at the detector surface where a given x-ray will be recorded after being refracted in the point $(x, y, 0)$ within the object by an angle $\alpha(x, y)$ as:

$$x_d \approx x + d\alpha_x(x, y) \quad (2.11)$$

$$y_d \approx y + d\alpha_y(x, y) \quad (2.12)$$

In the above equations $\sin \alpha$ was replaced by the angle α itself, as the magnitude of deviations in phase contrast imaging are in order of microradians. $\alpha_x(x, y)$ and $\alpha_y(x, y)$ can be expressed as:

$$\alpha_x(x, y) \approx \frac{\lambda}{2\pi} \frac{\partial \Phi(x, y)}{\partial x} \quad (2.13)$$

$$\alpha_y(x, y) \approx \frac{\lambda}{2\pi} \frac{\partial \Phi(x, y)}{\partial y} \quad (2.14)$$

There is only one solution of equation (2.10) which describes the intensity of the beam on the detector surface (Gureyev and Wilkins 1998):

$$I_d(x_d, y_d) = I_i(x, y) \left| \frac{\partial(x_d, y_d)}{\partial(x, y)} \right|^{-1} \quad (2.15)$$

which can be written as:

$$I_d(x_d, y_d) = I_i(x, y) \left| \begin{array}{cc} 1 + d \frac{\partial \alpha_x(x, y)}{\partial x} & d \frac{\partial \alpha_x(x, y)}{\partial y} \\ d \frac{\partial \alpha_y(x, y)}{\partial x} & 1 + d \frac{\partial \alpha_y(x, y)}{\partial y} \end{array} \right|^{-1} \quad (2.16)$$

By neglecting the products of partial derivatives as we are assuming that $d\lambda \ll 1$, the equation becomes:

$$I_d(x_d, y_d) \approx I_i(x, y) \left[1 + \frac{d\lambda}{2\pi} \nabla_{\perp}^2 \Phi(x, y) \right]^{-1} \quad (2.17)$$

By making some further assumptions that $d\alpha_x/x \ll 1$ and $d\alpha_y/y \ll 1$ (so that x_d, y_d become x, y), and that the variations of the phase are small ($d\lambda/2\pi \nabla^2 \Phi(x, y) \ll 1$), the final equation to calculate the intensity of the x-ray in the detector plane is:

$$I_d(x, y) \approx I_i(x, y) \left[1 - \frac{d\lambda}{2\pi} \nabla_{\perp}^2 \Phi(x, y) \right] \quad (2.18)$$

So far we have assumed the beam to be parallel. In order to take into account the divergent beam produced by a point source, one needs to take into account the image magnification $M = (s + d)/s$, where s is the source-to-object and d the object-to-detector distance. In this case, by following similar steps as above, and by implementing corrections for the magnification, equation (2.13) can be rewritten as:

$$I_d(Mx, My) \approx I_{d,i}(x, y) \left[1 - \frac{d\lambda}{2\pi M} \nabla_{\perp}^2 \Phi(x, y) \right] \quad (2.19)$$

where the intensity $I_{d,i}(x, y)$ is the intensity of the beam at detector active surface in the absence of the object. Finally, in order to take into account the attenuation of the x-rays within the object, the intensity $I_{d,i}(x, y)$ becomes $I_{d,i}(x, y) \exp[-\mu(x, y)]$ (Peterzol et al. 2005), so the following expression known as Transport of Intensity Equation for weak attenuation (TIEW) is obtained:

$$I_d(Mx, My) \approx I_{d,i}(x, y) e^{-\mu(x, y)} \left[1 - \frac{d\lambda}{2\pi M} \nabla_{\perp}^2 \Phi(x, y) \right] \quad (2.20)$$

From this equation it can be seen that the phase contrast effects are observed only for distances $d > 0$, and that they become more intense as d increases.

Wave optical approach

It will now be shown how the phase contrast phenomenon can be described using the wave optical approach, in particular Fresnel diffraction theory. The diffraction pattern is created by the interference of the wave phase-shifted by an object and the undisturbed wave. Let us consider a wave propagating in free space over a distance d , after having transversed an object characterized by a transmittance function T (see equation (2.7)). The intensity of the wave forms the Fresnel diffraction pattern, and is given by:

$$I_d(\vec{r}_{\perp}) = I_i(\vec{r}_{\perp}) |T(\vec{r}_{\perp}) * P_d(\vec{r}_{\perp})|^2 \quad (2.21)$$

where $\vec{r}_{\perp} = (x, y)$, $I_i(\vec{r}_{\perp})$ is the initial intensity of the wave, T is defined by equation (2.7) and $P_d(\vec{r}_{\perp})$ is the Fresnel propagator defined as:

$$P_d(\vec{r}_{\perp}) = \frac{1}{i\lambda d} e^{i\frac{\pi}{\lambda d} |\vec{r}_{\perp}|^2} \quad (2.22)$$

In order to express equation (2.21) in the frequency domain, it is necessary to apply a Fourier transform to each side of equation (2.22), which gives:

$$P_d(\vec{f}) = e^{-i\pi\lambda d |\vec{f}|^2} \quad (2.23)$$

where $\vec{f} = (u, v)$ denotes the spatial frequencies conjugated with x, y . Now, equation (2.21) can be rewritten in Fourier space as (Langer et al. 2008):

$$I_d(\vec{f}) = \int I_i(\vec{r}_\perp) T(\vec{r}_\perp - \frac{\lambda d}{2} \vec{f}) T^*(\vec{r}_\perp + \frac{\lambda d}{2} \vec{f}) e^{-i2\pi\vec{r}_\perp \cdot \vec{f}} d\vec{x} \quad (2.24)$$

For $d=0$, only the attenuation of the object is present in the above equation. If $d>0$, the phase signal becomes apparent, in addition to attenuation.

Further, by expanding $T(\vec{r}_\perp \pm \frac{\lambda d}{2} \vec{f})$ in a Taylor series:

$$T(\vec{r}_\perp \pm \frac{\lambda d}{2} \vec{f}) = T(\vec{r}_\perp) \pm \frac{\lambda d}{2\pi} \vec{\nabla}_\perp T(\vec{r}_\perp) \quad (2.25)$$

And inserting it into equation (2.23), the intensity of the wave can be expressed as (Langer et al. 2008):

$$I_d(\vec{r}_\perp) = I_{d=0}(\vec{r}_\perp) - \frac{\lambda d}{2\pi} \vec{\nabla}_\perp [I_{d=0}(\vec{r}_\perp) \vec{\nabla}_\perp \Phi(\vec{r}_\perp)] \quad (2.26)$$

With the assumption that the absorption term ($\mu(\vec{r}_\perp)$) is constant in the above equation, $I_{d=0}(\vec{r}_\perp)$ can be moved outside the gradient operator, leading to:

$$I_d(\vec{r}_\perp) = I_{d=0}(\vec{r}_\perp) [1 - \frac{\lambda d}{2\pi} \vec{\nabla}_\perp^2 \Phi(\vec{r}_\perp)] \quad (2.27)$$

In order for the equation to be valid for a divergent beam produced by a point source, one needs to introduce the image magnification M into equation (2.22), so the Fresnel propagator becomes:

$$P_d(\vec{r}_\perp) = \frac{M}{i\lambda d} e^{i\frac{\pi}{\lambda d} |\vec{r}_\perp|^2} \quad (2.28)$$

After similar transformations, equation (2.26) can be expressed as:

$$I_d(\vec{r}_\perp) = I_{d=0}(\vec{r}_\perp) [1 - \frac{\lambda d}{2\pi M} \vec{\nabla}_\perp^2 \Phi(\vec{r}_\perp)] \quad (2.29)$$

The above equation is called the Transport of Intensity Equation for Weak attenuation for conical beams, and it is equivalent to equation (2.20) which was obtained using the ray optical approach.

2.1.1.3 Edge enhancement

Equations (2.13) and (2.14) describe the angle of refraction of the x-rays in both x and y directions in the plane perpendicular to the propagation direction. This angle is of the

order of microradians for light materials and at the energies generally used in medical imaging. The refraction of x-rays typically occurs at the edges of the details, where the phase gradient is largest. As a consequence, the x-rays change speed and deviate from their original direction. Figure 2.3 shows an example of this mechanism for an object with a circular cross-section. The intensity profile shows positive and negative peaks at the boundaries of the object, which correspond to the increases and losses in the detected intensity caused by refraction. In this way the edges of the object are enhanced - hence the name of the process, edge enhancement.

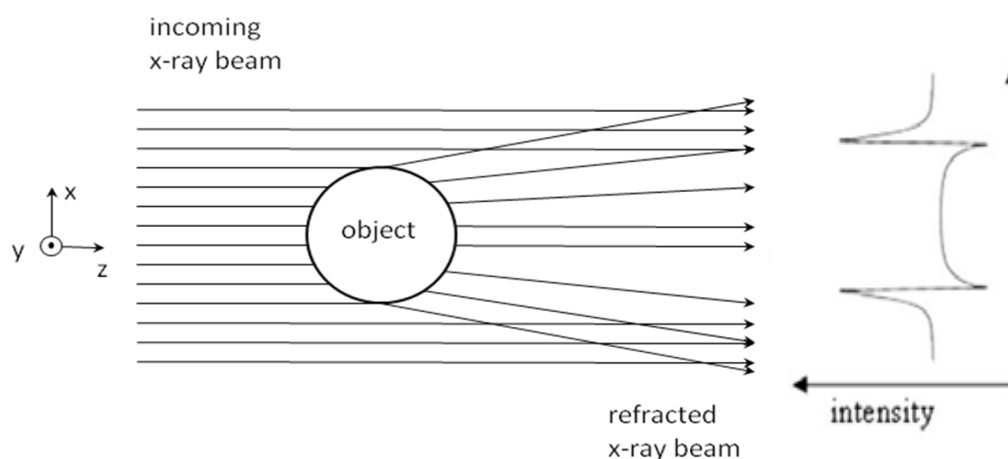


Figure 2.3 Mechanism of the phase contrast signal creation from an object with a circular cross-section. Due to the phase gradient at the edges of the detail, x-rays are refracted and change their original direction. The measured intensity profile shows loss in intensity in the forward direction, and an increase in the direction corresponding to the refraction angle. Note that the refraction angles have been highly exaggerated for easiness of display.

2.1.2 Generation of phase contrast effects

There are currently several XPCi techniques that enable converting phase effects into detectable intensity differences, often in the form of edge enhancement. The most general classification would be into methods that use interferometers (analyser-based methods or grating interferometers) or free-space propagation (FSP) methods. Techniques that require the use of crystals are restricted to synchrotron radiation sources, while the FSP and grating methods can, with some caveats, be used with polychromatic x-ray beams. Generally speaking, interferometric methods measure the phase Φ itself, analyser-based methods measure the phase gradient $\nabla\Phi$, and free-space

propagation methods measure the Laplacian of phase $\nabla^2\Phi$ (Wu and Liu 2003). In this chapter, a general overview of these phase contrast techniques will be given.

2.1.2.1 Free space propagation

Free space propagation (FSP) is the simplest of all PC techniques in terms of set-up requirements, as only an x-ray source and a detector are needed. If the source has a sufficient degree of spatial coherence, it is possible to observe the phase contrast effects with a very simple setup, arising because of the coherent properties of the x-ray beam itself. By allowing for sufficient propagation length (see Figure 2.4), the x-rays will interfere, thus creating a pattern which can be detected (Snigirev et al. 1995; Arfelli et al. 1998; Zhang et al. 2008). The recorded images contain both absorption and phase signal. A number of methods have been developed to retrieve a pure phase signal from the mixed images (Gureyev et al. 1995; Cong et al. 1999; Arhatari et al. 2005). The FSP technique is a good candidate to be implemented into laboratory or hospital environments as it works with divergent, polychromatic beams (Wilkins et al. 1996; Olivo and Speller 2006). It has been noticed, however, that it is greatly affected by large source and pixel sizes (Olivo and Speller 2006), which substantially limits its practical applicability.

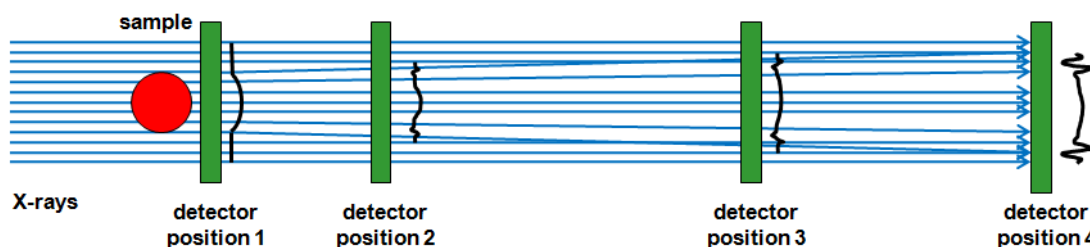


Figure 2.4 Schematic of a fundamental idea of the free space propagation technique. The setup used to image the sample (red), consists only of a detector (green) with suitable spatial resolution. On the image, different positions of the detector are shown and corresponding PC signals.

2.1.2.2 Bonse/Hart interferometer

Interferometric methods based on perfect crystals (Bonse and Hart 1965) were one of the first approaches in PC imaging (Momose and Fukuda 1995) to be developed. They involve 3 silicon crystals acting as monochromators selecting a narrow band of wavelengths (see Figure 2.5). The first crystal splits the beam into two identical beams. The second crystal redirects the two beams towards the same point; one beam crosses a

sample located in its path, while the other (reference) beam does not. When the two beams are recombined in the third crystal, they produce an interference pattern as a consequence of the phase shift caused by the sample. This technique requires strictly parallel and monochromatic beams, which makes it feasible at synchrotron facilities only. Moreover, this technique is highly sensitive to vibrations, which can disturb the alignment of the crystals (Momose et al. 2001). Ideally, the three crystal blades should be part of the same single crystal. If different crystals are used, it becomes difficult to align them, as the inter-crystal distances must be tuned within a fraction of an atomic distance. If, alternatively, a single crystal block is used, with the three crystal blades cut out of it and remaining attached to a common base, this leads to reduction of the sample size that can be imaged, as this needs to be much smaller than the original crystal.

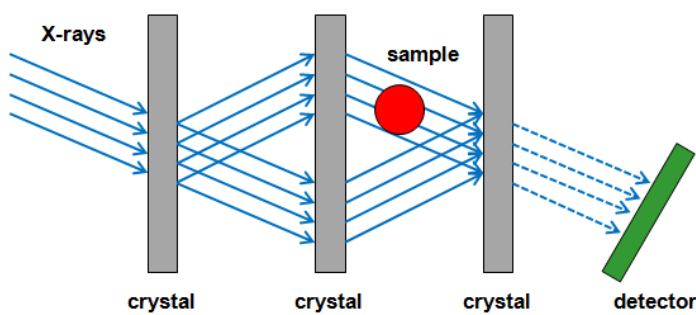


Figure 2.5 Schematic of a fundamental idea of the interferometric technique. The setup, which is used to scan a sample (red), consists of 3 crystals (grey) and a detector (green).

2.1.2.3 Diffraction Enhanced/Analyzer based imaging

Analyzer-based setups like the one used in diffraction enhanced imaging, DEI (Chapman et al. 1997; Lewis et al. 2003; Zhang et al. 2010), consist of an analyser crystal placed between the sample and detector (see Figure 2.6). Another crystal called monochromator is placed before the sample to produce a monochromatic beam. The analyser crystal is oriented at an angle with respect to the direction of the incoming beam. This ensures that the refracted part of the beam is reflected onto the detector if the Bragg condition is satisfied. By changing the angle of the analyser, different refraction angles can be explored. Images acquired at several angles of the so called reflectivity curve or the rocking curve (RC) are then combined to create a final image. This technique requires high temporal coherence of the beam, a condition typically fulfilled only at synchrotrons.

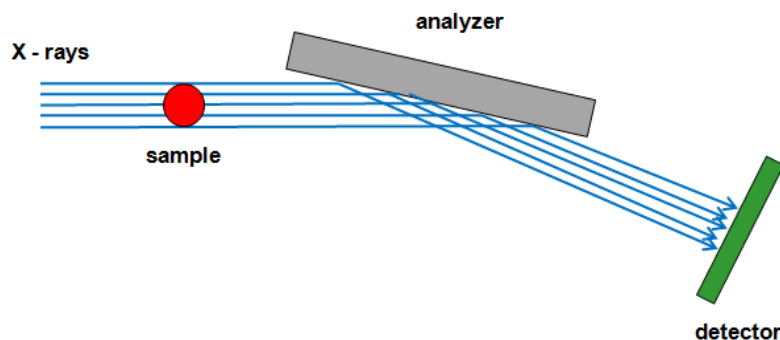


Figure 2.6 Schematic of the Analyser based PC technique. The setup used to image the sample (red) consists of an “analyser” crystals (grey) placed between the sample, and the detector (green). An additional crystal (the monochromator, not shown in the picture) must be present upstream of the sample to provide the necessary degree of temporal coherence.

2.1.2.4 Talbot/Lau interferometer

The fourth approach is based on two sets of diffraction gratings placed between the sample and detector (see Figure 2.7). The first grating splits the beam into a number of beams which interfere with each other creating an interference pattern (seen as fringes in planes perpendicular to the optical axis) at some distance from the diffraction grid (Weitkamp et al. 2005). The location of the fringes changes according to the perturbations of the incident wave fronts caused by the changes in refractive indices in the object. These distortions in the wave front can be then determined from the relative displacement of the fringes. An absorption grid placed in front of the detector is required in order to modulate the finely spaced interference pattern sufficiently for the detector to resolve it. To adapt the technique to a spatially incoherent source, a third grating must be added in front of the source to create multiple spatially coherent beamlets. Grating-based techniques are less restrictive than crystal methods when it comes to beam monochromaticity, and they can be used with some degree of polychromaticity (Pfeiffer et al. 2006). However, it is still difficult to overcome the problems of system sensitivity to vibrations and inefficiently delivered dose. Due to the grid thickness being much larger than the transverse apertures, the angular acceptance to the emitted beam is limited. This leads to longer exposure times and higher dose. Moreover, the grating’s slits are orientated vertically which makes the technique sensitive to phase effects in one direction only (Olivo and Speller 2007).

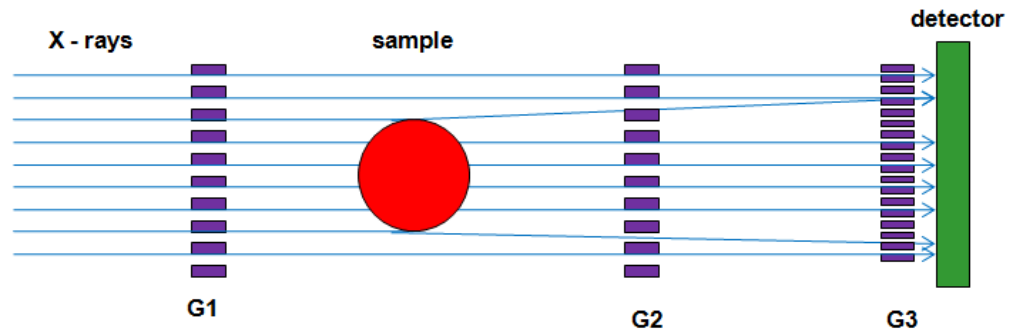
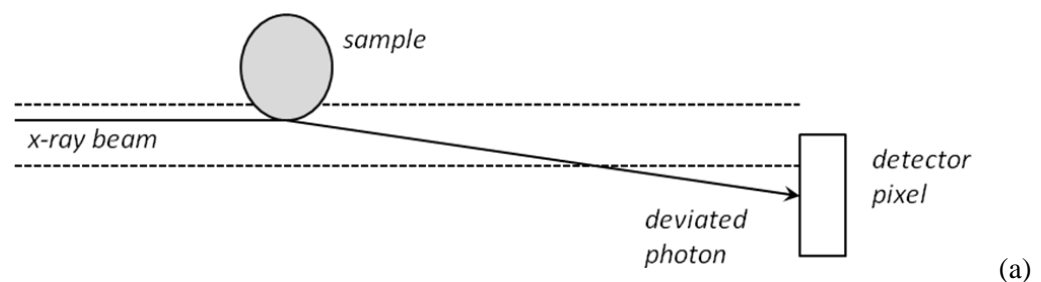


Figure 2.7 Schematic of the grating-based PC method. The setup used to image the sample (red) consists of 3 gratings (purple), one before the sample (G1) and two behind the sample (G2 and G3) and a detector (green).

2.1.3 Coded Apertures Phase Contrast Imaging

2.1.3.1 Edge illumination method

In order to detect local deviations of the photons one needs to use an imaging system with high angular sensitivity. As seen above, this is achievable at synchrotron facilities by means of silicon crystals placed between the sample and the detector. These crystals are characterized by a narrow curve describing their reflectivity as a function of the incident angle (for a monochromatic beam), and can therefore be used to analyse the x-ray direction. A similar process of selecting photon directions is performed in the method presented in this work. The basic idea of the technique is to illuminate only one edge of the detector pixel (Olivo et al. 2001), as shown in Figure 2.8. The introduction of a sample can lead to a change in photon direction. As a consequence, photons that in the absence of the sample would not reach the detector pixel are deviated inside it and can be detected (see Figure 2.8a) or, conversely, photons that would normally be detected are deviated by the sample and not detected anymore (see Figure 2.8b). This results in a signal containing positive and negative peaks at the edges of the imaged sample. This technique is called the edge illumination method.



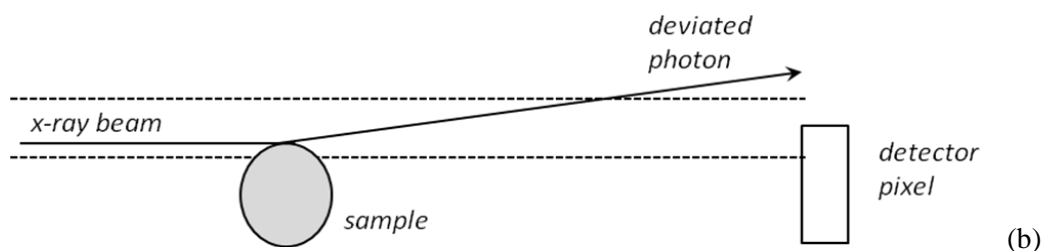


Figure 2.8 Schematic of the basic principle of the edge illumination technique.

2.1.3.2 Coded Apertures Phase Contrast Imaging

Coded Apertures Phase Contrast Imaging (Olivo and Speller 2007) is the PC imaging method used in the present work. It has been introduced recently as a technique with the potential to transfer all the advantages of PC imaging from synchrotron environments to laboratory conditions, overcoming most of the limitations associated with other PC techniques (Olivo and Speller 2007).

The CAXPCi is an adaptation of the edge illumination technique to divergent and polychromatic beams generated by conventional sources, suitable for imaging large samples with no scanning involved. Two sets of coded apertures are used, one placed before the sample and the other one in contact with the detector, to allow for repeating the edge illumination principle for each detector row or column (see Figure 2.9). The first set of coded apertures (from now on referred to as the sample mask) acts like a beam splitter and separates the beam into a number of independent beams. The second set of coded apertures (referred to as the detector mask) is positioned in such a way that each beam impinges on the edges of an aperture in the detector mask. Figure 2.9 shows the introduction of a sample which is placed between two sets of coded apertures. Image contrast arises from the difference between detected and undetected photons, which results in a relative intensity change between positive and negative peaks of the PC signal (see Figure 2.10). Positive peaks are created by photons that in the absence of the sample would not hit the pixel, but are deviated and reach the active area of the pixel as a consequence of the refraction caused by the phase shift. Conversely, negative peaks relate to the case where photons that would hit an active area on the pixel are deviated outside it, thus hitting a solid part of the detector mask.

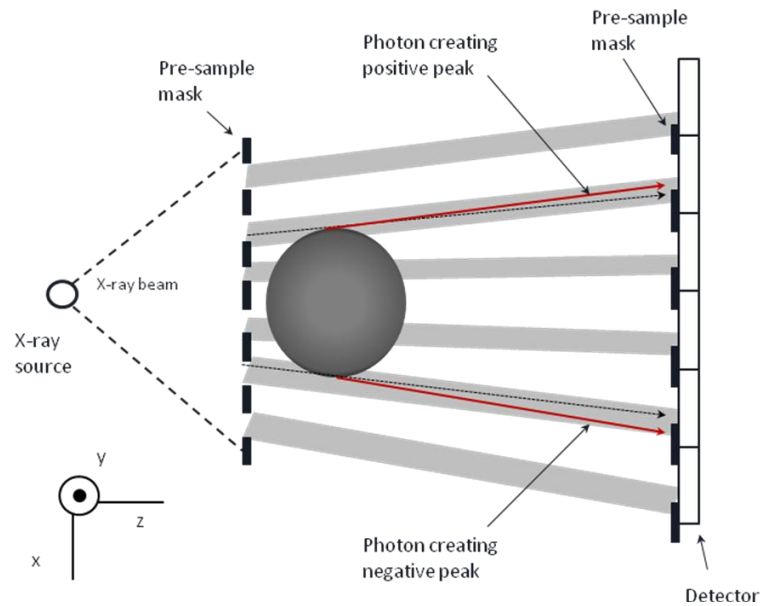


Figure 2.9 Coded Aperture Phase Contrast setup. Dotted arrows indicate photon directions in the absence of the sample.

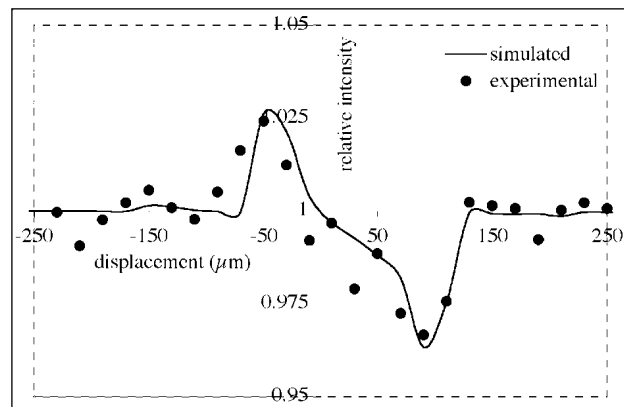


Figure 2.10 Phase Contrast signal of a 100 μm wire obtained at 40keV with the experimental setup shown in Figure 5. Dots describe the experimental data while solid line is the simulated data.

In order to maximize the amount of the practical signal being detected, the two sets of coded apertures are shifted, one with respect to the other, to increase the acceptance of photons refracted in a given direction. This is equivalent to slightly misaligning the crystal from its Bragg position in analyser based imaging. By changing the relative positions of the coded apertures, different illumination levels of the detector pixels are tested (Olivo and Speller 2007; Olivo et al. 2008).

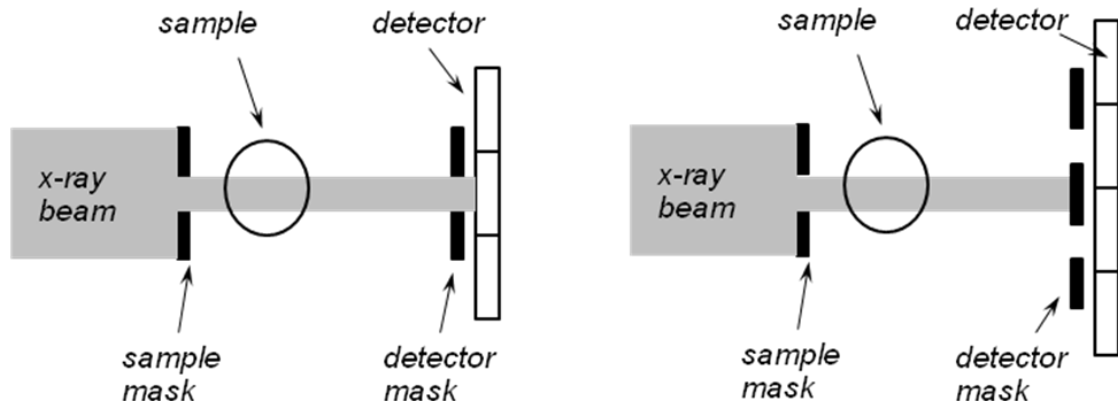


Figure 2.11 Full illumination (a) and no illumination (b) of the detector.

Figure 2.11 shows two possible alignments of the masks: one in which the masks are completely aligned and the aperture in the detector mask is fully illuminated and one in which the masks are misaligned such that no direct photons reach the detector. Each intermediate shift of the masks results in partial illumination of edge of the aperture mask (i.e. effectively the edge of the sensitive part of the pixel). To visualize this, Figure 2.12 shows the effect of the full and partial illumination of the pixel on the acquired signal. The illumination of the entire pixel, indicated as “fullbeam” in the picture, is achieved by aligning the masks so that the sample mask apertures match the detector mask apertures allowing the whole beam to be transmitted through the latter. If the sample mask is shifted with respect to the detector mask so that only half of the beam goes through it, the difference between the positive and negative peak (image contrast) increases. In general, the smaller the illuminated fraction of the pixel, the higher the image contrast. Note that using one half of the “fullbeam” leads to the same signal shape (apart from spatial inversion) as using the other half, and the positive and negative peaks on both sides of the pixel provide the same information about the edges of the object. Therefore it is rational to use only one edge of the active area of the pixel to get the desired information. Of course, by decreasing the illuminated part of the detector pixel, the number of detected x-rays decreases accordingly, leading to increased quantum noise. Therefore it is necessary to increase the exposure time accordingly, until a satisfactory statistics is achieved.

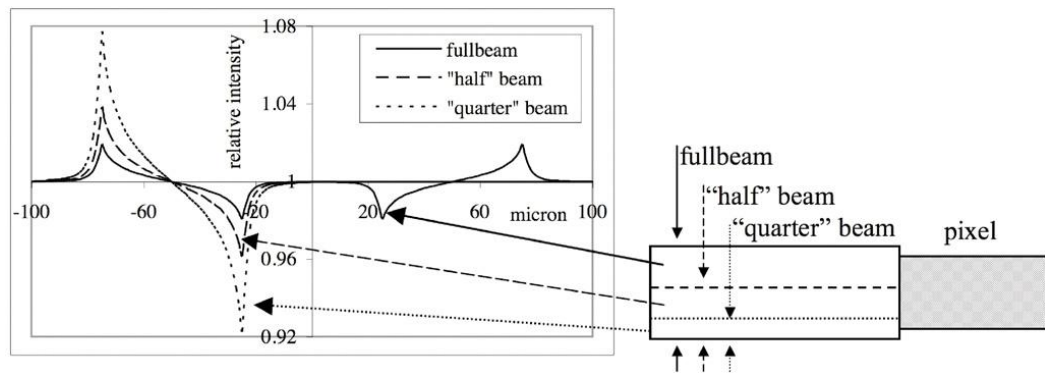


Figure 2.12 Effect of partial pixel illumination on the simulated PC signal (left) of a 100µm polyethylene fibre and the corresponding illumination conditions (right). The solid, dashed and dotted line of the acquired signal corresponds to illumination of the full pixel (fullbeam), half of the pixel (“half” beam) and a quarter of the pixel (“quarter” beam). Figure adopted from (Olivo and Speller 2008).

Currently the masks used in the laboratory system feature long apertures which enable sensitivity to phase contrast effects in one direction only. However, it has been previously shown that L-shaped apertures can be used to allow for simultaneous sensitivity in two directions (Olivo and Speller 2007).

2.1.3.3 Source size and coherence requirement

The major concern with the new technique was the possibility of using it with polychromatic, divergent beams from a conventional source and with finite resolution detectors. In (Olivo and Speller 2006) the influence of all three factors on free-space phase contrast signal was first simulated and then verified experimentally for FSP XPCi. These results were then translated to CAXPCi in (Olivo and Speller 2007). First, in order to take into account the effect of beam polychromaticity, the polychromatic pattern I^{poly} was calculated as weighted sum of monochromatic patterns I^{mono}

$$I^{poly} = \sum_{k=1}^N \omega_k I_k^{mono} \quad (2.30)$$

where ω_k represent the normalised spectral entries. The second step involved convolution of the polychromatic pattern I^{poly} with function f describing the convolution of detector point spread function PSF and rescaled source distribution s , $f = PSF * s$, which leads to the following expression:

$$J^{poly} = I^{mono} * f = I^{mono} * (PSF * s) \quad (2.31)$$

The rescaled source distribution s in the above equation, is defined as:

$$s = S \frac{z_{od}}{z_{so}} \quad (2.32)$$

where S is the real source distribution, z_{od} is the object-to-detector distance and z_{so} is the source-to-object distance.

The convolution pattern J^{poly} represents the ideal pattern corrected for experimental conditions, taking into account both the limited spatial coherence of the beam and the detector resolution. Both simulations and experimental data showed that the phase contrast signal is affected by the limited spatial resolution of the detector, which results in broader and lower peaks in the signal. A finite source dimension also causes smearing of the peaks in the signal, because of the convolution with the function s . In the case of beam polychromacity, it was noticed that it only broadens the peaks while the effect on the peak position is negligible compared to those of source and detector.

The effects of the source size and detector with a finite spatial resolution on the phase contrast signal in the CAXPCi system were reported in (Olivo and Speller 2007). It was observed that the signal spill-out from a given pixel to its neighbours has a major impact on the effectiveness of the technique, as it reduces the intensity difference between positive and negative peaks in the PC signal, i.e. image contrast. The authors attributed this primarily to light diffusion in the scintillator, which was an integral part of the detector used for the experiments. The effect of the source size was studied by simulating a wire with both a point source and with a Gaussian - distributed source with a full-width at half maximum (FWHM) of 100 μ m. The results show that the loss in image contrast is negligible. The same is then validated experimentally. This proved that the CAXPCi technique can be used with large size x-ray sources, like those used in mammography.

2.2 Digital Tomosynthesis

2.2.1 Introduction

Digital Tomosynthesis (DTS) is a three-dimensional (3D) imaging modality in which an x-ray tube moves above the breast along an angular trajectory (see Figure 2.13a), and a

limited number of angular projections are taken and reconstructed to provide depth information.

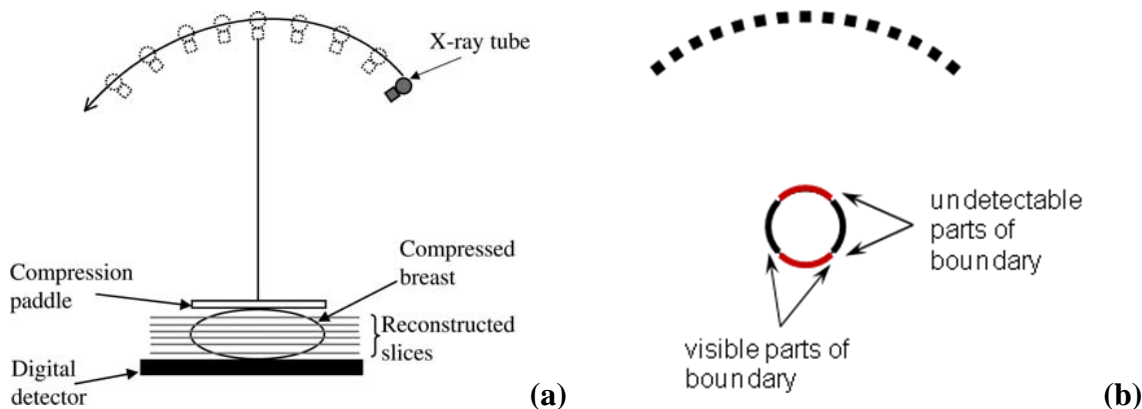


Figure 2.13 Schematic of the tomosynthesis scan (a) and its limitations (b)

Tomosynthesis reconstructions provides high resolution in the transverse plane (i.e. the plane parallel to the compression paddle), while the resolution in the z direction is limited due to the incomplete number of projections available. This is schematically illustrated in Figure 2.13b.

2.2.2 Geometry

Several tomosynthesis geometries exist. The most widely used is the one where the x-ray tube and the detector move in parallel and opposite directions (Dobbins and Godfrey 2003). In this geometry, the relative position of the x-ray tube above the detector, as well as the distance between them, remain fixed at each projection angle, so there is no need to apply corrections for object magnification (Figure 2.14a). Other geometries use a point in the patient (Figure 2.14b and c), or in the space above patient (Figure 2.14d), as the centre of rotation for the x-ray tube (Dobbins and Godfrey 2003). These techniques are called isocentric (as the central point of the rotation is an isocenter). It should be noted that the geometry of the partial isocentric technique (Figure 2.14c) differs from the isocentric method, in that the x-ray tube moves along an arc above the patient, while the detector is shifted along a plane parallel to the imaged planes within the patient. In this chapter only the isocentric geometry will be described in detail, as it is the one that was adopted in this work.

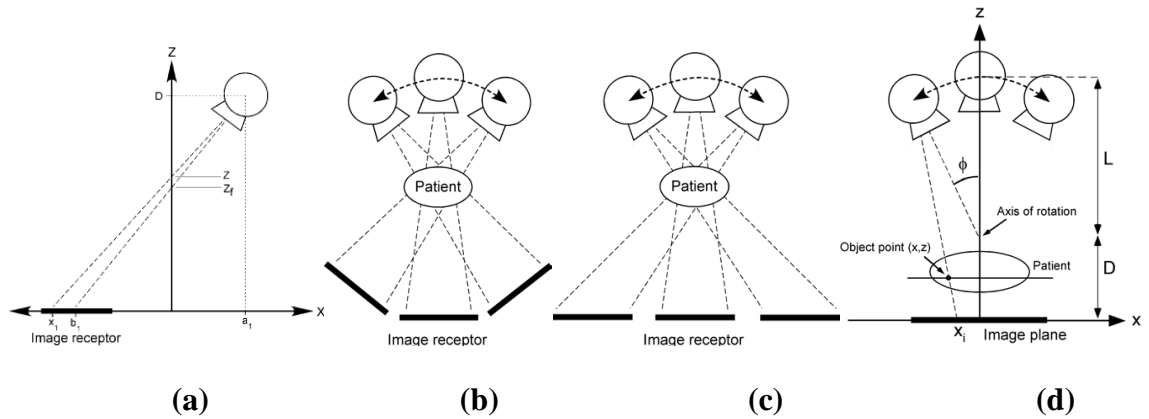


Figure 2.14 Tomosynthesis geometries. (a) parallel opposing motion of the x-ray source and the detector, (b) complete isocentric motion with an isocenter located in the centre of the patient, (c) partial isocentric motion, in which the x-ray tube is rotated within angular range and the detector moves in one plane, (d) partial isocentric motion, in which the detector remains stationary while the x-ray tube moves around a central axis with an isocenter located above the patient (Figures a, b and c adopted from (Dobbins and Godfrey 2003) and figure d adopted from (Niklason et al. 1997)).

In the isocentric geometry, the x-ray tube moves around the patient with the centre of rotation located in the central plane of the patient. The detector follows the movement of the x-ray tube along the same arc but in the opposite direction. This geometry requires some mathematical corrections for the magnification of the structures within the patient which are located in different planes, due to the distance from the focal spot to the plane of interest changing with the tube rotation angle (Dobbins and Godfrey 2003). These problems can be overcome by applying correction algorithms proposed by (Kolitsi et al. 1992). Let us assume that the central point of the rotation of the x-ray tube and detector is located in the isocenter C (Figure 2.15b). The imaged plane within the patient is CA . C_iA_i represents the acquired image plane on the detector active area (image receptor) for a specific gantry angle. C_hA_h is the image plane projected on the axis that is parallel to the plane of interest (imaged plane). In order to project the data acquired at the imaged plane onto the reconstructed image plane on the x axis, the following transformation is used:

$$h = \frac{id}{d \cos \alpha - i \sin \alpha} \quad (2.33)$$

where h is the distance from the projected isocenter point C to projection plane C_h , and i is the distance from the projected isocenter point C to image receptor plane C_i . The reconstructed image plane is calculated for each new angle α . The projected

plane $C_h A_h$ has the same length for all angles. Therefore the final image of the isocenter can be obtained simply by summing all the reconstructed horizontal images acquired in a sequence. The computations become more complicated for the planes other than the plane of the isocenter. In Figure 2.15b the plane QP is at a distance a from the isocenter C. In this case, some extra steps must be taken in order to bring this plane into focus. The first step requires projecting the imaged plane QP on the parallel horizontal x axis $Q_r P_r$. Next, the $Q_r P_r$ plane is shifted by the length of $C_h Q_h$. This shifts the projected position of Q to the centre of the image. The last step takes into account the magnification arising from the different positions with respect to x-ray source. The position r on the plane $Q_r P_r$ of an object projected at h in the horizontal plane is given by:

$$r = \left(h - \frac{ad \sin \alpha}{b \cos \alpha - a} \right) \left(1 - \frac{a}{b \cos \alpha} \right) \quad (2.34)$$

Similarly, a series of images is acquired at different angles of the x-ray tube, and these are added together to create an image of the plane QP.

For simplicity reasons, only horizontal planes were discussed here. A detailed description of the transformations required for planes tilted with respect to the horizontal isocentric plane are given in (Kolitsi et al. 1992).

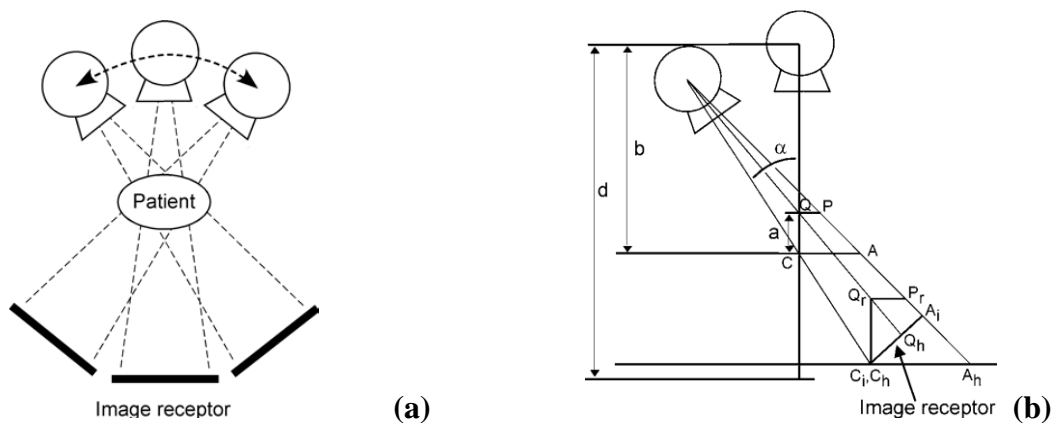


Figure 2.15 Tomosynthesis geometry using a complete isocentric motion (a) and geometric configuration for transforming the complete isocentric geometry into planar Tomosynthesis reconstruction (Figures a adopted from (Dobbins and Godfrey 2003) and figure b adopted from (Kolitsi et al. 1992)).

2.2.3 Reconstruction methods

This chapter introduces the basic concepts of analytical and iterative reconstruction. The main aim of all reconstruction methods is to restore the 3D distribution of a given quantity inside an object given a set of its projections. Although the analytical reconstruction algorithms are widely used in CT and TS, there is also great interest in the iterative reconstruction techniques, which can allow for incorporating a prior knowledge of the sample and better noise management than the analytical techniques.

2.2.3.1 Analytical reconstruction

Analytical reconstruction is the most popular in CT and TS nowadays for several reasons. Its properties have been well understood, it is relatively fast, deterministic and easy to implement. In this chapter, a Fourier slice theorem will be presented, as it provides the mathematical bases for the most commonly used reconstruction technique, i.e. filtered backprojection.

Fourier Slice Theorem

Let assume a two-dimensional (2D) object described by an object function $f(x, y)$. According to the Beer-Lambert law, the measured intensity I transmitted through a material with a thickness x is defined as follows:

$$I = I_0 \exp\left(-\int_L f(x, y)dl\right), \quad (2.35)$$

where I_0 is the incident beam intensity and L is the line along which the beam is attenuated.

By dividing the equation by I_0 and applying a logarithm to both sides, we get a relationship between the line integral value of the object function and the measured values:

$$\int_L f(x, y)dl = -\ln \frac{I}{I_0} \quad (2.36)$$

A projection of the object at a given angle θ and position t on the detector is given by a set of line integrals:

$$P(\theta, t) = \int_L f(x, y) dl \quad (2.37)$$

where the object function $f(x, y)$ represents some property of the object. The function $P(\theta, t)$ is called the Radon transform of the object function $f(x, y)$. The integration in the above equation takes place along the line L , which is defined by:

$$x \cos \theta + y \sin \theta = t \quad (2.38)$$

Although it is possible to measure $P(\theta, t)$ for angles θ ranging from 0 to 2π , it is sufficient to acquire projections for angles from 0 to π , since for a parallel beam the attenuation profiles obtained from the opposite direction of the beam provide the same information.

The fundamental question of the reconstruction problem is how to restore the original object function $f(x, y)$ given the set of projections at every angle, i.e. the sinogram $P(\theta, t)$.

The basic theory behind the analytical reconstruction algorithms is the Fourier Slice Theorem, also known as the central slice theorem. It states that:

The Fourier transform of a parallel projection of an image $f(x, y)$ taken at angle θ gives a slice of the two-dimensional transform, $F(u, v)$ at an angle θ with respect to the u -axis (see Figure 2.16).

In other words, by taking a projection in the space domain $P(t, \theta)$ and Fourier transforming it with respect to the first variable:

$$\hat{f}_{1D}(\omega, \theta) = \int P(t, \theta) e^{-2\pi i(\omega t)} dt, \quad (2.39)$$

one obtains a radial line in the frequency domain (line B in Figure 2.16), given by the 2D Fourier transform of $f(x, y)$:

$$\hat{f}_{2D}(u, v) = \iint f(x, y) e^{-2\pi i(ux+vy)} dx dy \quad (2.40)$$

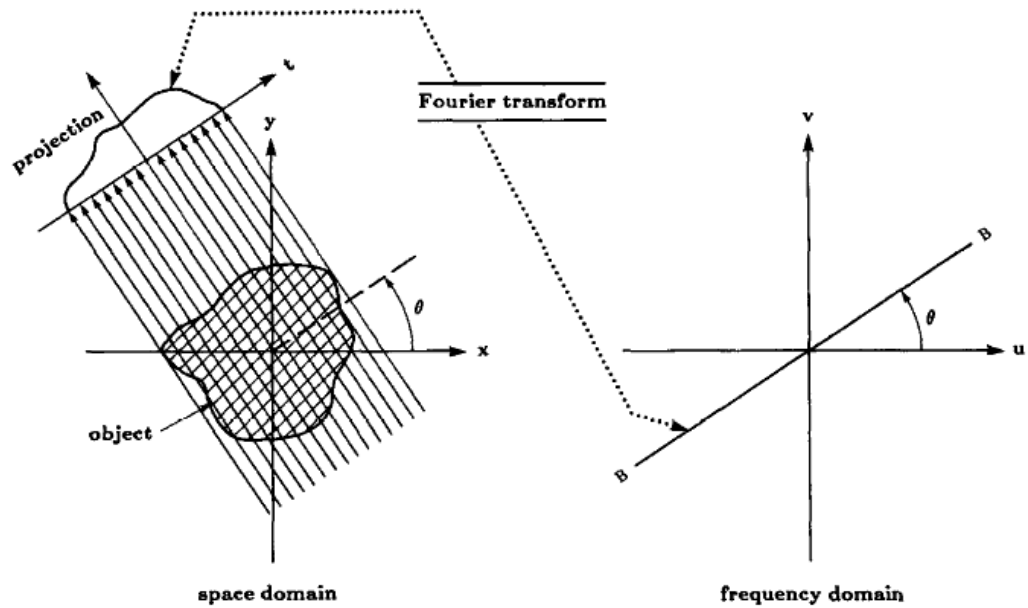


Figure 2.16 The Fourier slice theorem. Figure adapted from (Kak and Slaney 2001).

The next step is to apply an inverse Fourier transform on the radial lines in order to restore the object function $f(x, y)$:

$$f(x, y) = \hat{f}_{2D}^{-1} \hat{f}_{2D} [f(x, y)] = \iint \hat{f}_{2D} [f(u, v)] \exp(i2\pi(ux + vy)) du dv \quad (2.41)$$

The equation above provides a straightforward method for tomographic reconstruction of the object function. However, this method alone does not lead to satisfactory results. This is due to the fact that in practice the number of acquired projections is limited, which also means that the number of radial lines in the frequency space is limited. Moreover, in order to apply the inverse Fourier transform, the data needs to be distributed on a square grid rather than on radial lines (Figure 2.17). This implies that an interpolation (ex. nearest neighbour, linear, etc.) is needed to determine the values on a square grid from radial points. From Figure 2.17, it is clear that for larger image frequencies the data is distributed more sparsely, and the interpolation error is higher than for low image frequencies.

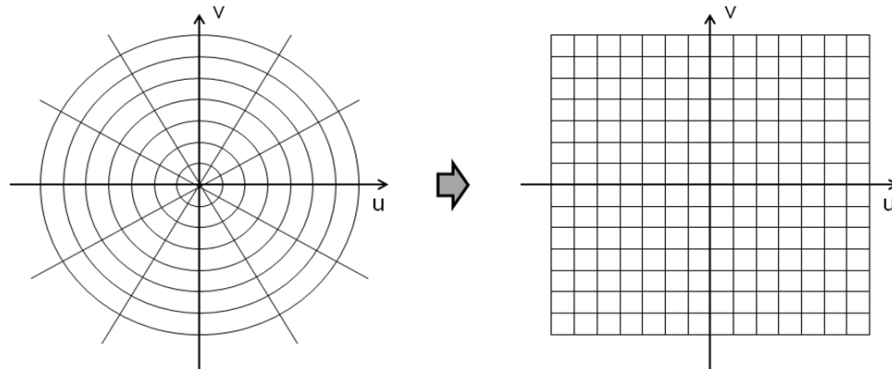


Figure 2.17 The object function in the Fourier domain sampled along radial lines and a Cartesian square grid.

Filtered Backprojection (FBP)

The complications due to gridding and two dimensional Fourier transforms are avoided in the reconstruction method called Filtered Backprojection (FBP). The FBP is a two – step process: first the projections are filtered in the frequency domain, and then they are backprojected, hence the name of the technique. The FBP algorithm was firstly developed for the parallel beam geometry, but it can be adapted also for the fan-beam and cone-beam geometries. A short description of the three approaches will be given below.

The inverse Fourier transform of the object function given by equation (2.41), can be modified from Cartesian coordinate system to a polar one by using:

$$u = \omega \cos \theta \quad (2.42)$$

$$v = \omega \sin \theta \quad (2.43)$$

so that it becomes:

$$f(x, y) = \int_0^\pi \left[\int_{-\infty}^{\infty} \hat{f}(\omega, \theta) |\omega| \exp(i2\pi\omega t) d\omega \right] d\theta \quad (2.44)$$

This equation provides a full reconstruction method. The inner integral is the inverse Fourier transform and the outer integral is the backprojection. The equation above is usually done in three steps to simplify the calculations. First, a 1D Fourier transform of the projection data is calculated at each angle:

$$\hat{f}(\omega, \theta) = \int P(t, \theta) e^{-2\pi\omega t} dt, \quad (2.45)$$

second, this equation is multiplied by a ramp filter $|\omega|$ in the frequency domain, in order to get filtered projections:

$$Q(t, \theta) = \int \hat{f}(\omega, \theta) |\omega| e^{i2\pi\omega t} d\omega \quad (2.46)$$

Finally the inverse Fourier transform of the filtered line integrals are taken and the filtered projections are backprojected:

$$f(x, y) = \int_0^\pi Q(t, \theta) d\theta. \quad (2.47)$$

An ideal ramp filter is given by:

$$H(\omega) = \begin{cases} |\omega| & \text{if } |\omega| < W \\ 0 & \text{otherwise} \end{cases} \quad (2.48)$$

In practice, this filter is usually cut off at a frequency $\omega = 1/2\Delta k$ (where Δk is the sampling distance), corresponding to the limit of a “useful” Fourier content. Such filter is called a Ram-Lak filter, and in practice a smoothing window (Hann, Hamming, cosine, Shepp-Logan, etc.) is applied to it to suppress the high frequencies to avoid image artefacts.

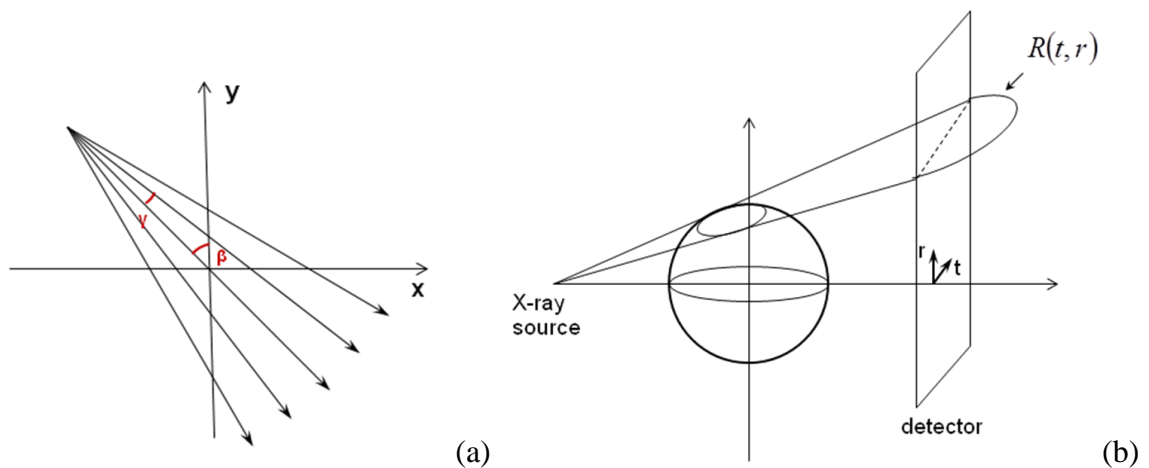


Figure 2.18 Fan- beam (a) and cone – beam (b) geometries. Figures adapted from (Kak and Slaney 2001)

Fan beam and cone beam

So far we assumed a parallel beam geometry which, can be obtained with synchrotron radiation or by moving an x-ray source above the sample in a direction parallel to a given object plane. Most modern clinical CT scanners, however, use either fan beam or

cone beam geometries (see Figure 2.18). The fan beam reconstruction has not been used in this thesis, but it is shortly summarized here for the completeness' sake.

In order to take into account the divergence of the beam, the FBP algorithm needs to be modified depending on the detector used for the acquisition. Two types of detector can be used: planar with equidistant pixels or curved with equiangular pixels. Although both types of detectors are widely used in different CT applications, planar detectors are more commonly used in clinical CT imaging. Therefore in this thesis only a brief description of fan and cone beam CT imaging will be given for planar detectors only.

When a fan beam is used, one needs to modify equations (2.45), (2.46) and (2.47) in order to take into account the geometrical difference from the parallel beam acquisition.

First, a correction factor $\frac{R}{\sqrt{R^2 + t^2}}$ needs to be applied to each projection to take into account the divergence of the fan beam:

$$\hat{f}(\omega, \theta) = \int \frac{R}{\sqrt{R^2 + t^2}} P(t, \theta) e^{-2\pi i \omega t} dt \quad (2.49)$$

where R is the distance between the source and the centre of the object coordinate system. The filtering operation is the same as for the parallel beam, except from the fact that one filters already pre-weighted projections.

The second correction is a weight applied in the backprojection process. In the case of a planar detector one has:

$$f(x, y) = \int_0^{2\pi} \frac{R^2}{U^2(x, y, \theta)} Q(t, \theta) d\theta \quad (2.50)$$

where $U^2(x, y, \theta)$ is the distance between the source and a point projected on the central ray; this can be calculated as $U^2(x, y, \theta) = R - x \sin \theta + y \cos \theta$, while t is given by $t = R(x \cos \theta + y \sin \theta) / (R - x \sin \theta + y \cos \theta)$.

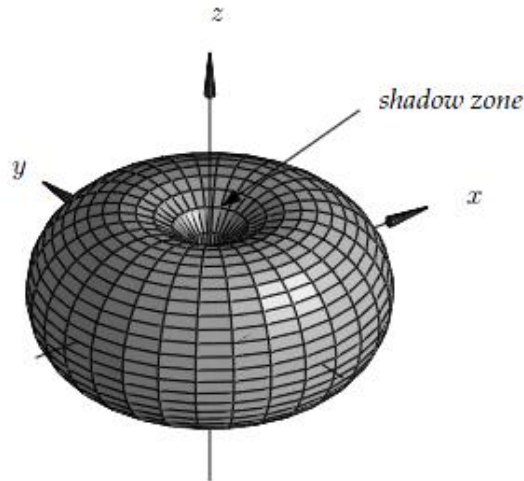


Figure 2.19 Radon data for a cone beam geometry. Figure adopted from (Turbell 2001)

The cone beam reconstruction is more complicated than parallel or fan-beam reconstructions. This is because the projection data $P(\theta, t, r)$ is now dependent not only on the projection angle θ , but also on the horizontal and vertical positions t and r on the detector. Figure 2.18b shows a schematic drawing of the cone beam geometry. The use of the cone beam is preferred in the CT acquisition as it allows imaging a larger area for each projection, meaning that a much shorter time is required to perform a full CT scan. For a circular source trajectory, it is possible to get an exact Radon dataset only for a donut shaped region (see Figure 2.19). At the z -axis, a double cone-like region is missing. This region is called the shadow zone. The missing information prevents an exact reconstruction, which, according to Tuy and Smith, can only be obtained if all planes intersecting the object intersect the trajectory of the source at least once. In order to meet the Tuy - Smith condition, one needs to move the source along the z -axis along a helical trajectory.

The FDK algorithm is currently the most commonly used for cone-beam reconstruction. It was firstly published by Feldkamp, Davis and Kress in (Feldkamp et al. 1984). The algorithm is an extension of the FBP to a 3D space. Similarly to FBP, it can be accomplished in three steps summarized in the following equations:

$$\hat{f}_\theta(\omega, r) = \int \frac{R}{\sqrt{R^2 + t^2 + r^2}} P(t, r) e^{-2\pi\omega t} dt \quad (2.51)$$

$$Q_\theta(t, r) = \int \hat{f}(\omega, r) \omega e^{i2\pi\omega t} d\omega \quad (2.52)$$

$$f(x, y, z) = \int_0^{2\pi} \frac{R^2}{U^2(x, y, \theta)} Q_\theta(t, r) d\theta \quad (2.53)$$

where t and $U(x, y, \theta)$ were already defined for the fan-beam reconstruction, and r can be calculated as $r = zR/(R - x \sin \theta + y \cos \theta)$.

2.2.3.2 Iterative reconstruction

Iterative methods are an alternative to analytical reconstructions. They can provide high quality reconstructions when only a limited number of projections are available, or when the sampling of the projections is not equiangular. It is clear that Tomosynthesis, which by definition entails the use of a limited number of projections, can benefit significantly from iterative methods. Iterative methods can also provide reconstructions with better signal to noise ratio compared to analytical algorithms. It is possible to make the model more realistic by adding certain physical effects like scattering, beam hardening, etc. These advantages come however at a cost of a longer computational time. Therefore they are rarely used to reconstruct full CT data. In case of Tomosynthesis, due to the limited number of projections (i.e. smaller datasets), the reconstruction time is often considered acceptable.

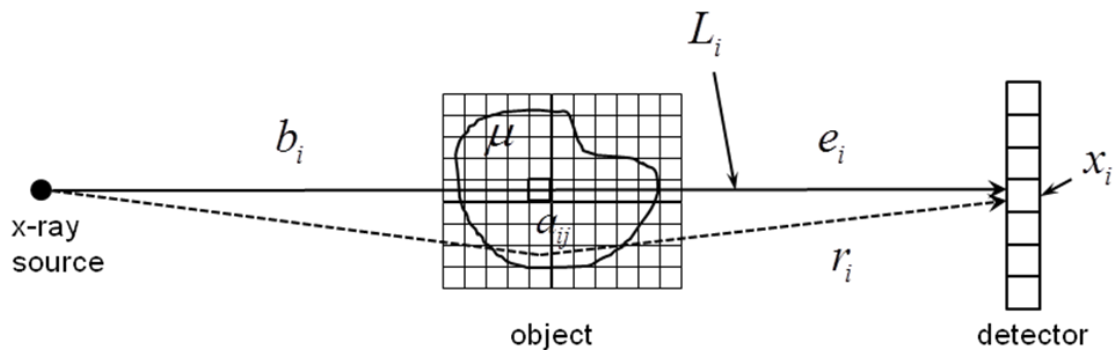


Figure 2.20 System model.

Let us first consider an imaging setup as shown in Figure 2.20. A random number of photons b_i in the i th ray are generated by a point source and pass through an object. Let x_i denote a random number of photons detected by the i th detector element. According to the Beer - Lambert law, the relationship between x_i and b_i is given by:

$$x_i = b_i \exp\left(-\int_L f(x, y, z) dl\right) \quad (2.54)$$

In transmission tomography, the object function f denotes the spatial distribution of the attenuation coefficient. In theory this is a continuous function. In practice, due to a finite number of pixels, its discrete values are calculated. Thus, the object function can be approximated with:

$$f(x, y, z) \approx \sum_{j=1}^M f_j \xi_j(x, y, z), \quad (2.55)$$

where $\vec{f} = \{f_j; j=1, \dots, M\}$ is the object vector, with f_j the mean value of $f(x, y, z)$ in the j th voxel, and $\xi_j(x, y, z)$ is a basis function. The most common choice for this function is a square pixel basis, although different functions exist – for example: natural pixels (Hsieh et al. 1996; Hsieh et al. 1996) or radial basis functions (Carr et al. 2001). Using this, the line integral from equation (2.51) can be approximated with:

$$\int_L f(x, y, z) dl \approx \sum_{j=1}^M f_j \int_L \xi_j(x, y, z) dl, \quad (2.56)$$

where the line integral along the i th ray through the j th basis function is usually denoted by a_{ij} . In practice, a set of a_{ij} values results in a $N \times M$ matrix A . By using this notation, equation (2.54) becomes:

$$x_i = b_i \exp\left(-[A\vec{f}]_i\right), \quad (2.57)$$

where

$$[A\vec{f}]_i = \sum_{j=1}^M a_{ij} f_j \quad (2.58)$$

In order to find the object function, one needs to solve a system of linear equations:

$$\vec{A} \cdot \vec{F} = \vec{P} \quad (2.59)$$

where \vec{P} is a column vector of ray sums p_i retrieved from the projection images by:

$$p_i = -\ln\left(\frac{x_i}{b_i}\right) \quad (2.60)$$

In theory one could solve the system of equations in (2.59) analytically. In practice, however, this would lead to highly noisy reconstructions due to the noise present in the projections, and would be computationally inefficient due to the large size of the matrix.

Algebraic reconstruction

An algebraic reconstruction technique (ART) was one of the first iterative reconstruction methods to be developed (Gordon et al. 1970). It aims at solving the system of linear equations in (2.59) iteratively. The process of updating the current estimate f_i^n is done according to the following formula:

$$f_j^{n+1} = f_j^n + \frac{x_i - \sum_{j=1}^N f_{ji}^n}{N}, \quad (2.61)$$

where f_j^{n+1} is a new estimate, x_i is the measured number of counts for ray i , and N is the number of pixels along ray i .

From the above equation it is clear that the iterative process involves two major steps. First, one has to compare the measured projections to the estimated projections and subtract the latter from the former. Then, the correction term must be added to the current estimate.

The process expressed by the above equation is repeated for every detector pixel and for every projection angle, until a sufficient convergence is achieved. An example of the ART iterative process is illustrated in Figure 2.21 for a simple 2x2 image. In this case, due to the small number of pixels, one iteration is sufficient to provide an exact solution. For larger objects more iterations are obviously needed.

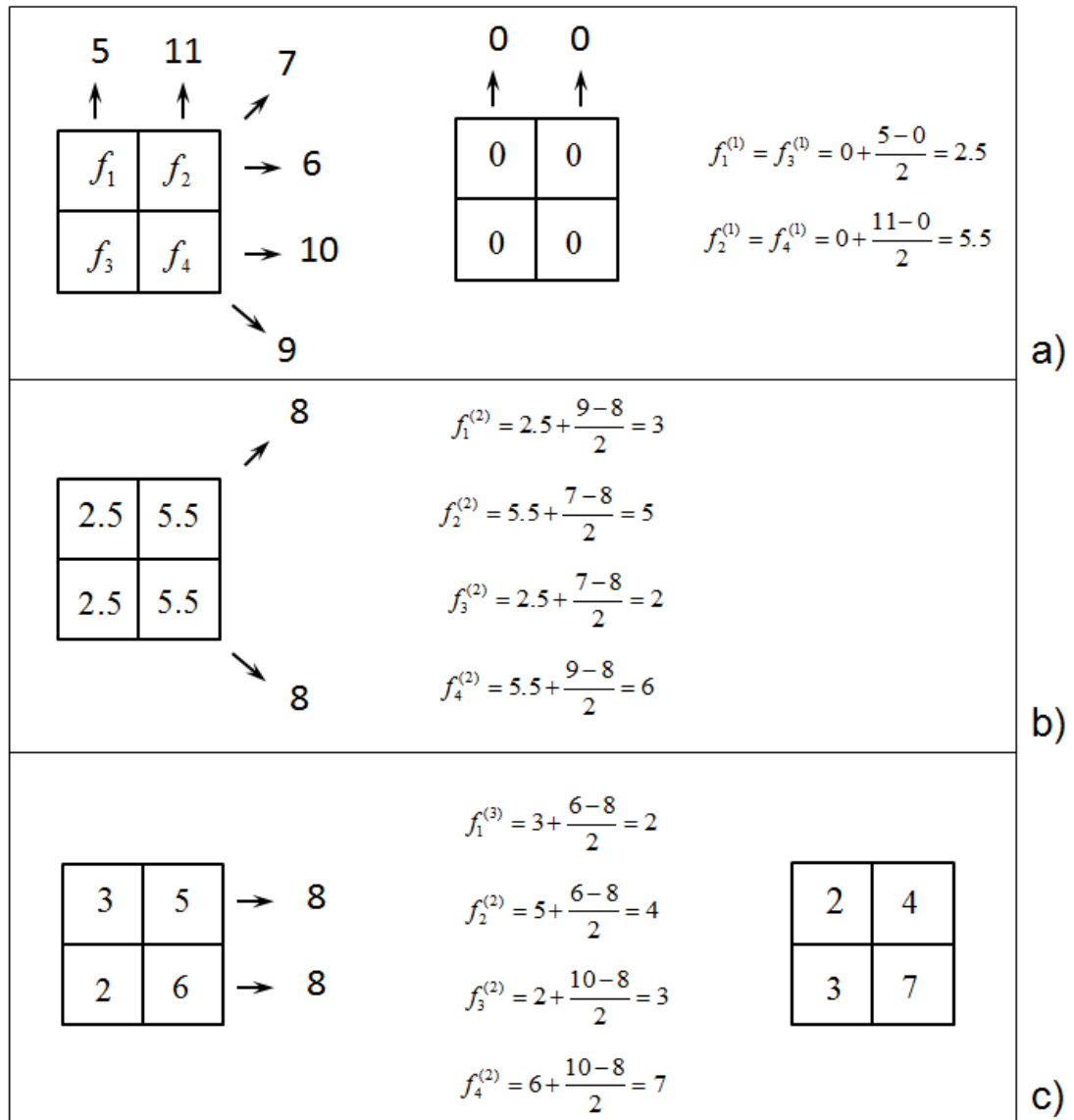


Figure 2.21 Example of an algebraic reconstruction for an array of 2x2 pixels. a) The problem is to find values $f_1 - f_4$ given six projected values; in first step an initial estimate (zeros) is projected, the ART algorithm is applied and pixel values are updated, b) the process is repeated for oblique rays, and d) for horizontal rays; the solution is obtained after 1 iteration

Statistical reconstruction

Statistical reconstruction methods provide another approach to iterative reconstruction. This reconstruction takes into account the stochastic nature of the x-ray transmission process, i.e. the statistical noise in the projections in the case of low x-ray flux. Moreover, it can incorporate *a priori* physical information about the object in the form of constraints. The reconstruction process involves two steps: the definition of an objective function and its optimization. One can choose many different objective functions, for example: minimum least square error, maximum likelihood or its surrogates, and others. Likewise, many different ways to optimize these functions exist (steepest ascent, steepest descent, conjugate gradients, ...).

A discrete forward model is a mathematical model that describes the imaging system. Let us again consider the imaging setup from Figure 2.20. Ideally, this system is correctly described by equation (2.51). Let us repeat it here for convenience:

$$x_i = b_i \exp\left(-\int_L f(x, y, z) dl\right) \quad (2.62)$$

The above equation is valid for an ideal case only (denoted by ray e_i in Figure 2.20), i.e. when no noise is present in the imaging system. In practice, one needs to take into account the scatter effects (denoted by ray r_i in Figure 2.20). Thus, the equation (2.62) becomes:

$$x_i = e_i + r_i \quad (2.63)$$

At this stage one needs to choose a statistical model. The most commonly used are the Poisson noise models and the Gaussian models.

The Poisson model assumes that e_i and x_i in equation (2.63) follow the Poisson distribution. Thus, the variable x_i is said to have a Poisson distribution with an expected value of x_i , i.e. \hat{x} , if the probability mass function $p(\vec{x} | \vec{f})$ of having observed a set of projections \vec{x} determined by the object function \vec{f} is given by:

$$p(\vec{x} | \vec{f}) = \prod_{i=1}^P \frac{\hat{x}_i^{x_i} e^{-\hat{x}_i}}{x_i!}, \quad (2.64)$$

where x_i and \hat{x}_i are elements of the matrix of measured data $x = \{x_i, i = 1, \dots, M\}$ and expected values $\hat{x} = \{\hat{x}_i, i = 1, \dots, M\}$, respectively. The equation above leads to a forward model, which, following the notation of (Fessler and Erdogan 1998), can be written as:

$$x_i \sim \text{Poisson}\{\hat{x}_i + \hat{r}_i\} \quad (2.65)$$

The expected number of detected photons \hat{x}_i for an image \vec{f} is given by:

$$\hat{x}_i = b_i \cdot \exp\left(-\sum_{j=1}^J a_{ij} f_j\right), \quad (2.66)$$

where b_i is the number of photons in the white field, i.e. when no sample is present in the beam, and a_{ij} an intersection length of projection line i with pixel j . The measured value x_i differs from the expected value \hat{x}_i due to the quantum nature of photons. All statistical methods aim to describe x_i as a function of \hat{x}_i . Two main steps are needed in the reconstruction process. First, one needs to define an objective function (e.g. maximum likelihood, minimum least squares error, etc), and then chose a method to optimise it (e.g. steepest ascent, conjugant gradient, etc.). The optimization is usually done iteratively. Similarly to ART, one starts with a random image (initial guess), and compares it with the measured image. Next, an error is calculated and the image is corrected accordingly. The corrected image is then subtracted from the current reconstruction. This process is repeated until a satisfactorily small error is achieved.

In the next section, a specific maximum likelihood approach will be discussed and its suitable implementation in the form of a ‘‘Separable Paraboloidal Surrogates’’ algorithm will be described, as it was the one used to reconstruct the experimental data obtained in this work.

Maximum likelihood

The ML reconstruction aims to find, for a set of measured projections x , the values of the object function f that maximizes the probability $p(\vec{x} | \vec{f})$. It is more convenient to maximize the logarithm of the probability, which is a monotonic function rather than the probability itself. The log-likelihood function from equation (2.64) becomes:

$$\log p(\vec{x} | \vec{f}) = \sum_{i=1}^n x_i \log \hat{x}_i - \hat{x}_i - \log(x_i!), \quad (2.67)$$

where $\hat{x}_i = b_i \exp(-[A\vec{f}]_i) + \hat{r}_i$. The last term in the above equation does not depend on \vec{f} and can be ignored. The log-likelihood function can be rewritten as:

$$L = \sum_{i=1}^n x_i \log(b_i \exp(-[A\vec{f}]_i) + \hat{r}_i) - (b_i \exp(-[A\vec{f}]_i) + \hat{r}_i) \quad (2.68)$$

The reconstruction problem is to maximize the log-likelihood from equation (2.67), which mathematically can be written as:

$$\hat{f} = \arg \max_{\vec{f} \geq 0} p[\vec{x} | \vec{f}] = \arg \max_{\vec{f} \geq 0} L(\vec{f}) \quad (2.69)$$

In order to maximize the log-likelihood function one can use an expectation maximization (EM) iterative method (Lange and Carson 1984). Historically, this was one of the first approaches to maximize $L(\vec{f})$. EM refers to two steps at each iteration: an expectation step and a maximization step. A detailed description of this method can be found in (Lange and Carson 1984). The ML – EM method has not been used widely for clinical reconstructions due to heavy computational load and low speed of convergence. The method requires the calculation of a large number of exponents at each iteration. Another problem with this algorithm is that it does not work properly for a limited angle dataset, as in that case it provides extremely noisy images. This happens because the number of counts is low, leading to a low signal to noise ratio in the projections. In order to overcome the limitations of the ML – EM method, one can add *a priori* information about the object. This is the Bayesian reconstruction approach firstly proposed by Geman and Geman in (Geman and Geman 1984); it will be briefly described below.

One type of Bayesian estimate is a maximum *a posteriori* (MAP) estimate. The goal is to find an estimate \hat{f} of the true map f of the object, i.e. the value of f for which the *a posteriori* probability $p(\vec{f} | \vec{x})$ is greatest:

$$\hat{f} = \arg \max_{\vec{f}} p(\vec{f} | \vec{x}) \quad (2.70)$$

The above equation can be modified by using Bayes' rule given by (Geman and Geman 1984):

$$p(\vec{f} | \vec{x}) = \frac{p(\vec{x} | \vec{f})p(\vec{f})}{p(\vec{x})} \quad (2.71)$$

and by applying a logarithm to both sides:

$$\log p(\vec{f} | \vec{x}) = \log p(\vec{x} | \vec{f}) + \log p(\vec{f}) - \log p(\vec{x}) \quad (2.72)$$

by neglecting the term which does not depend on the object, one obtains an objective function $\Phi(\vec{f})$:

$$\Phi(\vec{f}) = \log p(\vec{x} | \vec{f}) + \log p(\vec{f}) \cong L(\vec{f}) - \beta R(\vec{f}), \quad (2.73)$$

where $L(f)$ is a log-likelihood function, and $\beta R(f)$ is a roughness penalty function where β is a regularization parameter. The log-likelihood function for the independent transmission data is given by:

$$L(\vec{f}) = \sum_{i=1}^P x_i \log \left(b_i \exp(-[\vec{A}\vec{f}]_i) + \hat{r}_i - (b_i \exp(-[\vec{A}\vec{f}]_i) + \hat{r}_i) \right), \quad (2.74)$$

where b_i is the incident number of photons and \hat{r}_i is the mean number of scattered photons. The penalty function is introduced to take into account any *a priori* information about the projections. The role of the penalty function is to favour reconstructions that are piecewise smooth. This process is called regularization. The trade-off between the noise and spatial resolution can be controlled by changing the parameter β . If a high value of β is set, the noise will be reduced at a cost of reduced spatial resolution.

The log-likelihood function above depends on \vec{f} only through its projections $[\vec{A}\vec{f}]_i$ and can be rewritten in a more compact form:

$$-L(\vec{f}) = \sum_{i=1}^P k_i([\vec{A}\vec{f}]_i), \quad (2.75)$$

where

$$k_i(l) = x_i \log(b_i e^{-l} + \hat{r}_i) - (b_i e^{-l} + \hat{r}_i) \quad (2.76)$$

There are a number of different methods to maximize the penalized objective function. One way is a separable paraboloidal surrogate (SPS) algorithm.

Separable Paraboloidal Surrogates Algorithm

The objective function in the form presented in equation (2.73) is difficult to maximize. Therefore Fessler and Erdogan (Erdogan and Fessler 1999) proposed to replace Φ with a global surrogate function ϕ that would be easier to maximize. In this section, a description of the SPS algorithm will be provided, as it forms the basis of the reconstruction technique used in this work.

Let \vec{f}^n be the estimate of the distribution of the object parameter, and let $\phi(\vec{f}; \vec{f}^n)$ be the surrogate function to be maximized. The basic idea of the algorithm is illustrated in Figure 2.22.

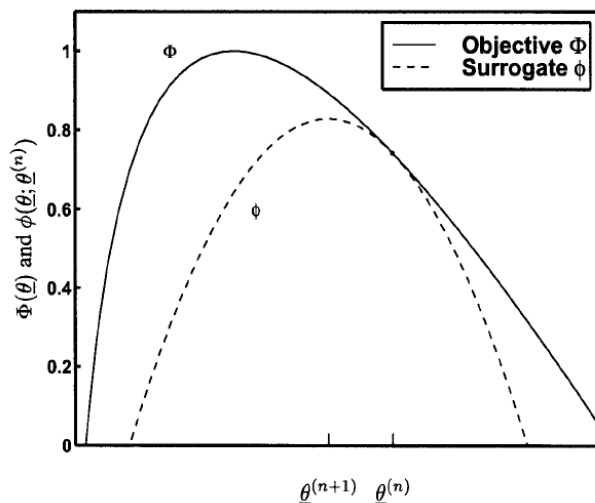


Figure 2.22 Optimization transfer in 1D. Figure adapted from (Sonka (2009))

The chosen surrogate function must satisfy the following conditions:

$$1) \quad \phi(\vec{f}; \vec{f}^n) = \Phi(\vec{f}^n) \quad (2.77)$$

$$2) \quad \frac{\partial}{\partial f_j} \phi(\vec{f}; \vec{f}^n) \Big|_{\vec{f}=\vec{f}^n} = \frac{\partial}{\partial f_j} \Phi(\vec{f}) \Big|_{\vec{f}=\vec{f}^n} \quad (2.78)$$

$$3) \quad \phi(\vec{f}; \vec{f}^n) \leq \Phi(\vec{f}), \forall \vec{f} \geq 0 \quad (2.79)$$

The first condition ensures that the surrogate function is equal to the original objective function at the current estimate. The second condition implies that the surrogate function is tangent to the original objective function at the current estimate. Finally, the

last condition states that the surrogate function lies below the objective function for all non-negative values of \vec{f} .

The surrogate function proposed by Fessler is constructed from two separate surrogates for the log-likelihood part $L(f)$ and the penalty part $R(f)$; hence the algorithm is called “separable” paraboloidal surrogates. The two surrogate functions can be treated separately, which means that the pixels can be updated in parallel. This process tends to be computationally more efficient than a sequential update of the pixels, but at a cost of a slower convergence.

The surrogate function for the log-likelihood part of the objective function is created from a sum of 1D surrogate functions $k_i(l)$, where $l_i = [\vec{A}\vec{f}]_i$. For convenience, the $l_i^n = [\vec{A}\vec{f}^n]_i$ is an estimate of the i th line integral of the object parameter at the n th iteration. It has been shown in (Erdogan and Fessler 1999) that a parabola given by the following formula is a good candidate for the surrogate function:

$$q(l; l_i^{(n)}) = h(l_i^{(n)}) + \dot{h}(l_i^{(n)})(l - l_i^{(n)}) - \frac{c}{2}(l - l_i^{(n)})^2 \quad (2.80)$$

In the equation above, $c_i(l_i^{(n)})$ refers to the curvature of the parabola, and \dot{h} denotes the first derivative of the function h .

A new surrogate function is tested to satisfy the above three conditions, and a total surrogate function is formed by summation of all single parabolas $q(l; l_i^{(n)})$:

$$Q(\vec{f}; \vec{f}^n) \equiv \sum_{i=1}^N q_i([\vec{A}\vec{f}]_i; [\vec{A}\vec{f}^n]_i) \quad (2.81)$$

The new objective function becomes:

$$\phi(\vec{f}; \vec{f}^n) = Q(\vec{f}; \vec{f}^n) - \beta R(\vec{f}) \quad (2.82)$$

An algorithm that maximizes $\phi(\vec{f})$ will also monotonically maximize the objective function. There are two main choices to be done in a paraboloidal surrogates method. First, one needs to choose a proper curvature and consequently the function $\phi(\vec{f}; \vec{f}^n)$, which then needs to be maximized. These two steps take place for each iteration. Details on how to choose a proper curvature can be found in (Erdogan and Fessler 1999).

The penalty function $R(\vec{f})$ is given by:

$$R(\vec{f}) = \sum_{j=1}^P \sum_{k=1}^P \omega_{jk} \Psi(f_j - f_k) \quad (2.83)$$

where $\Psi(f_j - f_k)$ denotes a potential function.

A number of possible functions have been proposed in literature for the choice of the penalty function $R(\vec{f})$. A popular choice is a Tikhonov function, in which the potential function is quadratic, i.e. $\Psi(t) = t^2 / 2$, and its variants (Tikhonov 1963; Arridge et al. 1993; Pogue et al. 1999). These regularization methods reduce high-frequency noise and work well for homogeneous objects. In case of a heterogeneous object they tend to penalize the discontinuities present in the object (Douiri et al. 2005). This problem was addressed by using total variation (TV) method (Rudin et al. 1992). The potential function in the TV method is given by a parabola function $\Psi(t) = \sqrt{|t|^2 + \varepsilon^2}$, where ε is a scale adjusted at each iteration. This technique preserves edges well. However, it tends to produce images that are piecewise constant in the presence of noise (Douiri et al. 2005). This means that fine details in the reconstructions may disappear and that the image may look “blocky” due to the fact that edges may give “staircase” effects. The solution to this would be to choose a function, the properties of which would give an intermediate effect between a quadratic and a hyperbolic function. A Huber function smoothes the homogeneous parts of the image and preserves the edges. This function is given by:

$$\Psi(t) = \begin{cases} t^2 / 2 & |t| \leq \varepsilon \\ \varepsilon |t| - \varepsilon^2 / 2 & |t| > \varepsilon \end{cases} \quad (2.84)$$

Least Squares Methods

Log-likelihood for the Poisson case is not the only possibility for an objective function. The normal (Gaussian) distribution is also a possibility to model the x-ray data. In this case the probability density $p(\vec{x} | \vec{f})$ is given by:

$$p(\vec{x} | \vec{f}) = \exp\left(\frac{-\|A\vec{f} - \vec{x}\|_2^2}{2\sigma^2}\right) \quad (2.85)$$

The aim of the reconstruction is then to minimize the squared difference between acquired data x_i and the result of the forward model $[Af]_i$, that is:

$$\hat{f} = \arg \min_f \|Af - x\|_2^2 \quad (2.86)$$

where $\| \cdot \|$ denotes the Euclidean norm.

The above method provides a least squares (LS) solution. If a regularization term $\beta R(\vec{f})$ is added in equation (2.84), then the method is called a penalized least squares (PLS) algorithm. The regularization assumes smoothness of the function to reconstruct and thus penalizes the roughness of the reconstructed image. Similar choices for the penalty function can also be made here, as mentioned previously for the SPS method.

Conjugate Gradient Method

One way to find a solution to equations (2.82) and (2.86) is to use a conjugate gradient (CG) iterative method. This can be used to solve large systems of linear equations that would be time consuming to solve using direct methods. In the case of transmission tomography, one would like to compare the computed projections with the measured ones. For some images this difference is small, for others it can be large. One way to schematize how the CG method works is to imagine a terrain with mountains and valleys, as shown in Figure 2.23. The high and low points of this land correspond to the differences between computed and actual projections as a function of the image. The goal is to find the point for which the difference is the smallest (point C in Figure 2.23), i.e. the one with the lowest altitude. This should be done in as small a number of steps as possible. One way to do this is to follow the steepest descent, i.e. the direction in which the gradient has the highest (negative) value. One starts from an arbitrary point (point A in Figure 2.23), which represents an initial estimate for the image, and moves along the steepest descent (arrows), to first find point B, and finally point C, which is the solution. The procedure can be mathematically expressed as:

$$f^{n+1} = f^n + \alpha^n r^n \quad (2.87)$$

where f^n and f^{n+1} are the current and the new estimates, respectively; r^n is called residual and it is a vector corresponding to a new direction of the steepest decent; α^n is a weighting factor indicating the step length. Suppose we wanted to minimize a quadratic function given by the following formula:

$$g(f) = \frac{1}{2} f^T A f - x^T f + c \quad (2.88)$$

The gradient of this function can be calculated as:

$$\nabla g(f) = g'(f) = \frac{1}{2} A^T f + \frac{1}{2} A f - x \quad (2.89)$$

and, if A is symmetric, the above equation is reduced to:

$$g'(f) = A f - x \quad (2.90)$$

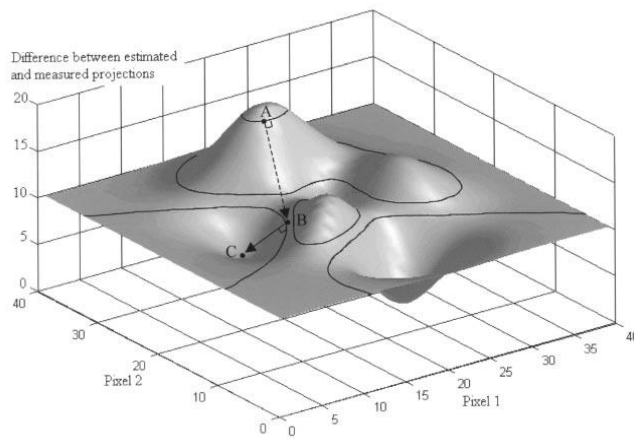


Figure 2.23 Schematic of a basic principle of gradient algorithms. Vertical axis corresponds to a difference between estimated and measured projections. Figure adopted from (Bruyant 2002)

The procedure that chooses α to minimize g along a line is called a line search. Function g is minimized where the projection is zero, i.e. where the gradient is orthogonal to the line search. α can be calculated from the following formula (Shewchuk and Morton 1994):

$$\alpha^n = \frac{(r^n)^T r^n}{(r^n)^T A r^n} \quad (2.91)$$

The residual r^n is calculated at each iteration step as: $r^n = x - A f^n$. The steepest descent algorithm usually requires a lot of iterations to find the solution. To improve this, one can use a r^n the direction of which is not opposite to the gradient at the current location, but to a combination of this gradient and the gradient from the previous step. In other words, the search direction is constructed by conjugation of the residuals (Shewchuk and Morton 1994). This approach is known as a conjugate gradient

algorithm. The first step is performed in the same direction as in the steepest gradient algorithm, i.e.:

$$d^0 = r^0 = x - Af^0 \quad (2.92)$$

The search for direction in the next iteration d^{n+1} is given by:

$$d^{n+1} = r^{n+1} + \beta^{n+1} d^n, \quad (2.93)$$

where $\beta^{n+1} = \frac{\left((r^{n+1})^T r^{n+1} \right)}{\left((r^{n+1})^T r^n \right)}$.

2.2.3.3 The choice of the best reconstruction algorithm

A choice of the best reconstruction algorithm is not always easy. The general preference is to use an analytical reconstruction method such as the FBP. This is because this technique has been well known and it is fast and robust. It gives superior results when a dense angular sampling is performed and when there is little or no noise in the imaging system. For other cases, in which there is a significant contribution of the noise to the final image and some angles are missing or there is a limited angular range, one should consider using an iterative statistical algorithm to reconstruct the data. There are five choices which can be made to create a fully working reconstruction method (Fessler, 2008). These involve the following: object parameterization, system physical model, statistical model, cost function and algorithm. These choices depend strictly on the application. An ideal reconstruction method needs to fulfil a number of requirements (Fessler, 2008). Firstly, it needs to be stable and converge quickly, which means that the f^n converges to \hat{f} in as few iterations as possible and also if the reconstruction process is run indefinitely. Depending on the statistical model used and the complexity of the incorporated physical model, the cost function can be difficult to optimize. Therefore it may be easier to firstly optimize a more convenient surrogate function (as done in the case of the SPS method) before finding a global optimizer. Secondly, the algorithm should be fast and robust, i.e. require minimal computation per iteration and be insensitive to finite numerical precision. Most reconstruction methods are intended to be used in clinical environments, so they should be user friendly. A good algorithm would also be easy to program and debug.

2.3 Image quality evaluation

In conventional digital breast tomosynthesis, the quality of an image is usually evaluated by means of two parameters: the contrast to noise ratio (CNR) and the artefact spread function (ASF). In this chapter, both parameter will be defined and extended to the case of phase contrast imaging.

2.3.1 Contrast-to-Noise Ratio (CNR)

In conventional absorption-based imaging, the CNR_{ABS} is calculated as the difference between the intensity value of a feature $I_{feature}$ and the intensity value of the background I_{bg} , divided by the standard deviation of the intensity values of the background σ_{bg} , i.e. $CNR_{ABS} = (I_{feature} - I_{bg}) / \sigma_{bg}$. Phase contrast images are characterized by intense positive and negative peaks; hence the contrast is redefined on the basis of the difference between maximum and minimum intensities ($C = (I_{max} - I_{min}) / I_{bg}$), and the CNR consequently redefined as:

$$CNR_{PC} = \frac{I_{max} - I_{min}}{\sigma_{bg}} \quad (2.94)$$

2.3.2 Artefact Spread Function (ACR)

Due to the limited number of angles, tomosynthesis images contain ghosting artefacts observed in planes other than the focus plane. These artefacts are more pronounced in the planes that are closer to the plane in focus, and spread out in the other planes. The Artefact Spread Function (ASF) proposed by (Wu et al. 2004) is a widely used metric to quantify these effects. It is defined as the ratio of contrasts:

$$ASF(z) = \frac{I_{artifact}(z) - I_{bg}(z)}{I_{artifact}(z_0) - I_{bg}(z_0)}, \quad (2.95)$$

where $I_{artifact}$ and I_{bg} are the intensities of the artefact and background, respectively, while z_0 and z correspond to the in-focus and the off-focus planes, respectively.

A different definition of the ASF given by (Zhang et al. 2006) takes into account not only the contrast, but also the noise of the background. The ASF is then calculated as

the ratio between the $CNR(z)$ measured in the given (off-focus) plane and the $CNR(z_0)$ measured in the in-focus plane. In this study, the latter definition was adopted, and the $ASF_{PC}(z)$ for a phase contrast signal in the reconstructed images is defined as:

$$ASF_{PC}(z) = \frac{CNR_{PC}(z)}{CNR_{PC}(z_0)}. \quad (2.96)$$

Chapter 3

3 Detector performance evaluation

3.1 Introduction and chapter overview

Image quality is a product of many factors including beam characteristics, imaging geometry, source dimensions, patient movement, detector performance and image post processing. Both imaging techniques described previously, Phase Contrast Imaging and Digital Breast Tomosynthesis, impose several demands on the imaging system. Therefore it is highly important to choose the detector with the best optical and x-ray performance in terms of suitability for both imaging methods. The choice of the detector was made on the basis of a detailed comparison of the performance of 3 commercially available flat panel detectors: the Anrad SMAM (ANRAD Corporation, Montreal, Canada) a-Se flat panel, the Dexela (Dexela Ltd, London, UK) active pixel CMOS flat panel, and Hamamatsu C9732DK passive pixel flat panel (Hamamatsu Photonics, Japan), see Figure 3.1.

An overall imaging performance of an x-ray detector is given by its DQE (detective quantum efficiency) values at different frequencies in the image. DQE is a product of two components, namely image resolution and noise at a given radiation exposure. The resolution of the final image is described by the modulation transfer function (MTF). In mammography, the resolution can be affected by a number of factors such as the size and shape of the detector elements, focal spot size, the magnification and the spread of signal between detector pixels. The MTF provides information about the system spatial resolution and enables a fair comparison between different detectors. The metric used for the evaluation of noise is the noise power spectrum (NPS). It takes into account all the sources of noise in a mammographic image, i.e. quantum, fixed electronic, secondary signal and indirect secondary quanta. Quantum noise is an intrinsic source of noise in any x-ray detection system as it results from the random distribution of x-ray quanta. DQE, spatial resolution by means of the modulation transfer function (MTF) and noise characteristics described by the noise power spectrum (NPS) were obtained

for all three systems. Additionally, for the Dexela detector, the Photon Transfer Curve (PTC) measurements of the sensor were also performed, in order to find performance parameters such as conversion gain, read noise, full well capacity, dynamic range and dark current. This was impossible for the Anrad detector, which is a direct conversion system and therefore is not sensitive to visible light. In the case of the Hamamatsu detector, it was impossible to remove the scintillator bonded on top of the CMOS sensor. Finally, all three detectors were characterized in terms of the amount of the signal that is detected in detector pixels surrounding the one which is actually illuminated by x-ray. This “signal spill-out” is in fact an undesired effect in CAXPC imaging, as it decreases the detectable PC signal.

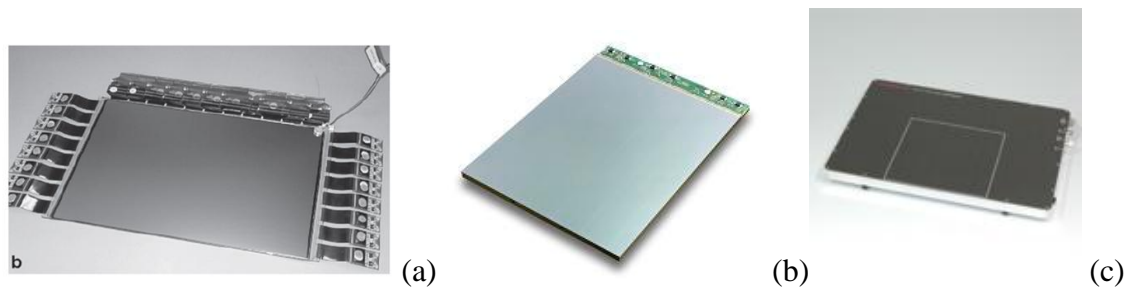


Figure 3.1 Flat panel detectors under investigation: Anrad SMAM (a), Dexela (b) and Hamamatsu (c)

3.2 Flat panel detectors under investigation

3.2.1 Anrad SMAM

The Anrad SMAM uses a thin layer of amorphous selenium as the x-ray absorber. It is a direct conversion detector, which means that x-rays are directly converted into charge within the photoconductive material (a-Se). As it happens for all photoconductors, following excitation caused by radiation, electrons are freed from the valence band. The liberated electrons leave an equivalent number of holes in the valence band. The electron-hole pairs form the detectable signal. In order to move the charge towards the charge collection electrodes (see Figure 3.2), an electric field is applied between electrodes deposited on the upper and lower surfaces of the photoconductor. The top electrode is continuous, while the bottom electrode is often a glass substrate with a matrix of detector elements, “dels” (Yorker et al. 2002). Each del stores the charge until it is activated by the neighbouring TFT (Thin Film Transistor) switch. The signal from

all dels is moved along the readout lines, then amplified and digitized. The Anrad detector features $85\mu\text{m}$ dels and is used in the Giotto, Planmed and Siemens commercial mammography systems. The active area of SMAM is 2032×2817 pixels, which corresponds to an area of $17.3 \times 24 \text{ cm}^2$. The maximum frame rate of the detector is 0.7fps.

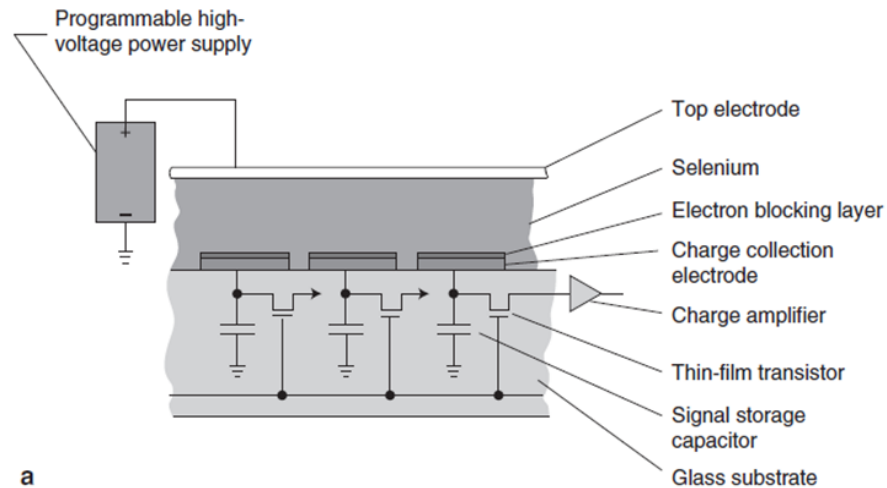


Figure 3.2 Selenium system schematic of direct conversion detector. Figure adopted from (Pisano and Yaffe 2005)

3.2.2 Dexela

The Dexela flat panel CMOS x-ray detector is an Active Pixel Sensor (APS) device. Each detector pixel contains 3 transistors (reset, source follower and row select), and a pinned photodiode to increase the photo-responsivity (and thus the quantum efficiency) and decrease dark current and read noise (Fossum 1997; El Gamal and Eltoukhy 2005), see Figure 3.3.

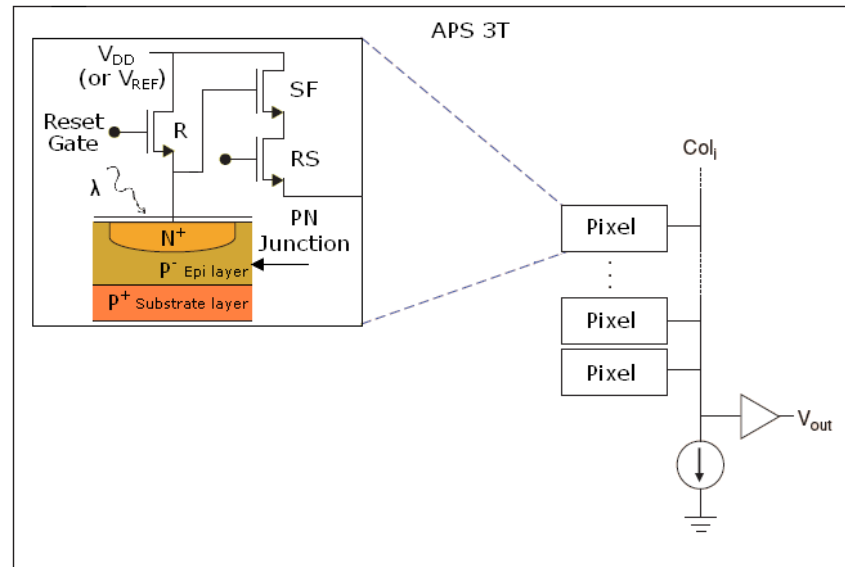


Figure 3.3 Dexela detector (right) and a pixel architecture of a 3T APS, R, SF and RS denotes the reset, source follower and row select transistors, respectively. Figure adopted from (El Gamal and Eltoukhy 2005).

The full well capacity of the pixels can be switched between two separate modes: high full well (HFW) and low full well (LFW). The LFW mode allows a low noise during binned mode read-out, and increased sensitivity of the detector at low exposure levels. In the HFW mode the sensitivity is lower, but the exposure range is extended. As an x-ray convertor in the mammographic energy range, it uses a thin layer (150 μm) of scintillator (Thallium-activated Caesium Iodide (CsI:Tl)). The active area of a single module for this detector is 1944 x 1536 pixels, i.e. 11.5 x 14.5 cm^2 , and the pixel pitch equals 75 μm . Up to 6 separate modules can be tiled to form a larger detector area, depending on the specific application. The largest active area that is currently available is 29 x 23 cm^2 . The detector can be operated in the binned mode, which allows a trade-off between spatial and temporal resolution. In the full resolution mode (75 μm pixels), a frame rate of 26 fps is achieved, while for the 4x4 binning resolution mode (300 μm pixels) a maximum rate of 86 fps is reached. The pixel fill factor for this detector is 84%.

3.2.3 Hamamatsu

The Hamamatsu C9732DK is an indirect conversion Passive Pixel Sensor (PPS) CMOS detector. As an x-ray convertor it uses a 160 μm layer of CsI:Tl. The 50 μm pixels create an array with dimensions of 2400 by 2400 pixels. The active area of the detector is 12 x

12 cm². The detector dynamic range is 74dB, with a read noise of 1250 e⁻ and saturation charge of 6.4 x 10⁶ e⁻. The maximum frame rate is 1 fps. The pixel fill factor is 79%.

3.2.4 Direct and indirect conversion

Both the Hamamatsu and the Dexela detector are indirect conversion detectors. Unlike direct conversion systems, they involve an extra step in the conversion of x-ray photons into electric charge (see Figure 3.4), provided by a scintillator. Incoming x-ray photons are first converted into visible light photons within the scintillator material. One of the most common scintillators is thallium-activated caesium iodide phosphor, CsI(Tl), used in both the Dexela and Hamamatsu detectors. The created visible light photons are then converted into charge by photodiodes in the CMOS. In the Hamamatsu detector, the scintillator is directly deposited onto the CMOS matrix, and therefore no fibre optics plate (FOP) is present.

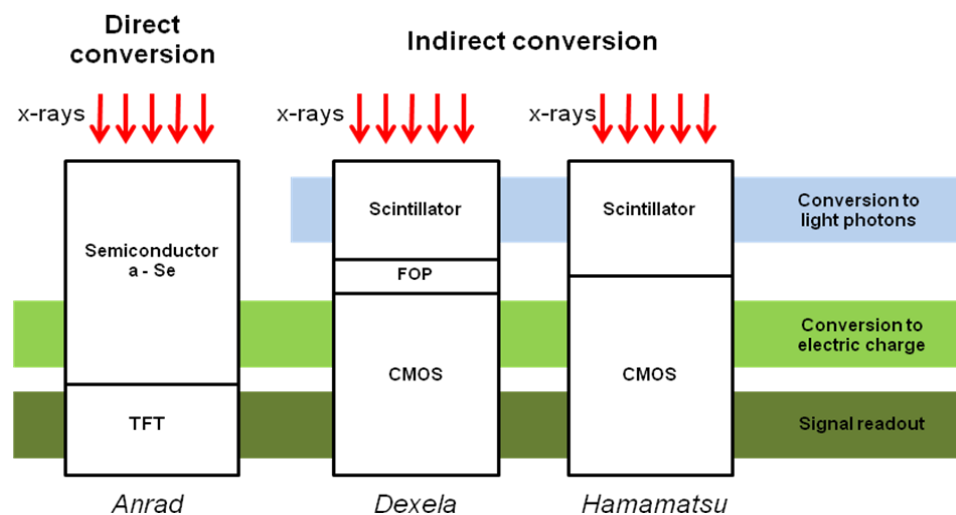


Figure 3.4 Schematic of conversion of x-ray photons into an electric charge in direct conversion systems (Anrad detector) and indirect conversion systems (Dexela and Hamamatsu). Figure adopted from (Chotas et al. 1999), modified.

3.3 Optical characterization

3.3.1 Photon Transfer Curve

The Photon Transfer Curve is a comprehensive characterisation method of the optical properties of an imaging sensor. The basic principle of this method involves the assumption that the sensor itself is a “system block” with light photons as input and

digital data as output. As the light radiation follows the Poisson distribution, it is straightforward to predict the inherent noise at a given illumination level. Therefore, any additional noise seen on the output of the system originates from the system itself. Figure 3.5 shows a typical PTC profile represented on a log-log graph by the square root of the mean number of photons (r.m.s) incident on a given pixel as a function of the illumination level. The measurement of the PTC is usually performed with a monochromatic light source such as a light-emitting diode (LED). The illumination level is varied from complete darkness to full well illumination. The PTC contains 3 sources of noise: read noise, shot noise and fixed pattern noise. The read noise is random noise which originates from the sensor electronics. It is measured in total darkness and is often called the “noise floor” of the system. The second region of the PTC curve corresponds to the shot noise. The shot noise is the noise associated with the Poisson distribution of the light photons, and is directly proportional to the square root of the signal. This type of noise does not depend on the used sensor. Fixed pattern noise dominates at relatively high levels of illumination. It originates from the differences in the sensitivity and photoresponse between pixels.

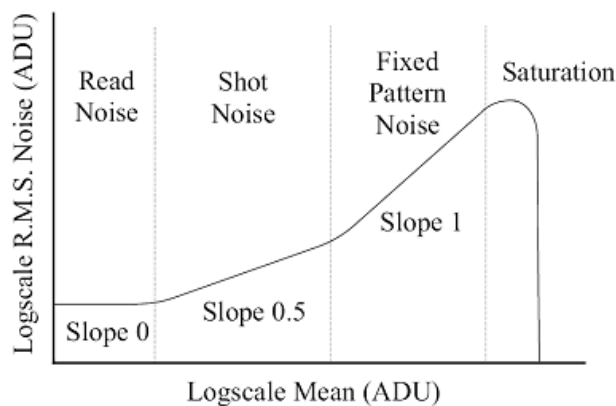


Figure 3.5 Ideal PTC with four classical noise regimes. Figure adopted from (Janesick 2007), modified.

In practice only the shot and read noise are used to characterize the sensor. The fixed pattern noise is removed by subtracting two consecutive frames. This step is part of the shot noise calculation, which is given by the statistical variance of the random noise in the image (Bohndiek et al. 2008; Bohndiek et al. 2008):

$$\sigma_s^2 = \frac{1}{2(N-1)} \sum_{l,m} \left[(S_{l,m}^A - \overline{S_A}) - (S_{l,m}^B - \overline{S_B}) \right]^2 \quad (3.1)$$

where $S_{l,m}^A$ and $S_{l,m}^B$ are the individual pixel values of the first (A) and second (B) frame respectively, and $\overline{S_A}$ and $\overline{S_B}$ are the mean of all pixel values in the first and second frame, respectively. The factor of 2 in the denominator comes from the process of subtracting two frames, which doubles the noise.

From the PTC curve it is possible to extract a number of parameters which describe the overall performance of the sensor. Some of these parameters are described below.

Read noise

Read noise (σ_R) is the minimum detectable signal. It can be extracted directly from the PTC as the noise level at zero illumination.

Gain

The gain of the sensor (G) is usually expressed in digital numbers per signal electron (DN/e⁻). It is calculated by fitting the line to the variance curve in the shot noise regime of the PTC and measuring its slope.

Full well capacity

The full well capacity expressed in electrons, $FW(e^-)$, can be calculated by dividing the maximum signal S_{\max} by the sensor gain, G:

$$FW(e^-) = \frac{S_{\max}}{G} \quad (3.2)$$

Dynamic range

The dynamic range is defined as the ratio of the largest detected signal to the smallest detectable signal (or noise floor):

$$DR = 20 \log \left(\frac{FW(e^-)}{\sigma_R(e^-)} \right) \quad (3.3)$$

3.3.2 Experimental methods and results

The measurement of the PTC was obtained for the Dexela detector with a narrowband LED emitting at $530\pm 20\text{nm}$ (green). The illumination level was varied from complete darkness to full well illumination. Figure 3.6 shows the PTC curves for the HFW and LFW modes. The two curves on the plot correspond to mixed read and shot noise (diamonds), and to shot noise only (squares), respectively. The LFW mode features higher shot noise at the same signal level compared to HFW mode. The full well capacity of the photodiode is about 13100 DN for the HFW and 12000 DN for the LFW.

Table 3.1 provides the main detector parameters extracted from the PTC analysis for both, HFW and LFW modes. The conversion gain can be changed at the pixel level by switching between the two modes. In particular, for the LFW mode the gain is 3 times lower than for the HFW mode.

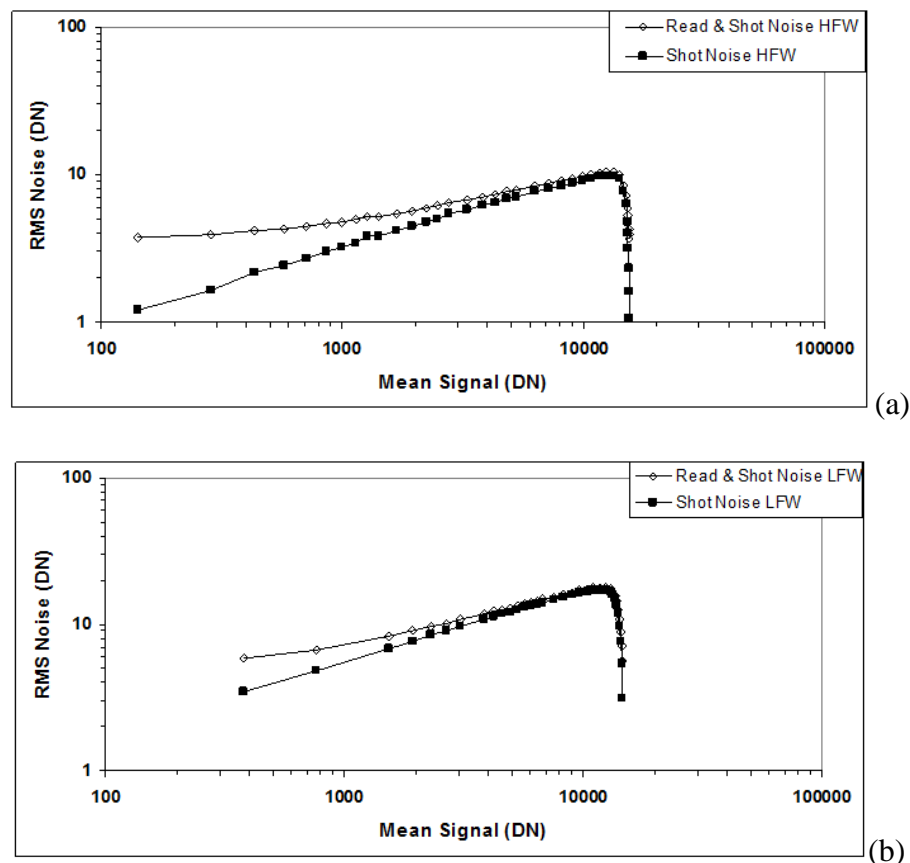


Figure 3.6 PTC curve for HFW (a) and LFW (b) for Dexela detector

The LFW mode enables imaging with low read noise at lower dynamic range (suitable for low exposure levels), while the HFW mode is more suitable for imaging at higher

dynamic range with reduced noise performance (suitable for higher exposure levels) (Naday et al. 2010).

Table 3.1 Summary of the performance parameters of the sensor

Parameter (full resolution)	HFW mode	LFW mode
Conversion Gain, e ⁻ /DN	101 ± 17	34 ± 3
Read Noise, e ⁻	355 ± 62	157 ± 13
Full Well capacity, e ⁻	(1.3 ± 0.2) × 10 ⁶	(4.2 ± 0.4) × 10 ⁵
Dynamic Range, dB	71 ± 4	68.5 ± 2

The conversion gain e⁻/DN is defined as the slope of the straight line fitting the PTC curve. A least squares method (often called a linear regression method) has been used for the fitting, where a smallest sum of square distances between the data points and the straight line is calculated. For a linear function y=ax+b, the slope a can be calculated according to the following formula:

$$a = \frac{n \sum x_i y_i - \sum x_i \sum y_i}{n \sum x_i^2 - (\sum x_i)^2} \quad (3.3)$$

where n is the number of points taken for fitting, x_i and y_i are the coordinates of the data points. We can estimate how well the fit reproduces the data by analyzing the so-called correlation coefficient, R^2 , which can be calculated as:

$$R^2 = \frac{n \sum x_i y_i - \sum x_i \sum y_i}{\sqrt{n \sum x_i^2 - (\sum x_i)^2} \sqrt{n \sum y_i^2 - (\sum y_i)^2}} \quad (3.4)$$

The value of R^2 is always between 0 and 1, with R=1 representing the ideal fit. The average value of R^2 in this study was equal 0.9946 for the line fit on the PTC curve.

The individual uncertainties of the slope of the fitted line can be calculated according to the following formula:

$$\Delta a = \sqrt{\frac{n \sum y_i^2 - a \sum x_i y_i - b \sum y_i}{n-2} \frac{1}{n \sum x_i^2 - (\sum x_i)^2}} \quad (3.5)$$

The uncertainty of the conversion gain ΔK can be calculated as:

$$\Delta K = \frac{\Delta a}{a} K \quad (3.6)$$

Similarly, the uncertainties of the read noise ΔR and full well capacity ΔFW depend on the read noise, and they are computed as follows:

$$\Delta R = \frac{\Delta K}{K} R \quad (3.7)$$

$$\Delta FW = \frac{\Delta K}{K} FW \quad (3.8)$$

The uncertainty of the dynamic range ΔDR depends on the uncertainties on both the read noise and the full well capacity. Therefore it can be calculated using the theory of error propagation as:

$$\Delta DR = \sqrt{\left(\frac{\Delta R}{R}\right)^2 + \left(\frac{\Delta FW}{FW}\right)^2} \quad (3.9)$$

3.4 X-ray characterization of the detectors

3.4.1 Modulation Transfer Function (MTF)

There are several ways to measure the spatial resolution of the system (i.e. the minimum distance between two objects at which they can still be distinguished as separate objects, expressed in line pairs/mm). A simple, “partial” measurement can be obtained with a bar pattern. For the full quantitative characterization of the system, a more sophisticated method is required, i.e. the assessment of the Modulation Transfer Function (MTF). The MTF describes how well the system transfers the signal of the x-rays incident on the detector surface to the digital signal given as output, as a function of the spatial frequency. The imaging system processes a sinusoidal signal from the input to its output. The signal at low spatial frequencies is transferred with little loss, so the ratio between output and input values is close to one. The higher the frequency of the incident signal, the lower its amplitude at the output of the system. The design of a state high resolution imaging detector aims at achieving the highest possible MTF at high frequency levels, as this enables the detection of very fine details in the sample.

Various methods to measure the MTF exist: the square wave method, the edge method, and the slit method (Beutel 2000). In this work, the edge method was adopted, and a detailed description will be given below.

The MTF was measured with an edge method (Samei and Flynn 2002) according to the IEC standard. The measurements were performed with a tungsten edge which was 1mm thick and highly polished to a very sharp edge. Figure 3.7 shows the order of the steps required to measure and calculate the MTF of a given system using this method.

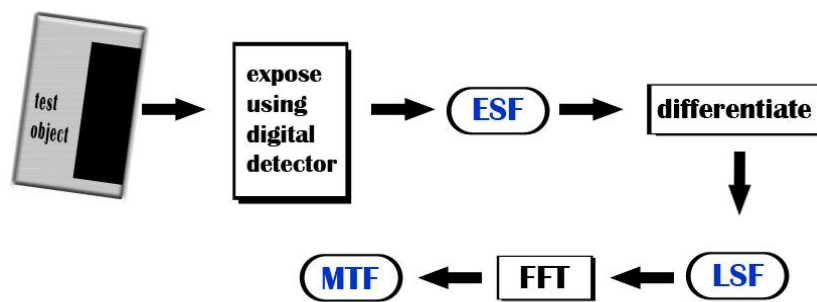


Figure 3.7 Schematic of the steps required to calculate the MTF of a system.

The edge was placed at a shallow angle (between 1.5° and 3°) with respect to the detector pixel rows or columns, which corresponds to measuring the MTF in the vertical and horizontal directions, respectively. The angle was estimated using a linear regression technique (Greer and van Doorn 2000; Price et al. 2008). Every image was gain and offset corrected before the MTF analysis. In order to calculate the edge spread function (ESF), seven edge response curves were extracted from the edge image. One of the edge profiles was selected as the reference one, and the remaining six were shifted laterally until they all overlapped on the reference edge profile. (IEC 2003; IEC 2007). The resulting averaged ESF was then differentiated to produce a line spread function (LSF).

The MTF was calculated as the modulus of the fast Fourier transform (FFT) of the LSF. The MTF was normalized to one at zero frequency. In order to avoid aliasing effects, the MTF was calculated only up to the Nyquist frequency (F_{Nyq}). The curve obtained in this way is often called presampled MTF (pMTF). According to the IEC standard, the horizontal and vertical pMTFs were calculated by binning the data points in frequency intervals f_{int} ($f - f_{int} \leq f \leq f + f_{int}$) around the spatial frequencies from 0.5 to F_{Nyq} , with an

interval of 0.5 lp/mm. f_{int} is obtained as $0.01/\Delta x(\text{mm})$. The final pMTF values were calculated as the average of the horizontal and vertical pMTFs. In order to remove low frequency (background) trends arising from the x-ray field's non-uniformity (e.g. heel effect, etc) that could increase the MTF at low frequencies (IEC 2003; IEC 2007), a second order polynomial fit correction was applied to the images of the edge.

All MTF curves were calculated from edge images acquired at approximately half saturation levels. The pMTF reaches 50% at 5.4 lp/mm, 3.4 lp/mm and 3.3 lp/mm for Anrad, Dexela and Hamamatsu detectors, respectively (see Figure 3.8). These values are in a good agreement with the results of the MTF measurements on similar systems previously reported in the literature (Blake et al. 2006; Honey et al. 2006; Lazzari et al. 2007; Zhao and Zhao 2008; Rivetti et al. 2009) (see Table 3.3). The limiting frequencies were different for the three systems. The highest cut-off frequency was observed for Hamamatsu, and it was of 10lp/mm. Beyond the cut-off frequencies (Nyquist frequencies), an amount of high-frequency signal may be aliased by the detector (Monnin et al. 2007). This aliasing can be reduced in case of indirect system by using thicker scintillators, however this also leads to a decreased resolution of the detector.

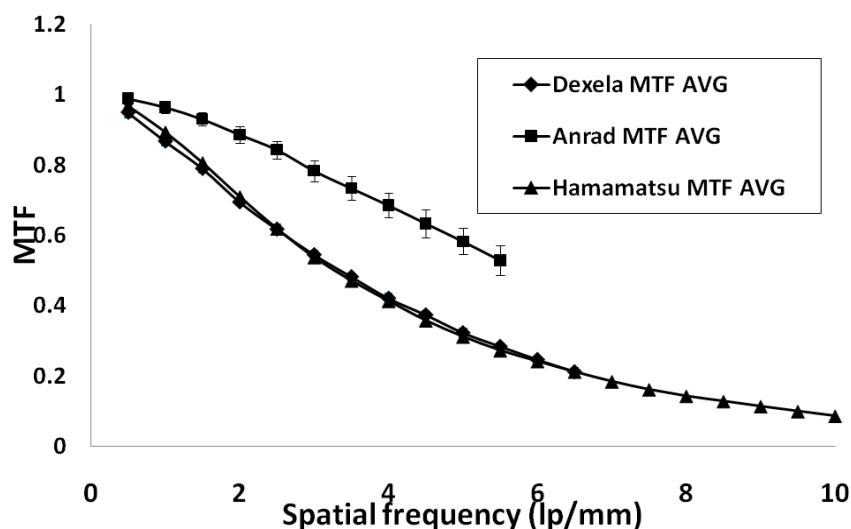


Figure 3.8 MTF obtained at 28kV for Dexela (blue line), Anrad (red line) and Hamamatsu (green line) detectors.

The MTFs measured for the three systems examined indicated that the MTF was notably higher for the direct conversion detector. This can be explained by the fact that the charge is collected with little lateral spread in direct detection systems, and thus good resolution is expected relative to the indirect detection systems, where light scattering in the scintillator is the main cause of blur: light photons are scattered in the

scintillator layer, thus widening the LSF and blurring the image. In direct conversion detectors there is no scintillator, and the x-ray photons are directly converted into electric charge. The LSF is narrower in this case, resulting in a limited signal spread across neighbouring pixels.

3.4.2 Noise Power Spectrum (NPS)

The Noise Power Spectrum can be described as the variance of the image intensity (i.e. image noise) as a function of the spatial frequency in the image. Similarly to MTF curves, a logarithmic increase of the spatial frequency results in decreasing the signal amplitude. In this chapter, a detailed description of the NPS measurements and calculations will be presented.

Figure 3.9 shows the series of steps needed to evaluate the NPS of a system. In order to calculate the NPS a number of flat field images were acquired. First, the gain and offset corrections were applied to all images to minimise the gain nonuniformities between pixels known as fixed pattern noise (FPN), and to remove the dark offset from the images. As previously reported (Moy and Bosset 1999), 10 dark and 10 flat field images are considered sufficient to minimize the noise added during gain and offset corrections.

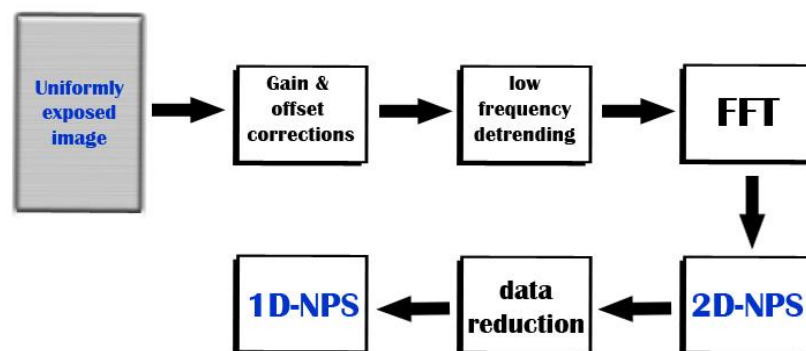


Figure 3.9 Schematic of the steps required to calculate the NPS of a system.

The second step of the NPS calculations was to extract overlapping regions of interest (ROI) of 256×256 pixels from a central area of the image. According to the IEC standard, in order to achieve required 5 % accuracy of the two-dimensional NPS, at least four million independent image pixels should be included in the analysis (IEC 2003; IEC 2007). Therefore it was important to acquire a sufficient number of flat

fields. The next step involved correcting images for the presence of background trends (such as the heel effect), by fitting a second order polynomial and subtracting the fitted two-dimensional function $S(x, y)$ from the flat field image $I(x, y)$. Next, the two-dimensional NPS was obtained according to the following equation:

$$NPS(u, v) = \frac{\Delta x \cdot \Delta y}{M \cdot N_x \cdot N_y} \sum_{m=1}^M |FFT\{I(x_i, y_i) - S(x_i, y_i)\}|^2 \quad (3.4)$$

where u and v are the spatial frequencies corresponding to x and y , Δx and Δy are the x and y pixel pitches, N_x and N_y are the ROI dimensions in pixels in the x and y directions (both equal to 256 as recommended by the IEC standard), M is the number of ROIs used, and FFT denotes the fast Fourier transform operation.

Finally, in order to calculate the one dimensional NPS, seven rows or columns (depending on the considered direction) on both sides of the central axis were averaged. This number of rows and columns was chosen in order to reduce the statistical noise. The central axis itself was not taken into account, as it can be easily influenced by column- or row-wise FPN of the flat field images. Each data point was associated to a specific spatial frequency according to the formula $f = \sqrt{u^2 + v^2}$. Then, in order to smooth the NPS, an averaging of the data points within the 14 rows and columns that fall in a frequency interval of f_{int} around the spatial frequencies from 0.5 to F_{Nyq} with an interval of 0.5 lp/mm (see above) was performed (IEC 2003; IEC 2007).

The horizontal and vertical $NPS(f)$ were then divided by the (large area signal)² to obtain the normalized NPS (NNPS), expressed in terms of relative input exposure fluctuation (Dainty 1976; Beutel 2000). The term “large area signal” corresponds to the mean DN in the image for each particular dose, and can be obtained from the signal transfer property (STP) curve. Finally, the horizontal and vertical 1D NNPS were combined to calculate the average 1D NNPS.

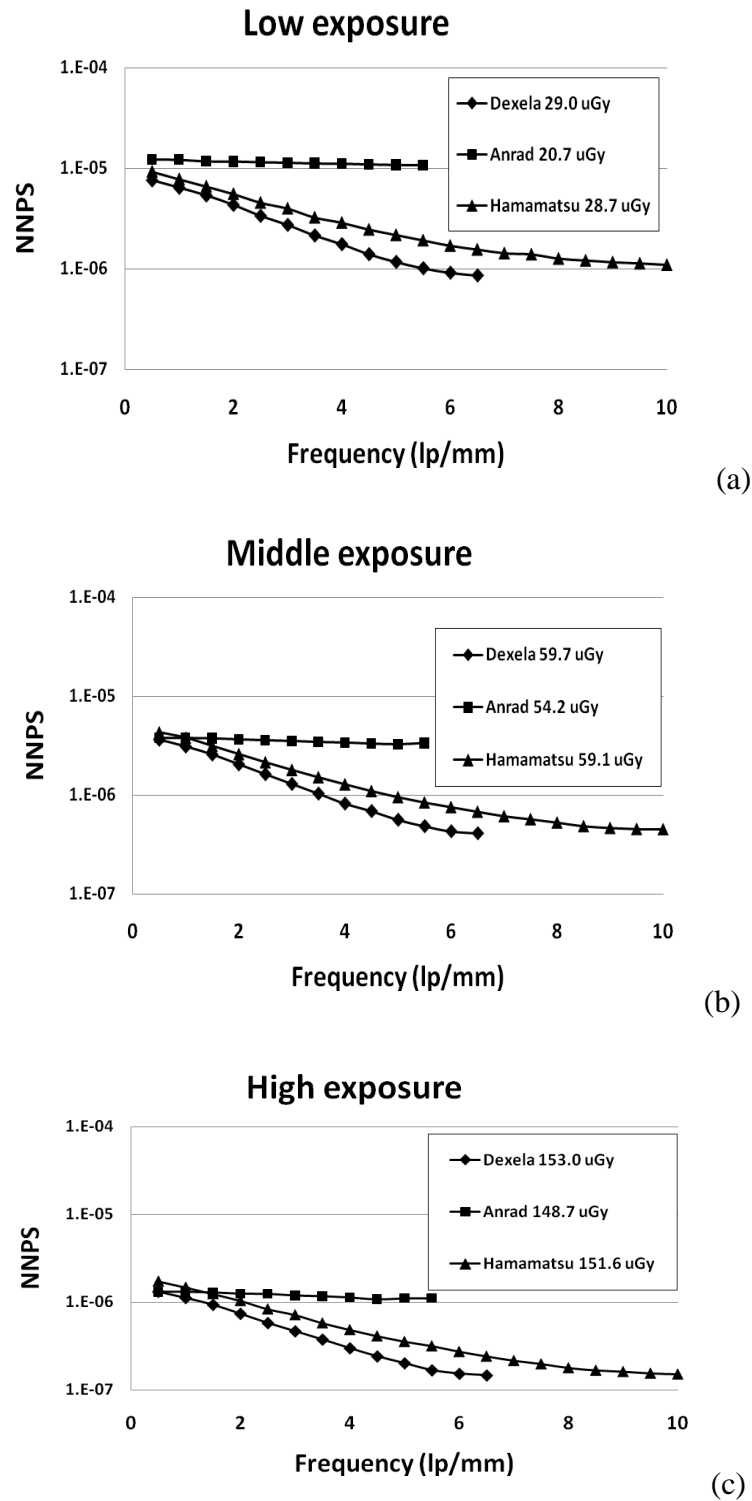


Figure 3.10 NPS for Dexela (diamonds), Anrad(squares) and Hamamatsu (triangles) detectors obtained at low (a), middle (b) and high (c) exposures used in mammography.

The 1D NNPS is required by the DQE calculation and gives information about the noise response of the detector. Figure 3.10 shows the NNPS curves at 28 kV at low, middle and high exposure levels for all three detectors tested. For the Dexela detector, only the NNPS corresponding to the HFW mode is shown. NNPS indicates the power of the noise at each frequency in the image. Generally, the lower the value of NNPS at a given frequency the less noise is present in the image. The noise becomes smaller for higher exposures (see the difference between Figure 3.10a and c). TS imaging is usually performed at low exposures so that the total exposure from several acquired projections is similar or lower than that used in 2D conventional mammography. The results show that for the low exposure (see Figure 3.10a) the values of the NNPS for the Anrad detector are almost constant with frequencies. This is due to the process of adding of the noise above the Nyquist frequency with that at lower frequencies taking place in the direct conversion detectors (Konstantinidis, 2011). In the other two indirect conversion systems this effect is prevented by the scintillator which acts as a filter for high frequencies. This is why the noise is smaller at higher frequencies for both the Dexela and the Hamamatsu detectors. The NNPS curves lie beneath these of the other two systems. It can be also seen (in Figure 3.10) that the NNPS values decrease with increasing exposure (K_a) more rapidly in indirect conversion systems, and remain almost exposure independent for direct conversion detector. The NNPS results influence the DQE curves, and thus an increase of the DQE is observed with increasing exposure. As specified in the IEC standard, since the 1D NNPS were calculated from more than four million independent pixels, an accuracy of at least 5 % is obtained.

3.4.3 Detective Quantum Efficiency (DQE)

The DQE is an effective and widely used metric of the performance of an imaging system. It enables a reliable comparison between the imaging capabilities of different systems. The DQE is usually defined by the ratio of the squared output signal to noise ratio (SNR_{output}^2) and the squared input signal to noise ratio (SNR_{input}^2):

$$DQE(f) = \frac{SNR_{out}^2}{SNR_{in}^2} \quad (3.5)$$

where f denotes the spatial frequency at which the detector capabilities are tested.

Ideally, the DQE would equal one at all spatial frequencies. In practice, it decreases with increasing spatial frequencies due to the combined effect of spatial resolution decrease and noise transfer decrease with increasing spatial frequency (Williams et al. 2007). Thus, in order to calculate the DQE values for a given system, one needs to take into account both, the MTF and the NPS of the system.

The DQE was calculated from the following formula (Beutel 2000; IEC 2003; IEC 2007):

$$DQE(f) = \frac{SNR_{out}^2}{SNR_{in}^2} = \frac{MTF^2(f)}{\frac{F}{K_a} \cdot K_a \cdot NNPS(f)} \quad (3.6)$$

where the F/K_a is the fluence per exposure ratio, which can be calculated as (Johns 1983; Boone 1998; Beutel 2000; Samei and Flynn 2002):

$$\frac{F}{K_a} = \int_0^{kV} \Phi_{norm}(E) \cdot \frac{W \cdot Q}{\left(\frac{\mu_{en}(E)}{\rho}\right)_{air} \cdot E \cdot e \cdot 10^8} dE \quad (3.7)$$

In the above equation, $\Phi_{norm}(E)$ is the normalized spectrum, W is the work function of air (33.97 keV), Q is the charge liberated in air by one R (2.58×10^{-4} Cb/kg/R) and e is the electronic charge (1.6022×10^{-19} Cb).

The product $\frac{F}{K_a} \cdot K_a$ corresponds to the SNR_{in}^2 due to the Poisson distribution of the input quanta. The SNR_{out}^2 output is calculated from the ratio between MTF^2 and NNPS.

Beam quality

In x-ray imaging, the beam quality refers to parameters of the beam such as its average energy and corresponding half value layer (HVL). For the x-ray characterization of the detectors, a Tungsten anode x-ray tube was used. According to the IEC standard, a beam quality of 28kV was chosen from several beam qualities recommended for DQE testing in the mammographic energy range. The choice of the beam quality was made on the basis of the target material of the x-ray tube (tungsten, W) and the availability of the attenuation filters (aluminium, Al). The tube voltage was varied near the nominal value of 28kV to reach the half value layer (HVL) of 0.83 mm of Al required by the

IEC standard. In this way, the right HVL was reached with 3% accuracy. For the HVL measurements, thin Al foils (99% purity) of various thicknesses were used. The measurements were done using a calibrated ionization chamber (KEITHLEY 35050A Dosimeter). The inherent filtration of the x-ray tube was estimated using the Total Filtration Calculator (Reilly 1999) to be 1.4 mm Al. This software calculates the total filtration of the x-ray system given information about the anode, kVp, measured HVL and the measurement distance. This value is estimated as the actual inherent filtration of a particular x-ray tube varies depending on the design. The IEC standard recommends a total thickness of 2.5mm of Al, normally consisting of 0.5mm from the inherent filtration, and an additional 2mm of Al to simulate the breast. Therefore in this case an additional thickness of 1.1mm of Al (99.999% purity) was added to match the total thickness required by the IEC standard.

Table 3.2 Values related to the used beam qualities

Parameter	IEC required	Measured	Estimated
Tube voltage, kV	28	28	-
Total filtration (inherent + added), mm Al	0.5 + 2.0	-	1.4 + 1.1
HVL, mm Al	0.83	0.83	-
IEC F/K_a , x-rays/ μ Gy/ mm^2	6575	-	7009

In order to estimate the fluence per exposure ratio (F/K_a) (or ideal SNR^2 input per K_a), the spectrum simulator software *Spektr* (Johns 1983) was used. *Spektr* is a MATLAB based graphical user interface (GUI) (Siewerdsen et al. 2004), which employs the TASMIP algorithm of Boone and Seibert (Boone and Seibert 1997). It simulates a spectrum given kV/HVL combination used in the experiments. It is based on the algorithm published by Boone and Seibert (1997). A tungsten anode x-ray tube and the voltage of 28kV were used for the evaluation of the detectors. The half value layer (HVL) of 0.83 mm of Al is required by the IEC standard for the mammography beam quality. These settings were used as the input data for *Spektr* resulting in 7009 x-rays per μ Gy per unit area. Table 3.2 shows the required, measured and estimated values of the beam used in the experiments.

DQE results

Figure 3.11 shows the comparison of the DQE values as a function of spatial frequency for the 3 systems at low (20.7 – 29.0 μGy), middle (54.2 – 59.1 μGy) and high (148.7 – 153.0 μGy) mammographic exposures. There were no significant differences between the DQE values along the horizontal and vertical axis of the detectors. The similar shape of the DQEs at all exposure levels tested indicates that the frequency composition of the DQE does not depend on the exposure (Monnin et al. 2007). DQE(0.5) values range between 0.56 and 0.72 at 20.7 μGy and 172.8 μGy for the Anrad detector, 0.55 and 0.66 at 7.1 μGy and 277.8 μGy for the Dexela detector (HFW) and 0.5 and 0.52 at 28.7 μGy and 244.4 μGy for the Hamamatsu detector. These results together with the high values of the NNPS suggest that the Dexela detector presents best overall imaging performance and would therefore be the best choice. However, the CAXPCi technique is based on the edge illumination method, which means that small deviations of the x-ray photons lead to a phase contrast signal. Therefore it is very important that each x-ray photon is registered by only one detector pixel. Otherwise, if the signal is spread out between the neighbouring pixels (i.e. if there is some spill-out between the pixels), the difference between the peaks is smaller as is the image contrast (see Chapter 3.5 for more details). The Anrad detector is a direct conversion system in which there is very little signal spill-out compared to indirect conversion detectors, like Dexela and Hamamatsu. Therefore, overall it was essential to choose a detector with high MTF and reasonably good overall DQE performance, which would perform better for the used CAXPCi technique.

Breast Tomosynthesis requires approximately 25 views to produce a sufficient quality image. Therefore, the average detector K_a per view should be of the order of 5 μGy . The Dexela detector features high DQE values at low exposure levels, i.e. 0.55 for HFW and 0.57 LFW at 7.1 μGy (Konstantinidis et al. 2012). Unlike its larger version Anrad LMAM that is typically used in tomosynthesis systems, the Anrad SMAM is designed for projection mammography. This means that the lowest integration time that can be achieved with this unit is 3s. Therefore it is not possible to evaluate its DQE performance at the very low air kerma levels used in Tomosynthesis.

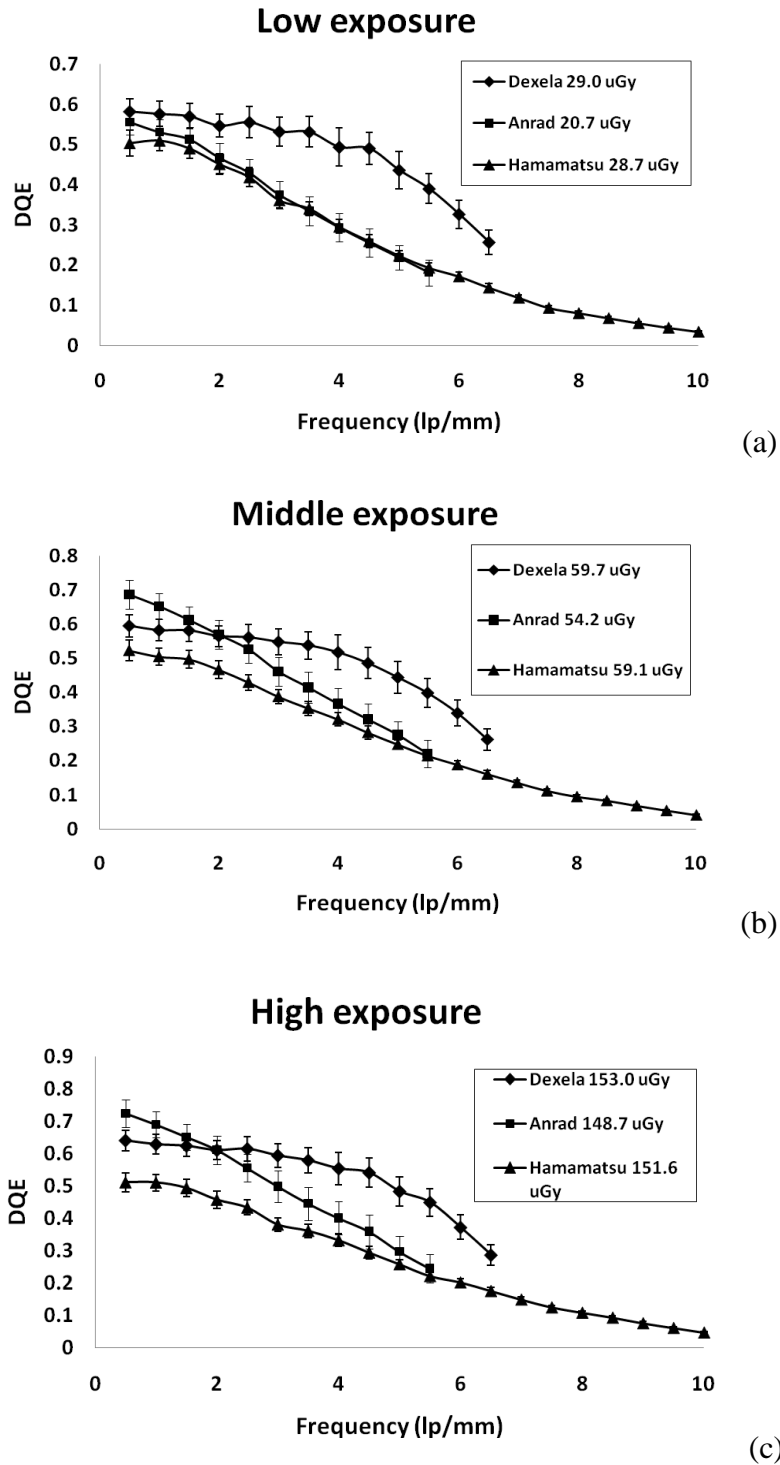


Figure 3.11 DQE curves for Dexela (diamonds), Anrad (squares) and Hamamatsu (triangles) detectors obtained at low (a), middle (b) and high (c) exposures used in mammography.

For comparison, the main parameters for other flat panel detectors used in mammography are reported in Table 3.3 (Blake et al. 2006; Honey et al. 2006; Lazzari et al. 2007; Zhao and Zhao 2008; Rivetti et al. 2009). It is difficult to compare different systems properly as they are usually evaluated under slightly different conditions, including the beam quality (anode/filtration combination and energy used), type and thickness of the detector material (scintillator or semiconductor), and data processing. Therefore the table only shows results from systems which were tested using the W/Al or W/Rh combinations at 28 kV. However, two exceptions were made for the GE Senographe 200D and the Hologic Lorad Selenia systems (Mo/Mo at 28 kV), which are broadly used in mammography. To the best of our knowledge, no one has characterized these detectors using W/Al or W/Rh combination for mammographic conditions yet. Table 3.3 shows how the imaging performance of the three detectors tested in this work compares with the imaging performance of other systems available on the market. It is immediately obvious from Table 3.3 that the spatial resolution of the Anrad detector is superior compared to most other systems, while the Dexela and Hamamatsu detectors have lower spatial resolution than other systems under investigation, which can limit the detectability of fine details such as microcalcifications. The visibility limit of microcalcifications for digital mammographic systems is considered to be 130 μm (Bick and Diekmann 2010). The peak DQE value at an exposure close to 130 μGy for the Anrad detector is higher than that measured with the Senographe 200D (GE) or the Senoscan (Fischer) systems. The peak DQE for the Dexela detector is higher than that of these two systems already at a smaller exposure of 122 μGy , and is therefore expected to outperform them even more at higher exposures. The Hamamatsu detector presents average peak DQE values comparable to other systems. Table 3.3 shows that the three detectors chosen for the comparison present a good cross-section among commercial detectors available the off-the-shelf in terms of imaging performance.

Table 3.3 Comparison of physical parameters of different mammographic systems

System	Data source	Detector technology	Scintillator/ semiconductor material	Radiation quality	MTF (at 50%) (x,y direction)	DQE peak (x,y direction) at average exposure level	K_{α}
Sectra Ltd <i>Sectra</i> <i>MicroDose</i>	(Honey et al. 2006)	direct photon counting	Crystalline silicon wafer	W/Al (28kV)	6.2, 3.3	0.63, 0.61	113 μ Gy
Fischer <i>Senoscan</i>	(Lazzari et al. 2007)	CCD	CsI+CCD	W/Al (28kV)	5.5	0.24	131 μ Gy
FUJIFILM <i>AMULET</i>	(Rivetti et al. 2009)	direct flat panel	aSe	W/Rh (28kV)	4.4	0.75	103 μ Gy
Siemens <i>Mammomat</i> <i>Novation</i>	(Zhao and Zhao 2008)	direct flat panel	aSe	W/Rh (28kV)	5.4	0.55	2.05 mR
General Electric <i>Senographe</i> <i>2000D</i>	(Lazzari et al. 2007)	indirect flat panel	CsI:Tl	Mo/Mo (28kV)	4	0.53	131 μ Gy
Hologic <i>Lorad Selenia</i>	(Blake et al. 2006)	direct flat panel	aSe	Mo/Mo (28kV)	5.8	0.59	92.5 μ Gy
Anrad <i>SMAM</i>	current study	direct flat panel	aSe	W/Rh (28kV)	5.4	0.72	130 μ Gy
Dexela <i>2923</i>	current study	CMOS APS	150um CsI	W/Rh (28kV)	3.4	0.61 (HFW)	122 μ Gy
Hamamatsu <i>C9732DK</i>	current study	CMOS PPS	CsI	W/Rh (28kV)	3.3	0.54	120 μ Gy

3.5 Influence of the signal spill out on the phase contrast signal

The signal spill-out refers to the amount of the signal detected by the neighbours of a given detector pixel when only the latter is illuminated. It has been shown to be one of the possible factors affecting the signal in the CAXPCi method (Olivo and Speller 2007). Similarly to MTF measurements, signal spill-out measurements were done using a sharp tungsten edge. The edge was placed at a small angle (between 1.5° and 3°) with respect to the detector pixel rows or columns to measure spill-out in the vertical or the horizontal direction, respectively. Data processing was carried out using the same calculation technique used for MTF measurements, starting from the ESF and leading to the evaluation of the LSF (see Figure 3.12). These steps are also a part of the MTF evaluation described already in Chapter 3.4.1. The LSF is used here to estimate the amount of the signal spill-out which has a major impact on the phase contrast signal in the CAXPCi method. The LSF curves were then normalized to the signal value at half FWHM for both the horizontal and the vertical cases.

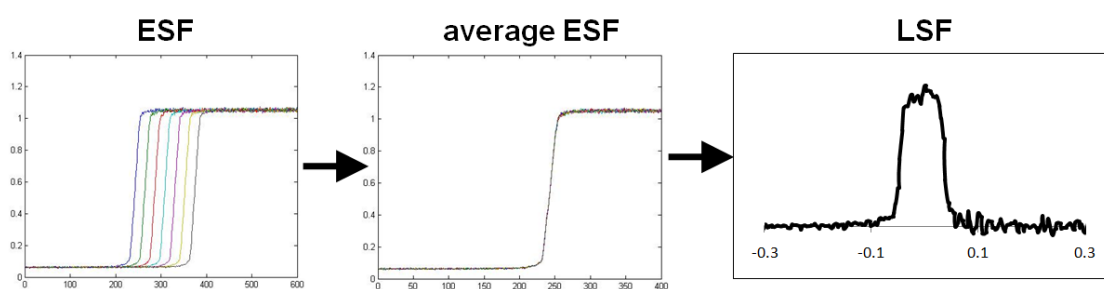


Figure 3.12 Steps required to obtain the LSF.

An essential step in obtaining the final shape of the LSF was to find a proper filtering technique which would efficiently remove the noise without affecting the curve shape. Several filtering methods were tested, including convolution with different kernels, smoothing of the ESF before differentiating it to obtain the LSF, and median filters with different kernels. The figure below shows the effect of several filtering on the horizontal LSF (black line) of the Anrad detector. The median filter with kernel 15 was eventually chosen visually and applied to all the LSFs of the 3 evaluated systems (see Figure 3.14). The median filter is widely used for smoothing the LSF in the MTF measurements, as it reduces high frequency noise without introducing significant bias into the MTF result (Marshall 2006).

In an ideal detector, the LSF would be a box function with dimensions corresponding to the pixel dimensions. In practice, however, this is never the case, and one observes a profile with a FWHM wider than pixel size. The amount of signal spill-out into adjacent pixels (first neighbours) can be estimated by integrating the LSF between the values on the x-axis which correspond to the physical dimensions of the first neighbour pixels. For example, considering the Dexela detector which has a pixel size of $75\ \mu\text{m}$, the main pixel corresponds to a range between $-37.5\ \mu\text{m}$ and $37.5\ \mu\text{m}$, while the first neighbour corresponds to the range between $37.5\ \mu\text{m}$ and $112.5\ \mu\text{m}$ (see Figure 3.15). The integrated signal was then normalized to the integral of the LSF over the main pixel, considered to receive 100% of the signal. The signal spill-out was calculated for adjacent pixels on both sides, and the final value was obtained as their average.

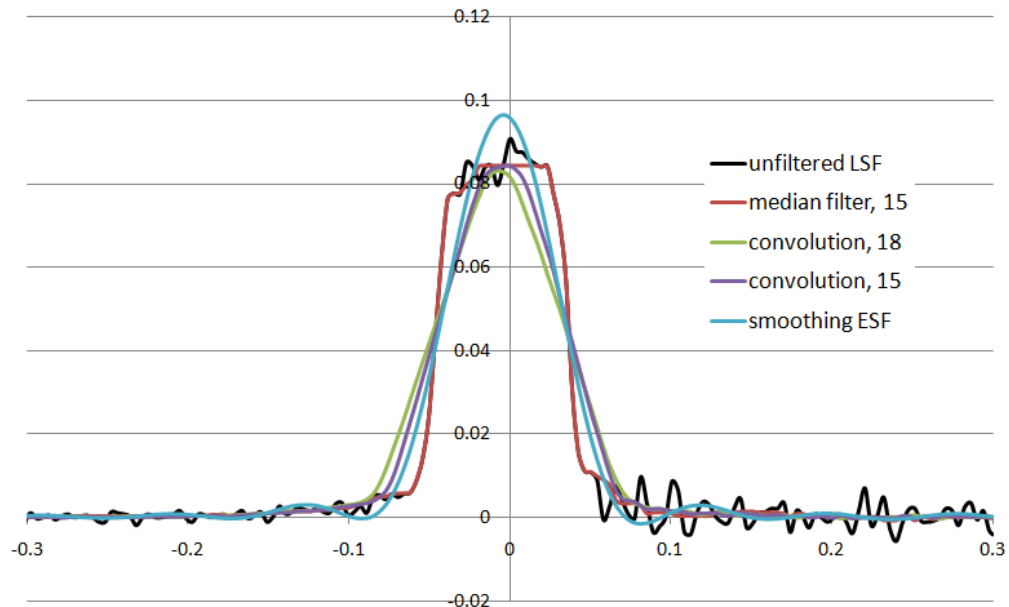


Figure 3.13 Effect of selected filters on the LSF curve (black line) and LSF obtained by smoothing the ESF prior to differentiation to the LSF (blue line).

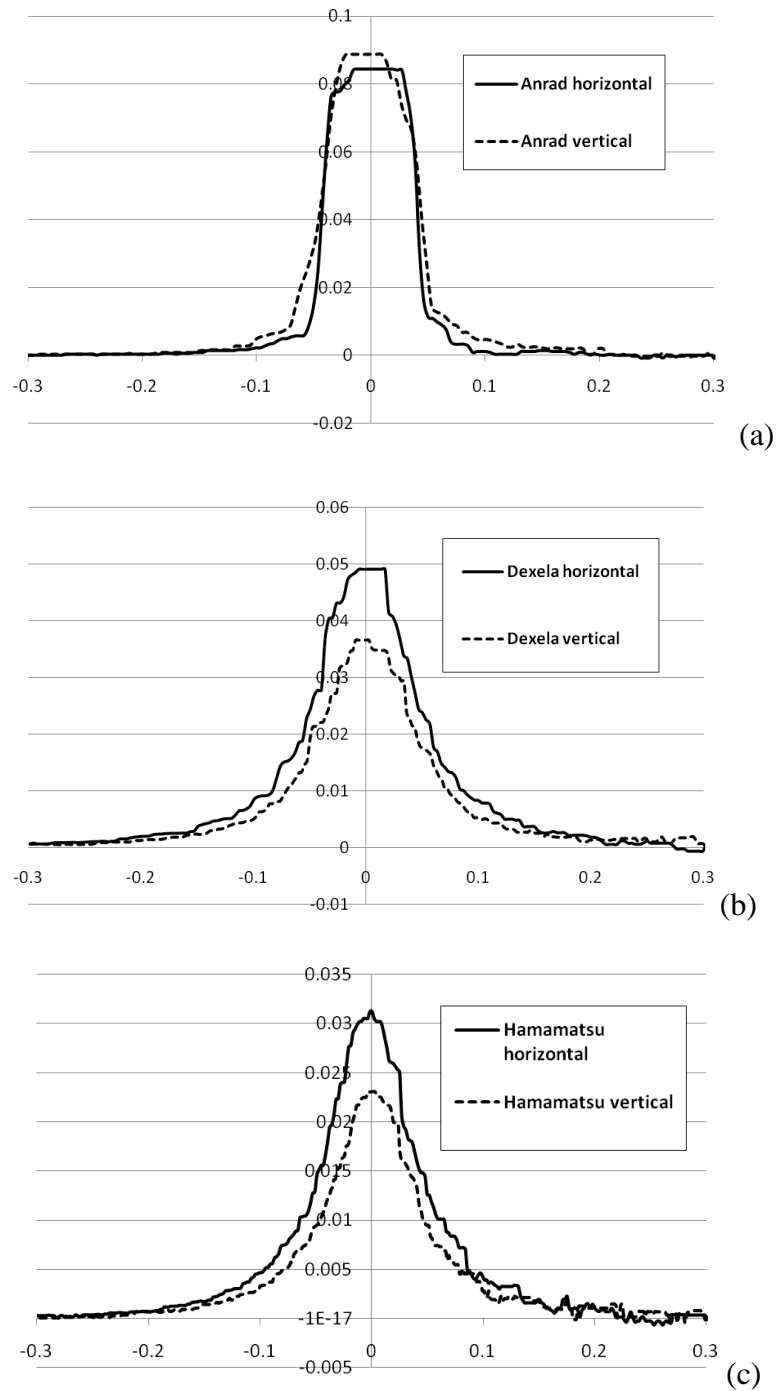


Figure 3.14 Filtered LSFs of three detectors tested: Anrad (a), Dexela (b) and Hamamatsu (c).

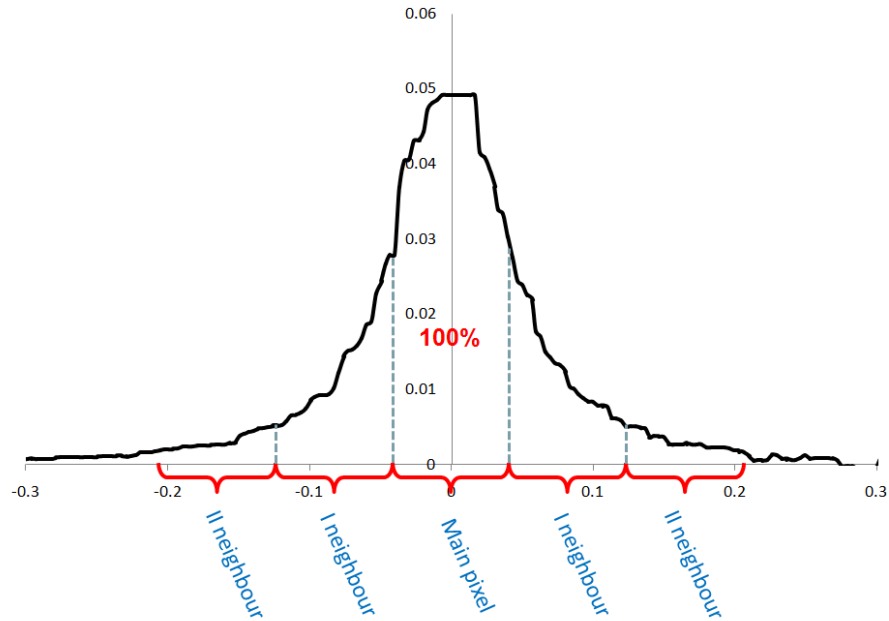


Figure 3.15 Dexela detector's LSF; y-axis corresponds to normalised signal while x-axis corresponds to detector pixels dimensions (mm).

Figure 3.16 summarizes the results of the signal spill out calculations for the 3 tested detectors, in both the horizontal and vertical directions. In all cases, the left and right hand side of the LSF curve gave similar results. Calculations of the vertical and horizontal measurement directions were comparable for the Dexela and Hamamatsu detectors. For the Anrad detector, the spill-out to adjacent pixels was higher in the vertical direction (11.7% and 11.8% on right and left side of the LSF curve respectively compared to 5% and 6% in the horizontal one). This indicates, that for a coded aperture method sensitive to phase effects in one direction only, using the detector in one orientation would provide better results than using it on the other. As a result of being indirect detection devices, the Dexela and Hamamatsu detectors have much higher signal spill-out to neighbouring pixels. For the Dexela detector, slightly higher spill-out to the first neighbours was observed for the horizontal direction (33.5% and 33.6% on right and left side of the LSF curve respectively) compared to the vertical one (31.7% and 31.2%). For the Hamamatsu detector, the situation was the opposite, as higher spill-out was seen for vertical direction 46.7% and 46.2% on the right and left side of the LSF curve respectively, while in the horizontal direction it was slightly lower, 44.9% and 45.9%. Significantly lower percentages of the main pixel signal are detected by the second neighbour pixels for all detectors examined. For the Anrad detector, the signal spill-out into the second neighbours can be ignored, as it is of the order of 1%, while for

other systems it is higher: for the Dexela detector, it is close to 8%, and for the Hamamatsu detector it is around 15%. The difference between the signal spill out values for the direct conversion Anrad detector and the other two indirect systems (Dexela and Hamamatsu) can be primarily attributed to the effect of light diffusion in the scintillator.

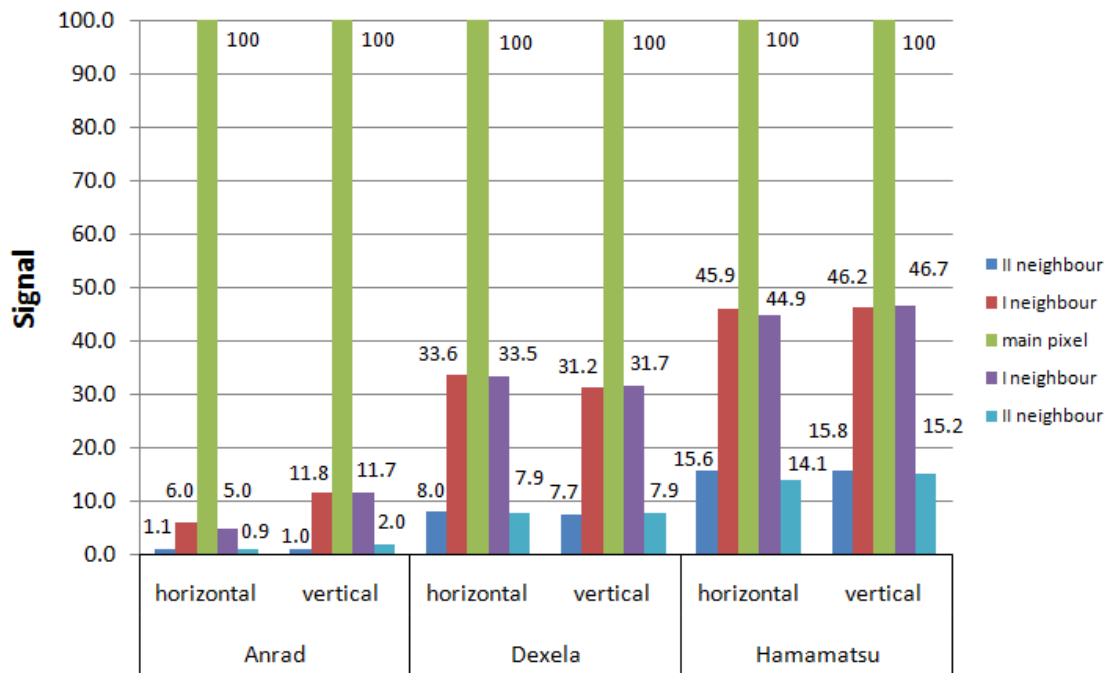


Figure 3.16 Signal spill out (%) of three detectors: Anrad, Dexela and Hamamatsu. For each system signal spill out was calculated in two directions: horizontal and vertical.

The effect of signal spill out on XPCi signal was simulated for 3 illumination levels, 20%, 35% and 50% (see Figure 3.17a, b, c). It can be seen, that as the overlap between the apertures increases, the height of the positive and negative peaks decreases, resulting in lower image contrast for high illumination levels. Different profiles were simulated for 5.5% signal diffusion (Anrad, horizontal case), 12% signal diffusion (Anrad, vertical case), 32.5% signal diffusion (Dexela), and for 46% signal diffusion (Hamamatsu). It can be seen, that the higher the signal spill-out, the lower the difference between the positive and negative peaks, i.e. the lower the image contrast.

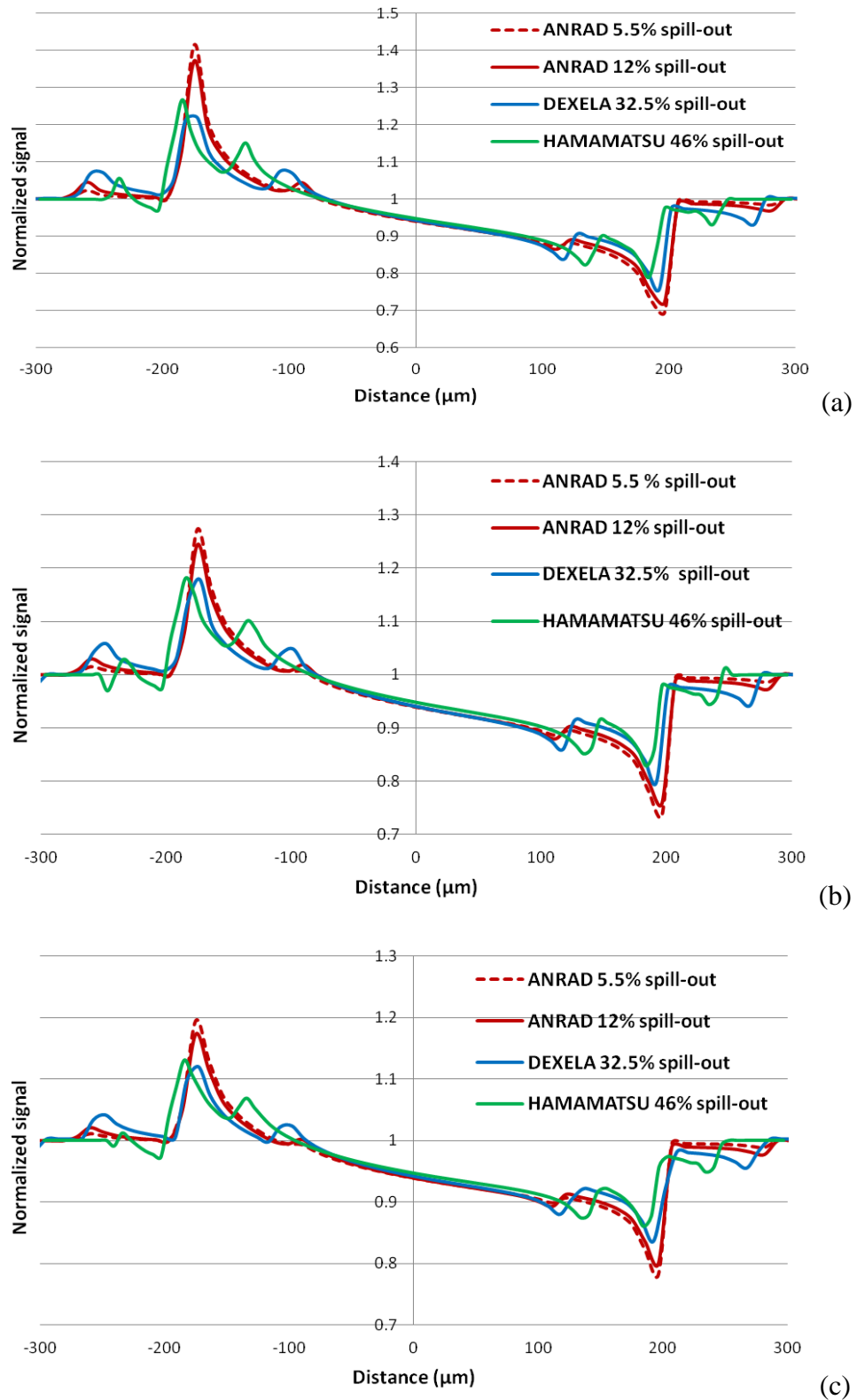


Figure 3.17 Effect of the signal spill out on PC signal at 20% (a), 35% (b) and 50% (c) illumination levels, respectively. For all graphs, the relative intensity is given in a function of displacement.

The contrast calculated as the difference between the positive and negative peaks for each illumination level is summarized in Table 3.4 for each detector tested. As it can be seen, the image contrast is the highest for the horizontal orientation of the Anrad detector, at each illumination level. In fact, the signal spill-out and its influence on the XPCi signal was the main parameter which drove ultimately the decision on the detector choice.

Table 3.4 Image contrast at different illumination levels for 3 detectors tested

Detector	Contrast (%) at illumination level		
	20%	35%	50%
Anrad 5.5% crosstalk (horizontal)	52	43	35
Anrad 12% crosstalk (vertical)	47	39	33
Dexela 32.5% crosstalk	40	33	26
Hamamatsu 46% crosstalk	39	30	24

3.6 Conclusions and choice of the detector for CAXPC Tomosynthesis

The purpose of this part of the study was to perform a complete evaluation of the electro-optical and x-ray performance of three detectors, and select the most suitable one to obtain proof of concept results in CAXPCi based Tomosynthesis. The detectors used for the study were: Anrad SMAM, Dexela and Hamamatsu C9732DK. For the electro-optical characterization, the PTC method was used to measure the performance parameters of the Dexela detector. The results showed the difference in electronic range and dynamic range between the detectors' two modes of operation (HFW and LFW). The x-ray characterization involved measurements of the following parameters: MTF, NPS, DQE and signal spill-out. The MTF and DQE results were then compared with other mammographic systems, obtained under similar experimental conditions. The Anrad detector features the best spatial resolution out of the three evaluated detectors, while the Dexela detector has the best DQE at low mammographic exposures. The signal spill-out results showed that in the Anrad detector, a large proportion of the signal is contained within a single pixel, and only a small fraction of it is spread into the adjacent pixels. For the other two systems, the signal spill out to first neighbours was found to be close to the 1/3 and 1/2 in the Dexela and Hamamatsu detectors, respectively. These results, along with its higher spatial resolution, indicate that the Anrad detector meets the requirements of the CAXPCi system better than the other two.

Chapter 4

4 Comparison between the Free-space-propagation Phase Contrast

Tomosynthesis and clinical Tomosynthesis

4.1 Introduction

The phase contrast effects were exploited in this work firstly under “gold standard” conditions using synchrotron radiation. Although in this case free space propagation XPCi was used rather than CA, this gave us a first opportunity to test the reconstruction algorithms in a situation where XPCi Tomosynthesis slices were acquired with one of the examined digital detectors (Dexela). The experiments were carried out at the Synchrotron Radiation for Medical Physics (SYRMEP) beamline of the Elettra synchrotron radiation facility (Trieste, Italy). The medical physics group in Trieste is currently carrying out a pilot study on the clinical effectiveness of free space propagation XPCi mammography on human patients using synchrotron radiation (Longo et al. 2003; Arfelli et al. 2007; Castelli et al. 2007; Dreossi et al. 2008). The underpinning idea is that FSP provides edge enhancement of the imaged samples, leading to a significant improvement in detail visibility, and thus potentially enabling earlier lesion detection. FSP implementation is the simplest implementation of XPCi and was thus considered the most suited to a first translation into *in vivo* studies on human patients. If the source is sufficiently coherent, optimizing the distance between the sample and the detector is sufficient to become sensitive to phase effects (alongside absorption). However the problem of overlying structures in dense breast is of course still present, hence the desire to test the method also in the tomosynthesis geometry.

Due to the demanding requirements of FSP XPCi on the detector resolution, so far the program has been based on mammography screen-film systems, with the first tests with high-resolution storage phosphor systems having started only recently. This is

suboptimal in many ways, especially as far as the films are concerned, since they only allow the acquisition of analogic images with a limited dynamic range and contrast resolution. It is currently hoped that the storage phosphor system will improve this, but still real-time imaging will not be available, which makes 3D approaches practically impossible. We propose here a possible solution based on the use of a large area CMOS x-ray flat panel detector developed by Dexela (see previous chapter).

4.2 Experimental methods

While the synchrotron experiments were carried out at the SYRMEP beamline, the tomosynthesis images with a conventional source were acquired for comparison purposes using a Giotto system (IMS, Italy). Finally, a Senographe Essential (GE) mammography unit was used for planar imaging.

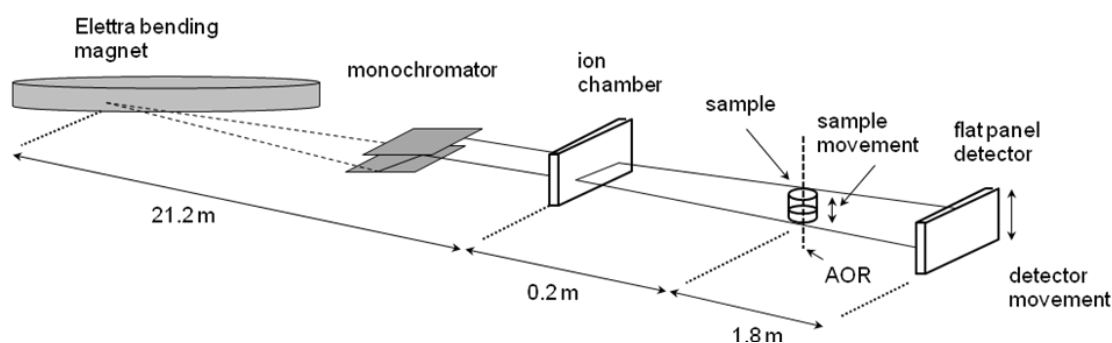


Figure 4.1 Elettra SYRMEP beam-line experimental setup.

Figure 4.1 shows a schematic drawing of the setup used at the synchrotron. An x-ray beam, produced in one of the ring's bending magnets, is directed onto a double-crystal Si(111) monochromator, where the required energy is selected. The typical range of the energies at the SYRMEP beamline is between 8.5keV to 35keV. In our experiments the energy used was 21keV. Dosimetry measurements were obtained with a high precision ionization chamber, which was placed at about 23m from the source. This is the chamber used in the SYRMEP *in vivo* patient project, and its performance is described in (Bovi et al. 2007). The CMOS x-ray detector was mounted on a translation stage at a source-to-detector distance of about 32m. Tungsten slits were used to limit the beam to a cross-section of $206 \times 3 \text{ mm}^2$ on the detector surface. During the acquisition, the detector was scanned vertically with a speed of 15mm/s, over a range covering the

whole area of the sample. The sample was also simultaneously scanned at a slightly reduced speed to preserve the angular velocity and avoid image distortions.

Tomosynthesis experiments, a rotation stage with an angular resolution of 10^{-3} degrees, incorporated in the “scanning bed” used for the patient study (see Figure 4.2 and (Castelli et al. 2007)), was used. During a conventional DBT acquisition scan, the x-ray tube moves along an arc around the patient, with the centre of rotation in the central plane of the patient. The detector follows the movement of the x-ray tube along an equivalent arc, but in the opposite direction. At the SYRMEP beamline, an equivalent geometry was adopted, but by rotating the sample while the x-ray source and the detector were kept stationary. This would be possible also *in vivo*, since as said above the patient scanning bed has this embedded capability. The phantom was rotated over 40° , and 13 projections were taken over this range.

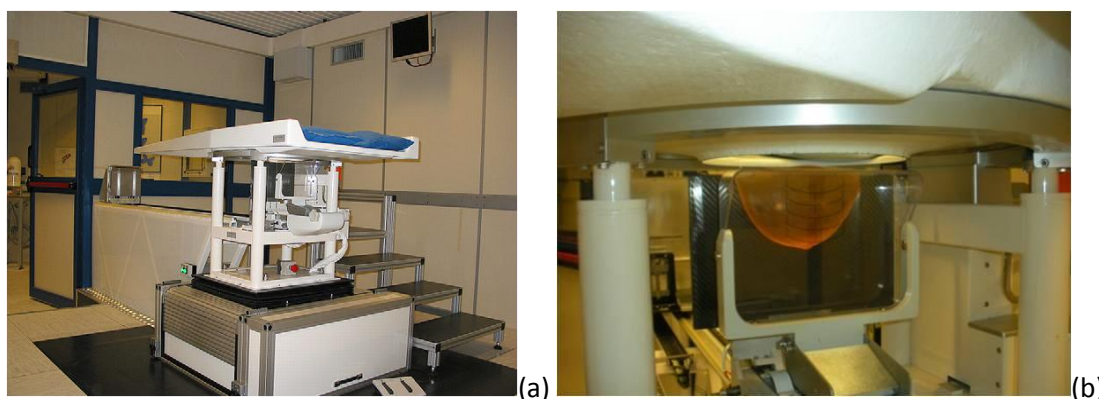


Figure 4.2 Mammography facility at SYRMEP beamline: patient support (a) and positioning of the sample (b)

The planar imaging of the phantom was obtained with a clinical mammography system. The Senographe Essential (GE) system features an x-ray tube (MAXIRay 100TH-M1) with a rhodium/rhodium anode/filter combination, and an indirect conversion a-Si flat panel coupled with a CsI(Tl), with a pixel size of $100\mu\text{m}$. The image of the ACR phantom was taken at the tube voltage of 29 kVp while the image of the biopsy phantom was acquired at the voltage of 28kVp.

“Conventional”, i.e. non synchrotron, Tomosynthesis scanning was obtained with the Giotto (IMS, Italy) digital breast tomosynthesis system (see Figure 4.3). An x-ray tube with tungsten target is used in this system, combined with a direct conversion a-Se thin film transistor (TFT) detector with $85\mu\text{m}$ pixel size. The tube voltage was 27 kVp. The sample was placed in the contact with the detector. The source-to-sample distance

(SSD) was 66,6cm. A set of 13 projections were acquired over a non-equiangular range of 40°. Gain and offset corrections were applied to all the raw images to reduce the structure noise. The images have been reconstructed with the Dexela's software which incorporates the SPS algorithm (see description in chapter 2 of this thesis).



Figure 4.3 IMS digital tomosynthesis system

For planar imaging, the American College of Radiology (ACR) mammography accreditation phantom was used. The phantom contains several test details placed in a wax block. The wax is embedded in an acrylic base, so that a total thickness of 4.0-4.5 cm is achieved, to simulate the thickness of a standard compressed breast. The details included in the wax layer simulate typical breast pathologies: fibres, microcalcifications and tumour masses. The materials used to manufacture these details are nylon fibres, aluminium oxide particles and phenolic disks to simulate fibres, microcalcifications and masses, respectively. Figure 4.4a shows the locations of the features inside the phantom. The thickness of the fibres is decreasing gradually from 1.56mm to 0.4mm for fibres from F1 to F6, respectively. The specks with diameters from 0.54mm (S1) to 0.16mm (S5) are organised in groups, each consisting of six specks. Finally, the diameter of tumour like masses, M1 – M5, decreases gradually from 2mm to 0.16mm.

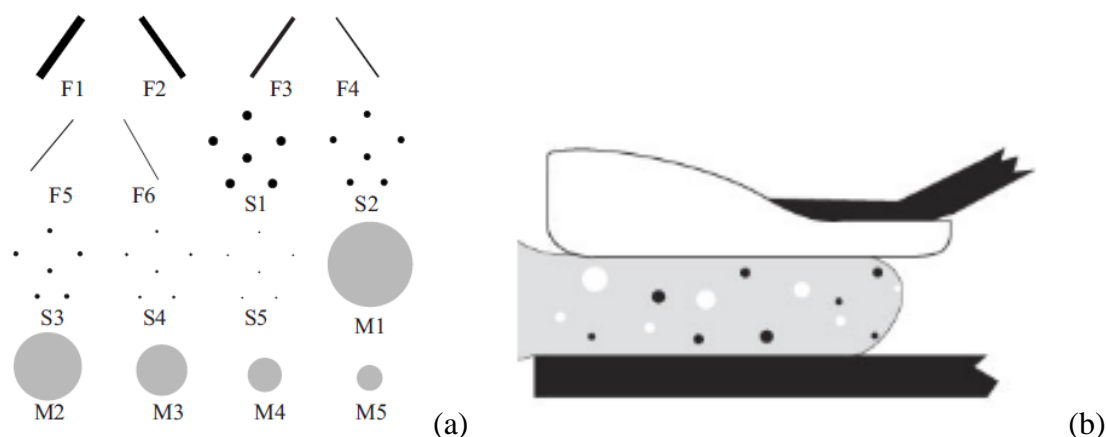


Figure 4.4 Schematics of: (a) American College of Radiology accreditation phantom containing six fibres (F1 to F6), five microcalcification specks (S1 to S5) and five tumour-like masses (M1 to M5), (b) stereotactic biopsy phantom

A Stereotactic Needle Biopsy Phantom (Figure 4.4b) was used for both planar and Tomosynthesis imaging. The phantom is a standard tool for quality assurance in stereotactic systems. The phantom is shaped as to represent a partially compressed breast which results in the standard thickness of 4.5cm. A number of randomly placed solid masses in the range of 3 to 6mm simulate the tumour masses. Two calcifications clusters are positioned in the middle plane of the phantom. The diameters of the calcifications range from 300 μ m to 350 μ m.

4.3 Results and discussion

Figure 4.5 shows a comparison between conventional and synchrotron radiation planar images of the ACR phantom. The MGD delivered to the phantom was estimated to be 0.93mGy at 21keV in synchrotron imaging and 1.14mGy at 29kVp in the mammography system. The corresponding entrance surface air kerma (ESAK) measured on the detector surface was 2.15mGy and 4.29mGy for synchrotron and conventional imaging, respectively. For comparison, in standard 2D mammography the MGD depends on factors such as breast grandularity, spectrum and imaging system used, and it can typically ranges from 1.7mGy to 2.1mGy and from 2.1mGy to 2.5mGy per one view for digital and screen-film mammography systems, respectively (Hendrick et al. 2010). Although the acceptable level of the MGD delivered to a breast equivalent thickness of 4.5cm is 2mGy (Young et al. 2005), in our study the MGD was kept below 1mGy per image (i.e. 0.93 mGy). The specks larger than or equal to 320 μ m were easily

detectable in both conventional and synchrotron images. The specks with a diameter equal to $160\mu\text{m}$ were detectable only in the synchrotron images. The lower detectability limit of fibre thickness for a conventional system was $750\mu\text{m}$, while fibres with thicknesses down to $400\mu\text{m}$ were still visible in the synchrotron images. The phase contrast effects are visible at the edges of the fibres as dark and bright fringes (see the enlarged ROIs in Figure 4.5). Significant advantages were observed also on the imaging of the masses, as details with a diameter of $160\mu\text{m}$ were detectable in synchrotron images while the conventional system was limited to masses with a diameter of $500\mu\text{m}$.

Figure 4.6 shows a planar image of a region of about 600×1000 pixels of the biopsy breast phantom (corresponding to approximately half image). The measured ESAK was 1.21mGy and 3.95 mGy for the synchrotron and the laboratory image, respectively. This corresponds to an MGD delivered to the phantom of 0.52mGy and 1.1 mGy for the synchrotron and the laboratory image, respectively. A substantial increase in the contrast of the tumour masses and of the calcifications can be observed by comparing the synchrotron with the conventional image. In the synchrotron image, phase contrast effects are visible at the boundaries of the tumour-like masses as dark and bright contours on the inside and outside of the masses, respectively.

The biopsy stereotactic breast phantom was then used in both the synchrotron and the laboratory tomosynthesis experiments. In both cases, the phantom has been compressed to a thickness of 4cm . The MGD delivered to the sample during a single tomosynthesis projection at the synchrotron facility was estimated to be 0.32mGy , while this value was 0.2 mGy for the conventional tomosynthesis image. The MGD of the entire scan was 4.16 mGy and 2.7 mGy for the synchrotron and conventional tomosynthesis imaging, respectively. Note that a typical MGD delivered to the compressed breast is 1.5mGy per projection (Dance et al. 2000), which results in 3mGy in a standard mammography examination, where two projections are required for a full diagnosis. Five reconstructed slices are presented in Figure 4.7, which shows the images obtained with the clinical tomosynthesis system and with the synchrotron radiation. The reconstruction planes are 0.5mm thick and cover the whole area of the phantom (i.e. $20\text{cm} \times 15\text{cm}$). Ten iteration steps were used in the reconstruction.

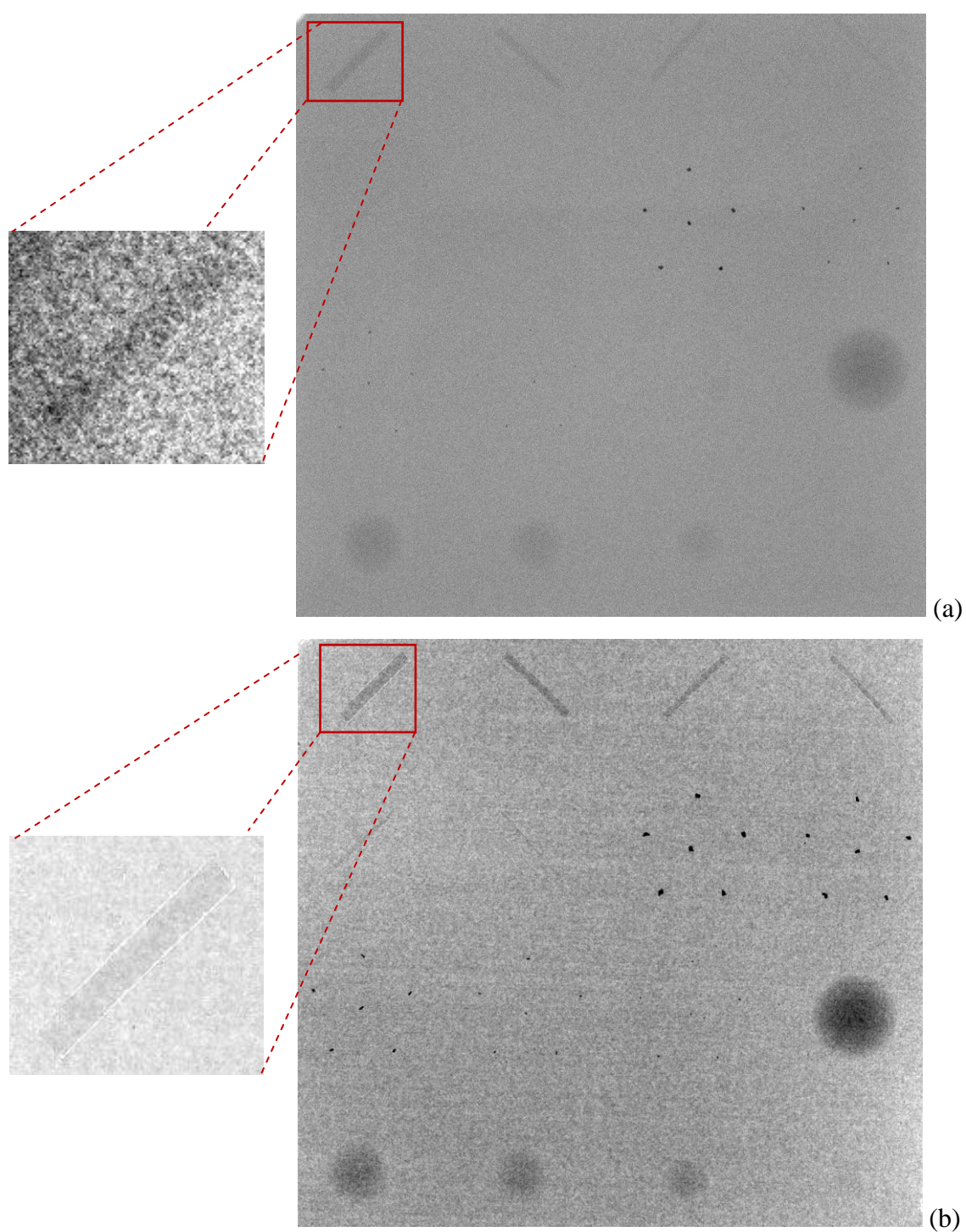


Figure 4.5 Images of an ACR phantom with a selected ROI (left) obtained with a) a laboratory system and b) using synchrotron radiation

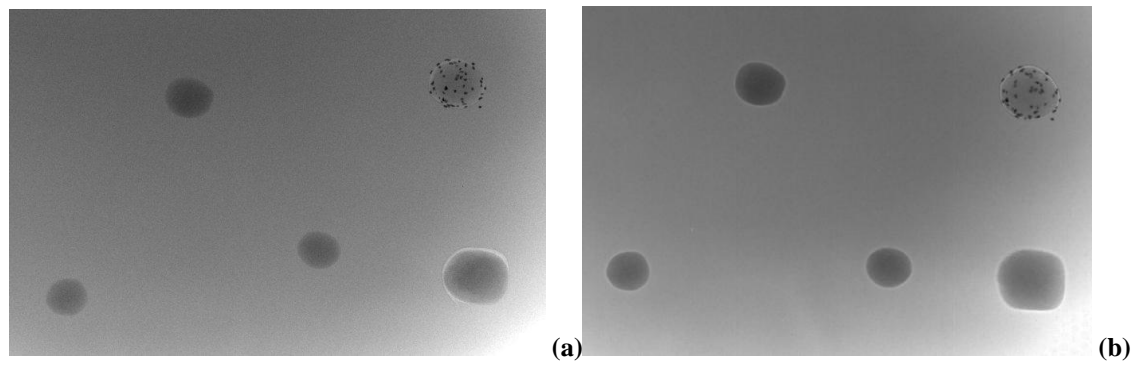


Figure 4.6 Planar image of a ROI in the biopsy phantom obtained a) with conventional mammography system and b) using synchrotron radiation

As expected in tomosynthesis imaging, all reconstructed slices suffer from typical artefacts: out of plane objects cause blurring artefacts, while the edges of objects in the plane of focus are crisp.

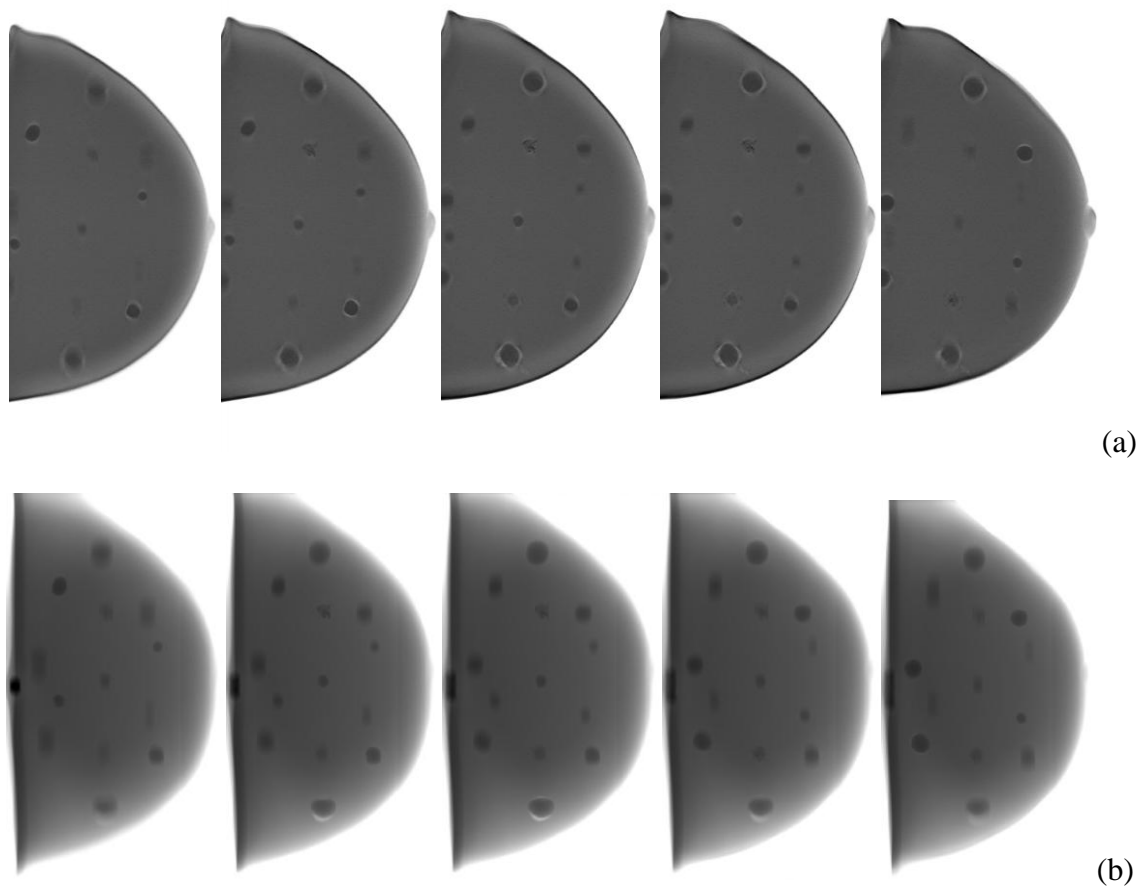


Figure 4.7 Selected reconstructions of the biopsy phantom obtained with the clinical tomosynthesis system (a) and using synchrotron radiation (b). Different features are in focus when slicing through the reconstructed volume from left to right. The objects that are not in the plane of focus appear as multiple replicas causing blurring artefacts.

Figure 4.8 shows a comparison between the signal obtained with a clinical TS system and with synchrotron radiation of an ROI of a single projection at angle 0° consisting of a tumour-like mass. Although the phase contrast signal is weak (which could be due to the excessively large pixel size of the CMOS sensor which washes out the phase contrast fringes), it can still be clearly observed only in the synchrotron images at the boundaries of the object (the arrows in Figure 4.8 point the phase contrast peaks). Note that the phase signal is visible all around the object. The image contrast is two times larger in the synchrotron projections than in those obtained with a clinical system (see Figure 4.10). Likewise, a significant increase in the CNR can be seen for the synchrotron images. The latter is due to the lower noise obtained with synchrotron radiation.

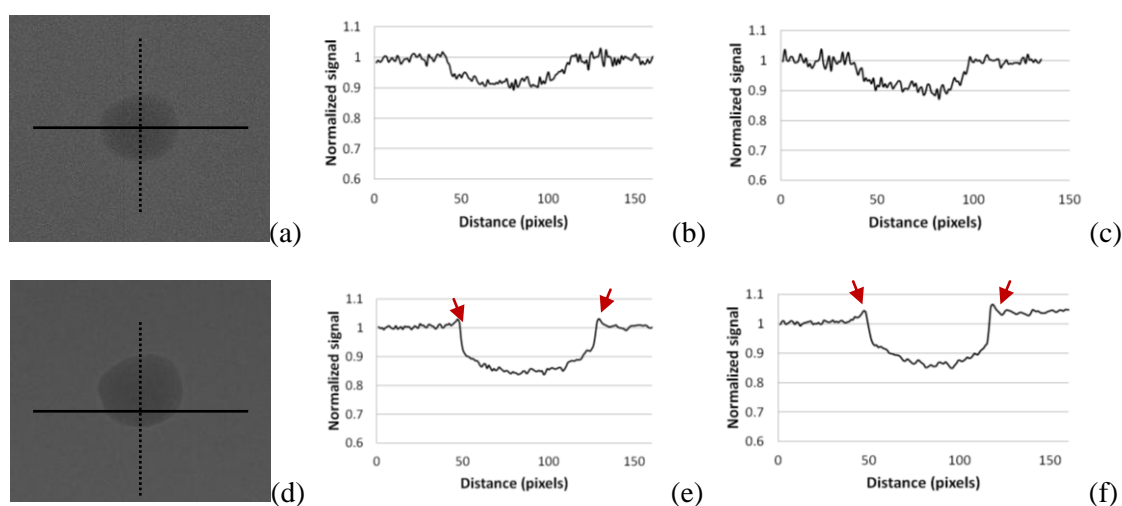


Figure 4.8 Single projections at 0° (a, d) and corresponding horizontal (b, e) and vertical (c, f) profile plots obtained with a conventional TS system (a, b, c) and with synchrotron radiation (d, e, f)

Figure 4.9 shows an ROI of the reconstructed tomosynthesis image consisting of the same tumour-like object. While the images obtained with synchrotron radiation preserve the phase contrast signal, the lack of it can only be clearly seen in the vertical profile plot (Figure 4.9c) of the image taken with the clinical system. This can only be explained assuming that the bright fringes, that can be seen in the horizontal direction of the clinical image, are not due to phase effects, but are rather ghosting artefacts related to the cone beam geometry. If these are ignored, both image contrast and CNR are superior for the images obtained with synchrotron radiation compared to those taken with the clinical system.

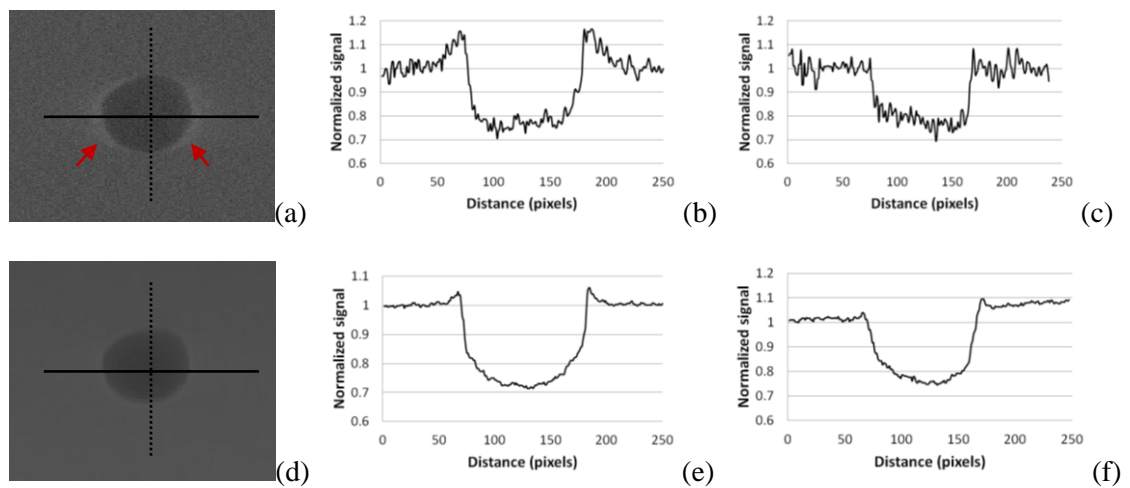


Figure 4.9 Reconstructions (a, d) and corresponding horizontal (b, e) and vertical (c, f) profile plots obtained with a conventional TS system (a, b, c) and with synchrotron radiation (d, e, f)

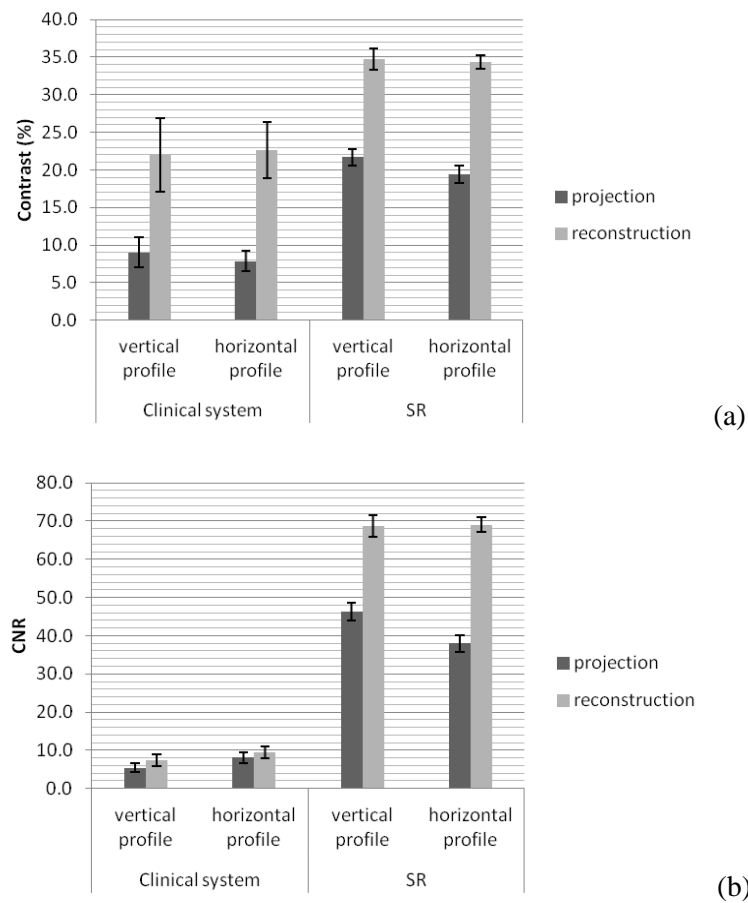


Figure 4.10 Contrast and CNR calculated for the clinical and synchrotron projection and reconstructed image from Figure 4.8 and Figure 4.9.

4.4 Conclusions

The results of the phase contrast imaging using FSP method and synchrotron radiation were presented in this chapter along with the results obtained with a conventional absorption-based imaging system. This exercise was performed for planar and TS imaging using an ACR and a biopsy phantoms, respectively. A large-field flat panel mammographic detector was used to acquire the images. The results of the imaging of the ACR phantom show that the phase contrast effects are visible only in the synchrotron images acquired with the FSP method. Moreover, the images exhibit strong phase contrast signal at the edges of the features, despite the large size of the detector pixel. The results of the TS imaging of the biopsy phantom show that the phase contrast signal is well preserved while rotating the sample, and appears as bright and dark fringes around the objects in each reconstructed plane throughout the object's volume.

Chapter 5

5 Proof-of-concept results of Coded-Aperture Phase Contrast Tomosynthesis

5.1 Introduction and chapter overview

In this chapter proof-of-concept results from preliminary study of Coded Apertures Phase Contrast Tomosynthesis (CAPCTS) will be presented. The first part of the study involved setting up the system in the laboratory and optimize it for tomosynthesis acquisitions. At this stage, entrance dose measurements were also performed. The mean glandular dose (MGD) was then estimated for the TORMAM phantoms.

The second part of this chapter presents the results of the CAXPCi tomosynthesis simulations, as well as their experimental verification. Two vertically arranged, low absorbing, small diameter wires were used for the simulations and the experiments. Two models were used to simulate the phase contrast profiles: a simple geometrical model (Olivo and Speller 2007), and a more sophisticated Monte Carlo ray tracing model (Millard 2012) based on the McXtrace software package. The planar simulations and the planar experimental data aim to confirm that both models correctly simulate the phase contrast signal for overlapping structures. A tomosynthesis scan of the wire sample then was performed, and vertical slices were reconstructed from the datasets by using the SPS algorithm. The plots from these slices were compared to their simulated counterparts.

In the third part of this chapter, to validate the technique on thicker samples and under more realistic conditions, a sample made by overlapping two TORMAM phantoms was imaged in the tomosynthesis geometry, and the slices were reconstructed with the SPS algorithm. In both cases, an intense phase contrast signal was preserved in the separated planes.

Finally, an attempt was made to compare the proposed technique with a conventional absorption based tomosynthesis acquisition using the two overlapping TORMAM phantoms. The Giotto digital tomosynthesis system was used to obtain the conventional tomosynthesis projections.

5.2 Setting up the Coded Apertures Phase Contrast system

The CAXPCi system at UCL is undergoing continuous developments, upgrades and tests. The goal of these modifications is to build up a system that could demonstrate the advantages of x-ray phase contrast imaging over conventional methods under laboratory conditions. Figure 5.1 shows the set-up used in this work for both the experimental validation of the mathematical simulations in the tomosynthesis geometry and for the imaging of phantoms and other samples. The biggest effort was dedicated to three major tasks: upgrade of the x-ray source, choice of the best detector and optimisation of the masks alignment procedure.

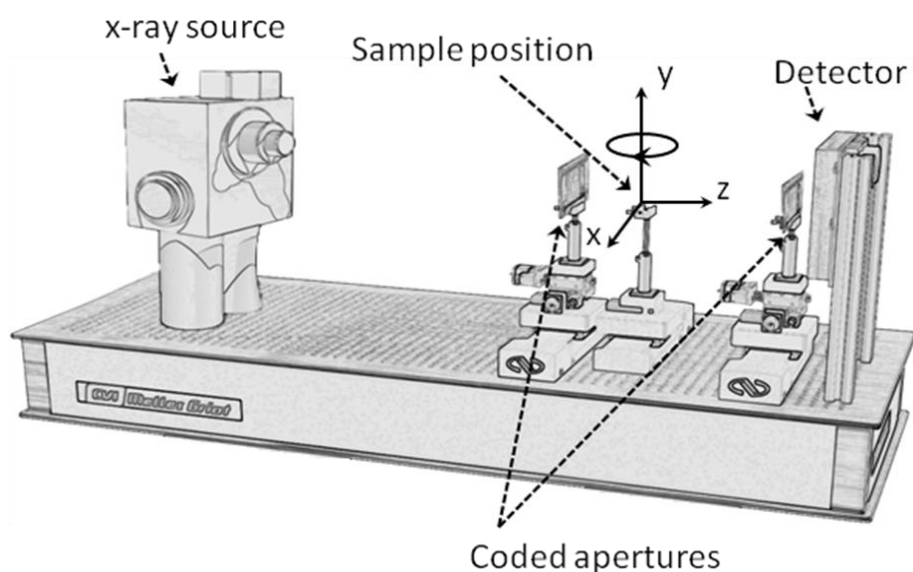


Figure 5.1 CAXPCi Tomosynthesis setup.

5.2.1 X-ray source

A high-power Rigaku MicroMax-007 HF rotating anode x-ray tube is used for the experiments. The source features a focal spot ϕ of $70\mu\text{m}$. The maximum current the source can tolerate is 30mA at energy of 40kVp. Molybdenum target and filtration is used.

5.2.2 Masks alignment

The schematic drawing of the masks used in the CAXPCi system is shown in Figure 5.2. The detector mask is aligned with the detector pixel columns, effectively creating insensitive regions between adjacent detector pixels. The sample mask apertures create individual beams, the refraction of which (caused by the sample) on or off the detector mask generates the signal. The width of the apertures is $20\mu\text{m}$ and $12\mu\text{m}$ for the detector and sample mask, respectively; while the pitch is $83\mu\text{m}$ and $66.8\mu\text{m}$ for the detector and sample mask, respectively. Precise masks alignment is of a paramount importance, thus a comprehensive study was performed in order to establish a reliable procedure for mask alignment. Two cradles and a rotation stage, which allow rotating the masks around the three coordinates: x, y and z (see Figure 5.1) are used. The x axis is perpendicular to the beam path, and corresponds to the direction in which mask scanning is performed to vary the “illumination level”. The y axis is perpendicular to the table surface and is used to adjust the height of the masks and the sample. The z axis corresponds to the optical axis of the system i.e. to the beam direction. The angles around the x, y and z axes are termed φ , the “rotation” (Rot) and θ , respectively.

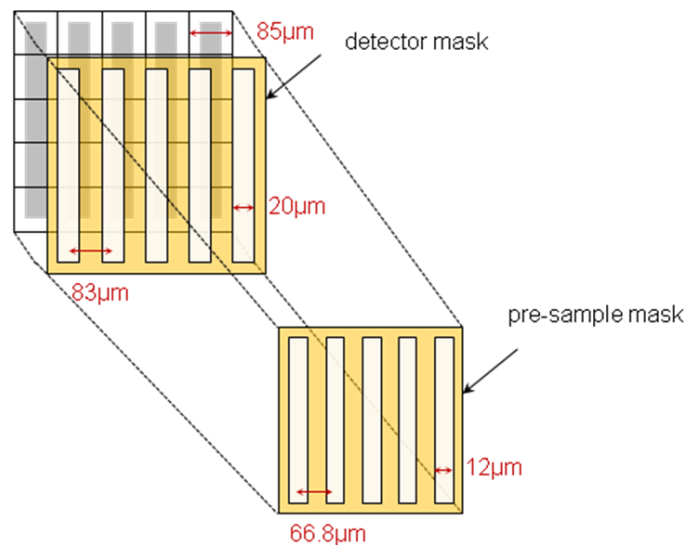


Figure 5.2 Coded apertures

Φ adjustment

The misalignment of the masks apertures is made evident by the appearance of Moiré patterns (interference pattern created when two or more grids are overlaid at an angle) in the acquired “flat” (i.e. in the absence of the sample) image. The first step to align the masks is to rotate one mask over φ , so that the apertures in the two masks become

parallel. This does not eliminate the Moiré fringes, but it makes them parallel to the detector pixel columns. Similarly, the detector mask must be aligned with the detector pixel columns.

Figure 5.3 shows the Moiré pattern which appears as a consequence of the misalignment of two masks. If p is the spacing between two adjacent apertures of the mask, and d is the spacing between two consecutive Moiré fringes, then the angle φ between the apertures in the two masks can be calculated as $\varphi = \arctan(p/d)$. By rotating one of the masks by φ , the Moiré pattern fringes become parallel to the detector pixel columns. To make them disappear, the z distance between the two masks has to be adjusted.

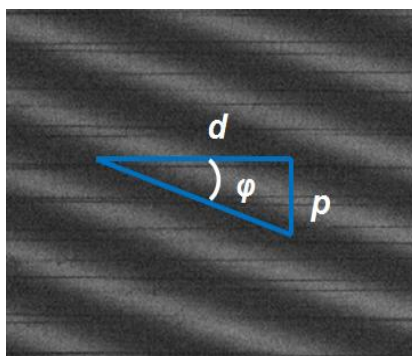


Figure 5.3 Moiré pattern of the two misaligned masks rotated by an angle φ with respect to each other

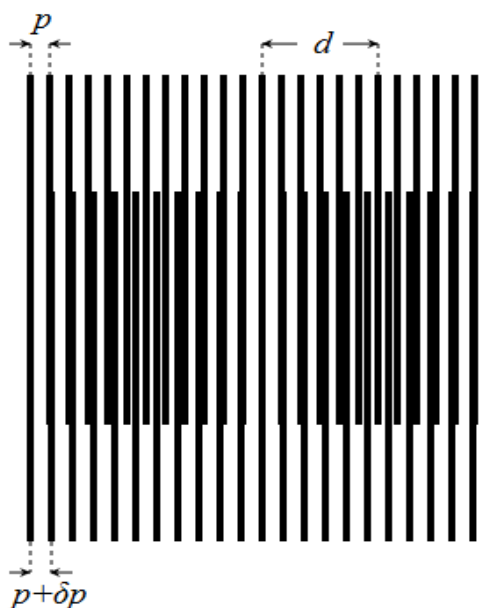


Figure 5.4 Moiré pattern of two masks aligned with respect to φ but not correctly positioned along the z axis

***z* adjustment**

The optimal distances of both sample and detector mask from the source can be found by changing their positions along the *z*-axis. One can again use the Moiré fringes. **Error! Reference source not found.** shows a schematic of the geometrical description of the moiré pattern for apertures mutually aligned along ϕ . Two grids with parallel and equidistant lines (apertures) are considered. The step of the first pattern is p and the step of the second pattern is $p + \delta p$.

The superimposed patterns create dark and bright fringes. The distance between two subsequent bright fringes (equal to the distance between two dark fringes), $2d$, is given by $p^2 / \delta p$. Therefore the shift between the patterns δp can be calculated as $\delta p = p^2 / 2d$. By translating the masks in the *z*-direction, the projected period of the masks also change. If the mask being aligned is moved in steps towards the correct *z*-position, the period of each consecutive step becomes larger, until the fringes disappear, which indicates an ideal *z*-position.

In order to place the masks at the correct *z* distance from each other, the relative shift (Δz) must be calculated by simple geometric considerations (see Figure 5.5). The actual source to sample mask distance and the ideal source to sample mask distance are z_1 and z_2 , respectively. The ideal pattern pitch p (or CD) at z_1 can be calculated by downscaling AB. Next, assuming that the triangles OCD and OEF are equivalent, one can calculate the ideal source to sample distance z_2 from the geometrical relation: $p / z_2 = (p + \delta p) / z_1$ and the relative shift (Δz) between the masks is then calculated as $z_2 - z_1$.

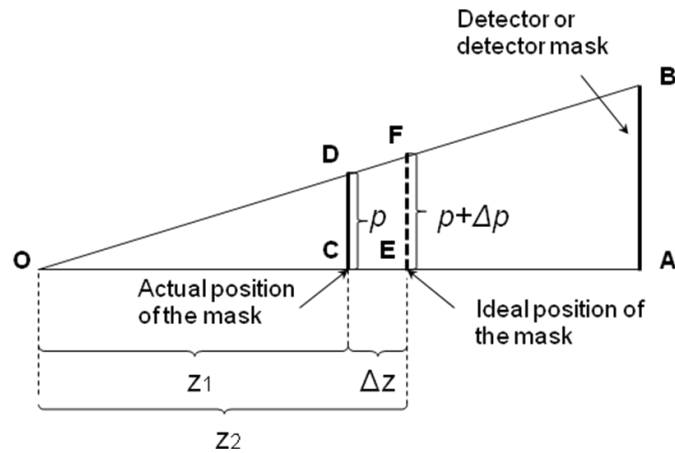
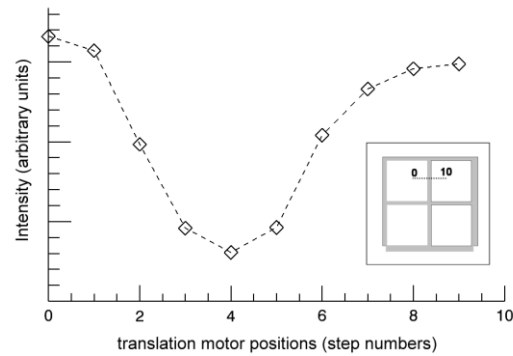
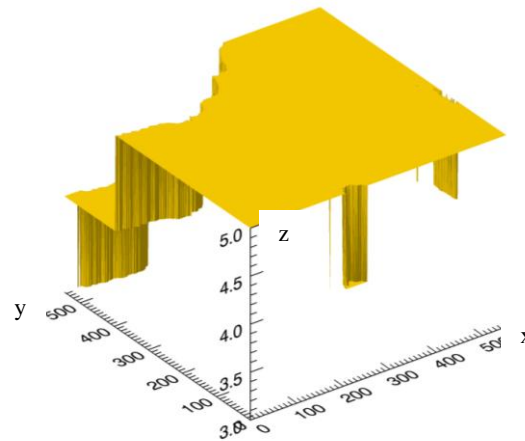


Figure 5.5 Geometry of the z distance calculations.

The above method, however, does not provide a complete alignment procedure of the masks as the accuracy of the alignment is not sufficient. An alignment with a precision of few micrometers can be achieved if shape of the detector pixel point spread function is used as an analyser tool. This can be measured directly by scanning the masks in sub-pixel steps in the direction orthogonal to the pixel columns and plotting the detected signal versus the mask position. First, the detector mask, which has a grating period comparable to the detector pixel, is translated along the x -axis in small steps until the centre of each detector mask slit matches the centre of every corresponding detector pixel column. This is achieved in two steps: first by aligning the centre of the slit with the edge of the detector pixel (where the sensitivity to the acquired signal is lowest), then shifting the mask by half a pixel. An example of the pixel response for one scan with 10 sub-pixel steps is shown in Figure 5.6a. The minimum of the plot indicates the step for which the centre of the detector mask slit is aligned with the edge of the detector pixel, from which the mask is then moved by half a pixel. The value of this function is then plotted on a pixel by pixel basis over a large number of pixels in a 3D plot (see example in Figure 5.6b). The x and y axes of the plot correspond to a square ROI within the masks with a size of 500×500 pixels. The vertical axis corresponds to the number of illumination steps for which the minimum of the pixel response is found. An ideal alignment of the detector mask with the detector matrix corresponds to a flat surface of the alignment plot, i.e. to a situation in which, for each pixel in detector array, this minimum is reached at the same translation step. In practice, however, this is never the case due to masks defects, which may cause local changes in the detector response function. The same alignment procedure is then repeated for the sample mask.



(a)



(b)

Figure 5.6 Masks alignment check diagram.

5.2.3 Dose measurements

An accurate dosimetry is an essential element of the quality control of any imaging system. Moreover, when new imaging modalities are developed which make use of ionizing radiation measuring the dose delivered to the sample is key to assess the possible clinical applicability. Several standard protocols exist for the estimation of breast dose in conventional projection mammography (IPEM 2005; EC 2006; IAEA 2006). Since the most radiation-sensitive part of the breast is the glandular tissue, the mean glandular dose (MGD) is usually calculated as an indication of the radiation risk in mammography. The basic idea is to estimate the mean glandular dose for a given incident air kerma measured on the breast surface (Dance et al. 2009). Monte Carlo simulations are used to calculate correction factors which take into account the x-ray spectra from different target/filter combinations (Dance 1990; Dance et al. 2000; Dance et al. 2009) as well as for different levels of granularity and breast thickness (Dance 1990; Dance et al. 2000).

The mean glandular dose can be calculated from the following formula:

$$MGD = K_{air} gcs \quad (5.1)$$

where K_{air} is the incident air kerma measured on the surface of the breast, g is a conversion factor that considers a breast granularity of 50%, s is a correction factor for the different x-ray spectra, and c is an additional correction factor that allows for breast granularities different than 50%.

The above definition of MGD has been extended to a tomosynthesis geometry by adding two further correction factors: t-factors and T-factors (Dance et al. 2011). The t-factors correspond to a single projection at a given angle θ , while the T-factors take into account the complete tomosynthesis scan. The extended definition of MGD for a tomosynthesis scan becomes:

$$MGD_{TS}(\theta) = K_{air} gcs \cdot t(\theta) \quad (5.2)$$

The $t(\theta)$ in the above equation is calculated as the ratio between the MGD calculated at a projection at angle θ and the MGD at projection angle 0° calculated for the same x-ray spectrum and tube loading:

$$t(\theta) = MGD(\theta) / MGD(0^\circ) \quad (5.3)$$

The T-factor can be then calculated as the sum of $t(\theta)$ for all projection angles. Both t-factors and T-factors have been estimated by Monte Carlo simulations and are tabulated in (Dance 2011). The t—factors depend on the breast thickness and on the projection angle, and range from 0.997 for a breast thickness of 20mm and projection angle of 5° , to 0.834 for a breast thickness of 110mm and a projection angle of 30° . In this study, mammographic phantoms were used with a thickness of 33mm and the angular range of -7° to 7° was typically employed. According to Dance (Dance et al. 2011), the correction factor T for an angular range of -10° to 10° and a breast thickness of 30mm would be 0.986, giving a difference of 1.4% on the MGD. This difference would thus be even smaller for the angular range used in this work.

The main limitation on the calculation of the MGD with equation (5.1) for the CAXPCi system is that the conversion factors g , c and s have been simulated only for typical mammographic spectra, i.e. 25-35kV. In this study energy of 40kV was used. In order to estimate the MGD, the measured air kerma was corrected with the normalized glandular dose D_{gN} extracted from (Boone 1999). In this paper, the values of D_{gN}

obtained with the Monte Carlo simulations are tabulated for high energy beams and for non standard x-ray spectra. The author compares the estimated values with the ones estimated previously by Dance (Dance 1990) and finds a good agreement. D_{gN} depends on the fractional energy absorption, x-ray spectrum, glandular fraction in the breast and the breast thickness (Boone 1999).

The entrance dose (air kerma) in the CAXPCi setup was measured with three dosimeters: a calibrated ionization chamber (KEITHLEY 35050A Dosimeter), thermoluminescent detectors (TLD-100H) and a semiconductor dosimeter (Piranha). Figure 5.7 shows the experimental setup for the dose measurements. Lead shielding has been added in front of the sample mask to remove possible scatter from other equipment components. A ionization chamber has been chosen as the “reference” dosimeter, due to its high stability, repeatability and low energy dependence (IAEA 2007). The ion chamber was placed at a distance of 1.6m from the source, which corresponds to the position of the sample. The measurements were obtained with the same x-ray source settings used in the experiments, i.e. tube voltage at 40kVp and current of 25mA. In order to also take the backscatter into account, a TORMAM phantom and three blocks of polymethacrylate (PMMA), for a total thickness of 4.4cm, were placed behind the ion chamber.

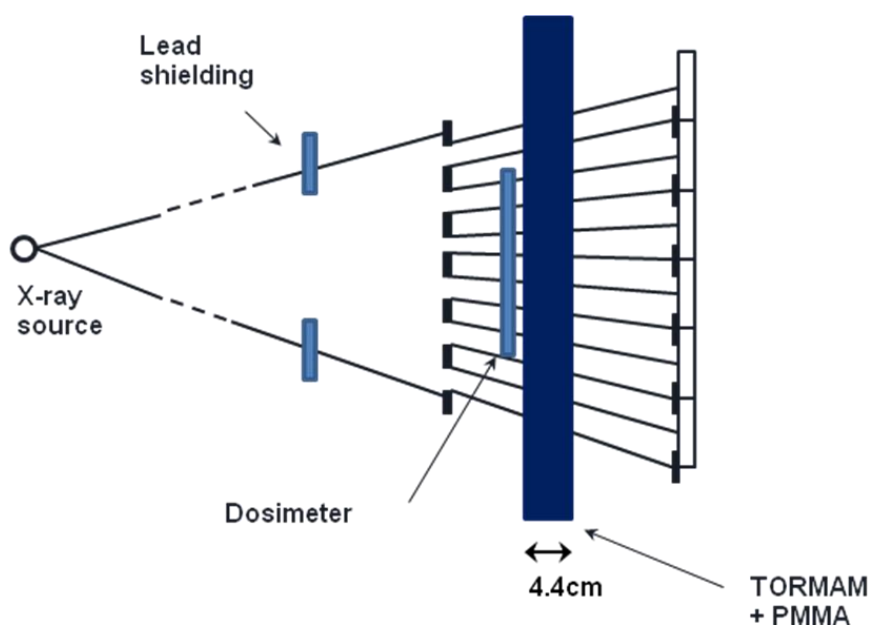


Figure 5.7 Schematic drawing of the experimental setup for dose measurements.

The ESAK values measured with the dosimeters were 0.76mGy, 0.61mGy and 0.89mGy for the ion chamber, the TLD and the solid state dosimeter, respectively. The differences could be explained by the different sensitivity of the dosimeters to low energy photons, plus possible calibration errors. By placing the dosimeter immediately downstream of the pre-sample mask, exactly as done with the real sample, both the beam fractionation introduced by the mask and any possible transmission through the gold are accounted for. A potential source of error lies in the non-uniform nature of the x-ray field illuminating the dosimeter, which could result in a local breakdown of the equilibrium conditions; a thorough explanation of this effect, however, would require the development of a dedicated Monte Carlo simulation and lies outside the scope of this work.

5.3 Phase Contrast signal simulations

5.3.1 Planar simulation

5.3.1.1 Description of the simulators

Two different computer simulations were used to model the experimental conditions, one of which had already been experimentally validated, while the other shows high potential for future work. Both are forward models based on a ray-optics approach; however, they differ in the way the sample is modelled. In the first model, the refraction angle of a photon is calculated as the gradient of the refractive index decrement inside the imaged sample (Olivo and Speller 2007). The McXtrace based model instead calculates the refraction angle using a vectorial form of the Snell's Law (Millard 2012). The sample introduced in the simulations is the same as in the experiment: two plastic wires with different diameters, placed at a distance of 2cm from each other. Only the plane containing the optical axis (z-axis) of the system is simulated. Therefore the phase contrast signal obtained from the simulations is determined only by the cross-section of the objects. In order to simulate the full z image representing the wires, the individual image profile is then "repeated" z number of times, exploiting the symmetry of the system. The 2D model developed by Olivo and Speller (Olivo and Speller 2007) simulated a single wire in the CAXPCi set up. In this model, the x-rays are generated by a source with a Gaussian shape, which emits evenly distributed x-rays within a specified

angular range. The input parameters are the number and dimensions of the pixels as well as pitches and aperture sizes in coded aperture masks, the number of dithering steps, plus source-to-sample and sample to detector distances, and the characteristics of the sample (β and δ), which also determine the simulated x-ray energy.

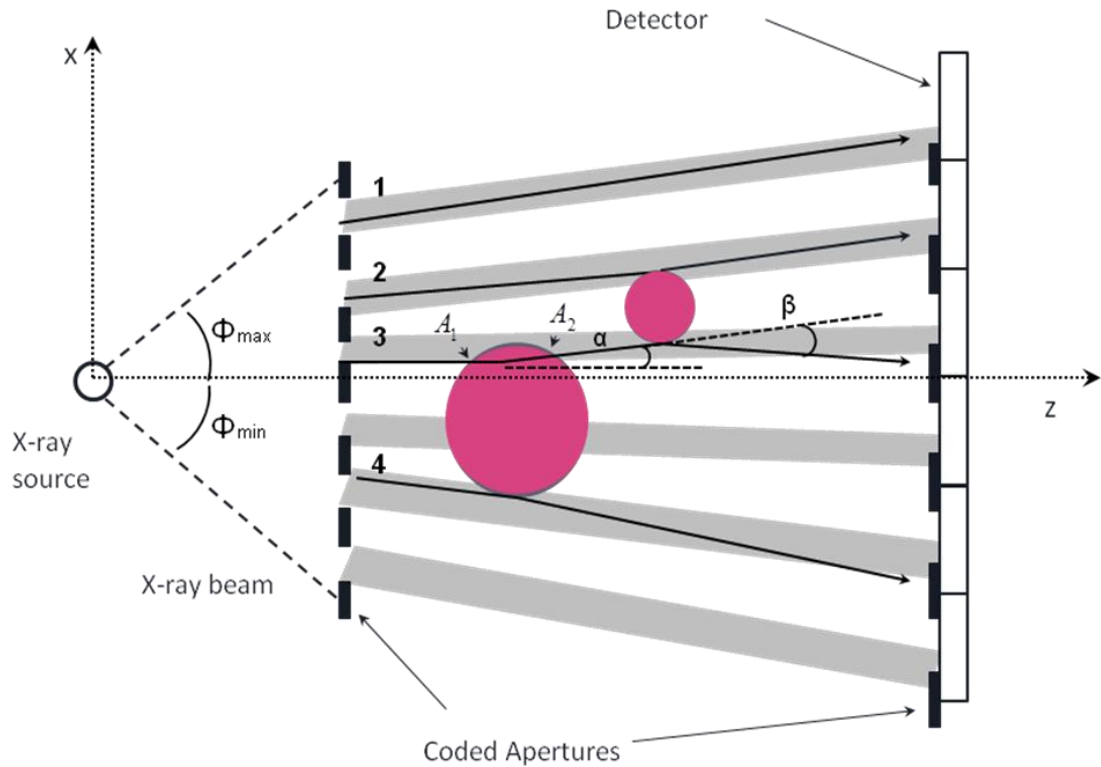


Figure 5.8 Schematic drawing of the CAXPCi simulation scheme with two “overlapping” wires. The maximum angular range of the photons leaving the x-ray source is from Φ_{\min} to Φ_{\max} . Numbers 1-4 indicate examples of possible photon paths (see text for description). The angles α and β are the refraction angles for photon “3” caused by the large and the small sample, respectively.

As the original model included a single wire, it has been extended to allow the simulation of two overlapping wires. Figure 5.8 shows a schematic of the simulated CAXPCi setup. A mathematical description was developed for the signal generated by two overlapping wires. This requires photons deviated by the first wire to be taken as input for possible interactions with the second wire, and the original code was modified accordingly. All possible photon paths are simulated in the model, and ultimately photons which pass through apertures in both x-ray masks are detected. With the introduction of a sample, photons interacting with it are refracted and change their path. Depending on the refraction angle, these photons can be detected or can be absorbed by

the septa in detector mask. If a sample consisting of two wires is considered, interacting photons can be refracted by one wire only or by both wires consecutively. The arrows in Figure 5.8 represent some examples of possible photon paths. Photon '1' passes through the sample mask, does not interact with any sample, and is detected in one of the detector's pixels. Photon '2' is refracted by the small wire only, and is detected. Photon '3' interacts with the large wire and its path is deviated at an angle α . Subsequently, it interacts also with the small wire, undergoing further refraction at different angle β , and it eventually hits the insensitive part of the detector mask, i.e. is not detected. Photon '4' is refracted only by the large wire, and is not detected.

The refraction angle α is calculated according to the method described in (Olivo and Speller 2007). One needs to find the coordinates of the points A_1 and A_2 in Figure 5.8 which correspond to the intersections of the x-rays with the sample. This can be calculated from the following system of equations:

$$\begin{cases} x = mz \\ x = \sqrt{R^2 - (z - d)^2} \end{cases} \quad (5.4)$$

where $m = \tan \theta$ is the angular coefficient that identifies each photon emitted by the source (at angle θ with respect to z-axis); R is the sample radius, and d is the source-to-sample distance. One can calculate the length of a vector $\overline{A_1A_2}$ as:

$$\overline{A_1A_2} = \sqrt{(z_2 - z_1)^2 + (x_2 - x_1)^2} = 2\sqrt{\frac{R^2 - m^2d^2 + m^2R^2}{1 + m^2}} = 2\sqrt{R^2 - d^2 \sin^2 \theta} \quad (5.5)$$

where the in the intermediate passage, the relation $m = \tan \theta$ was used. Here two assumptions were made. First, the centre of the sample was assumed to be at a source-to-sample distance d , while in fact, it is at a distance $d+R$. However, d is typically greater than 1m while R is in the order of μm so it can be neglected. Also, the photon path joining A_1 and A_2 was assumed to be a straight line.

The phase shift Φ caused by the sample is calculated from the following formula:

$$\Phi = \frac{2\pi\delta}{\lambda} \overline{A_1A_2} = \frac{4\pi\delta}{\lambda} \sqrt{R^2 - d^2 \sin^2 \theta} \quad (5.6)$$

The angle of refraction is then calculated as a gradient $\vec{\nabla}$ of the phase shift:

$$\alpha = \frac{\lambda}{2\pi} |\vec{\nabla}\Phi| \quad (5.7)$$

The phase gradient in equation (5.7) can be written in polar coordinates as:

$$\vec{\nabla}\Phi = \frac{\partial\Phi}{\partial r} \hat{r} + \frac{1}{r} \frac{\partial\Phi}{\partial\theta} \hat{\theta} \quad (5.8)$$

where \hat{r} and $\hat{\theta}$ are the basic versors in the polar plane. Since the phase shift depends only on the angle θ , the first term in the above equation is zero. The formula for the angle of refraction α thus becomes:

$$\alpha = \frac{2d\delta \cos^2 \theta \sin \theta}{\sqrt{R^2 - d^2 \sin^2 \theta}} \quad (5.9)$$

The above formula was used to calculate the angle of refraction also in the case of two overlapping wires. Figure 5.9 shows the CAXPCi setup with two wires and without the coded apertures for clarity's sake. The photon emitted from the source o at an angle θ_1 interacts with the first wire and is refracted at an angle α . The refracted photon is then refracted also by the second wire, at an angle β . A geometrical trick has been used to be able to calculate β still using equation (5.9). The path of the photon after refraction in the first sample is backprojected onto the z-axis. The intersection of the new photon's path and the z-axis creates a new origin o' and the incident angle becomes θ_2 instead of θ_1 with $\theta_2 = \theta_1 + \alpha$ where θ_1 was the original angle at which the photon was emitted, and α the refraction angle caused by the first wire. In this way, equation (5.9) can be re-applied following a simple change of coordinates. The next step involves rotating both wires (i.e. varying their relative position) within limited angular range to simulate the tomosynthesis scan. This step will be described in the next section of this chapter.

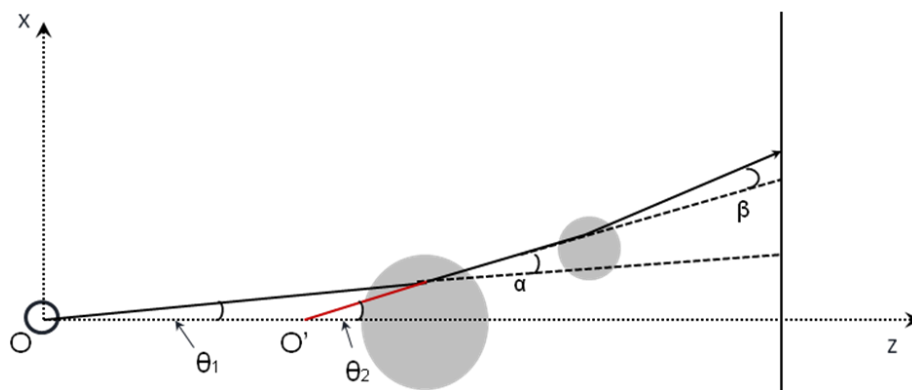


Figure 5.9 Schematic of the mechanism used to calculate the refraction angles caused by two wires overlapping in the x-direction.

The results of the simulated data in a planar geometry were compared with those obtained through another simulator created on the basis of an open source x-ray ray tracing program, McXtrace (Knudsen et al. 2011), which has been developed from a neutron ray tracing program called McStas. McXtrace is a Monte Carlo model and differs from the one previously described as refraction is calculated using a vector form of the Snell's Law. The refraction angle is calculated at the photons entrance and exit points from the wire, with absorption then included by inserting the distance between the entrance and exit point into the Beer's formula. The code describing a single wire is automatically embedded in the McXtrace simulation as a generic object with a circular cross-section. A modular structure like that provided by the McXtrace allows including any number of wires in the simulation, without having to modify the code. McXtrace also features all other components needed to model the system, including a component which can be used to include aperture masks. In this sense this approach is advantageous as it allows modelling more complicated sample geometries in 3D, since the calculation of the refraction angle only requires the surface normal at the interaction point to be known.

5.3.1.2 Experimental conditions

For the experimental validation of the model, a set of four planar images was acquired using the tomosynthesis setup, with sample orientations corresponding to separated wires, wires with one edge overlapping, wires completely overlapping and wires with the other edge overlapping - with diameters of 470 μm and 210 μm . The wires were made from Polyether ether ketone (PEEK). The refractive index of the wires at an effective energy of 18 keV was used as input to the simulations, with the unit decrement

of the real part equal to 8.0×10^{-7} and the imaginary part equal to $3.3 \cdot 10^{-10}$. The two samples had an approximate source to sample distance of 1.64m and 1.66m, respectively. Image acquisition was controlled by data acquisition software written in IDL (Interactive Data Language, ITT Visual Information Solutions, Boulder, CO, USA).

5.3.1.3 Results and discussion

The results of planar simulations with both models and the experimental data are shown in Figure 5.10. The experimental data shows good agreement with the results obtained with both models. The signal spill-out in the detector given in input to the simulation was 5%, as was measured experimentally. Occasionally there are minor differences in the maximum peak height, which can be explained by signal sampling. Apart from this, the agreement between simulated and experimental data is satisfactory.

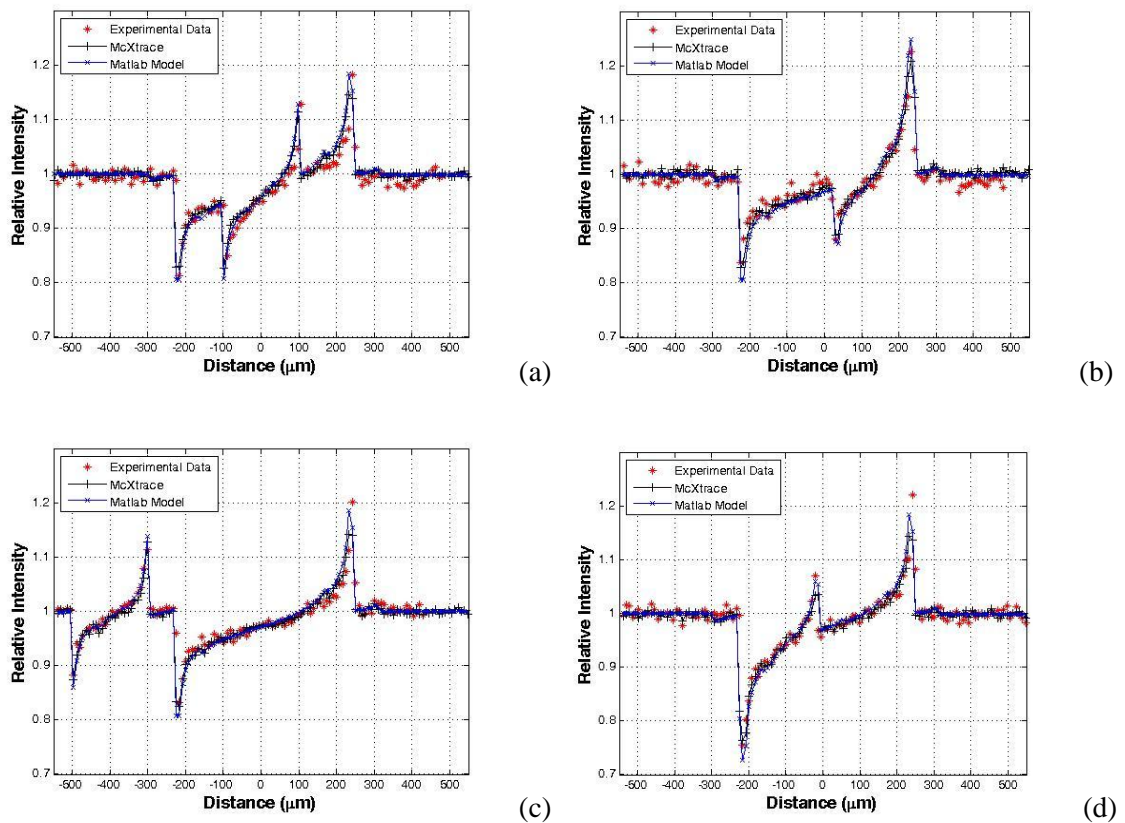


Figure 5.10 Simulated phase contrast signals of two wires in four different relative positions: the wires overlap (a), the wires are completely separated on the x axis (c) and the wires are in intermediate positions (b) and (d)

5.3.2 Tomosynthesis simulations

5.3.2.1 Description of the simulations

Following validation of the planar model the two overlapping wires, simulated and experimental data were collected for a whole tomosynthesis scan, and reconstructions were performed. After verification that the two models produced the same results, only one of the models was used to simulate the full tomosynthesis scan, i.e. the modified version of the simulator presented in (Olivo and Speller 2007). The Tomosynthesis simulations involved rotation of the two wires within a limited angular range around the centre of rotation located between the samples, as shown in Figure 5.11. The angle of refraction at each angular step depends on the relative positions of the wires, i.e. on the rotation angle and the actual source-to-sample distance.

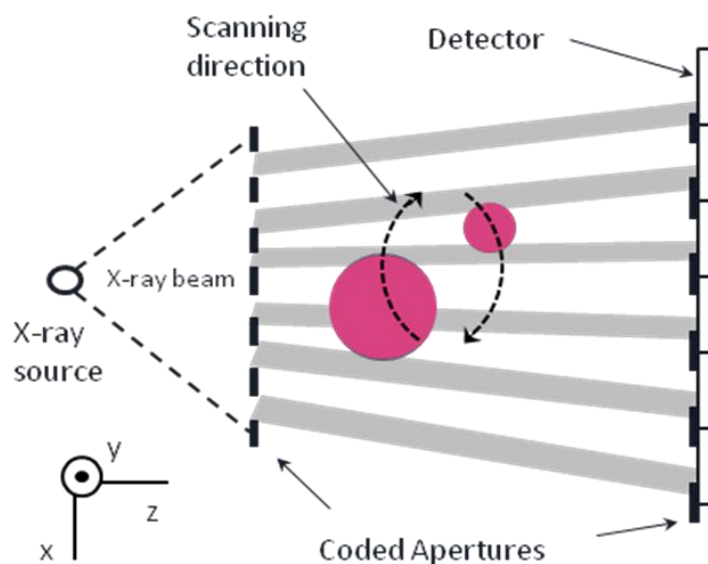


Figure 5.11 Schematic drawing of the CAXPCi setup for TS simulations and experiments. Dotted arrows indicate the direction of scanning.

Figure 5.12 shows a selection of the simulated single tomosynthesis projections of the PEEK wires at several acquisition angles. The total angular range was chosen so that the two wires always overlapped in all projection images (i.e. such that the individual wires were never “seen” separately).

5.3.2.2 Experimental validation

The tomosynthesis acquisition and reconstruction allow for the separation of wires which fully overlap in all planar images. Images obtained experimentally were

reconstructed with the Dexela's software, which uses the SPS algorithm described previously in chapter 2. Figure 5.13 shows the reconstructed images and the corresponding profiles obtained in the simulations and in the experiments, respectively.

A good agreement was found between the reconstructed simulated profiles and those obtained from the experiment in both cases showing good separation of the thin weakly absorbing wires. The calculated contrast values of the reconstructed thick wire were 2.1 and 1.1 in simulations and experiment, respectively. The contrast of the thin wire resulted in 1.3 and 0.7 for the simulation and the experiment, respectively. The results of the simulations indicate that a great improvement in image contrast is possible due to the phase contrast effects. The contrast calculated from the experimental profiles is different to the one obtained with the simulations due to the sparse sampling of the signal, plus possibly the fact that no noise was added to the simulations.

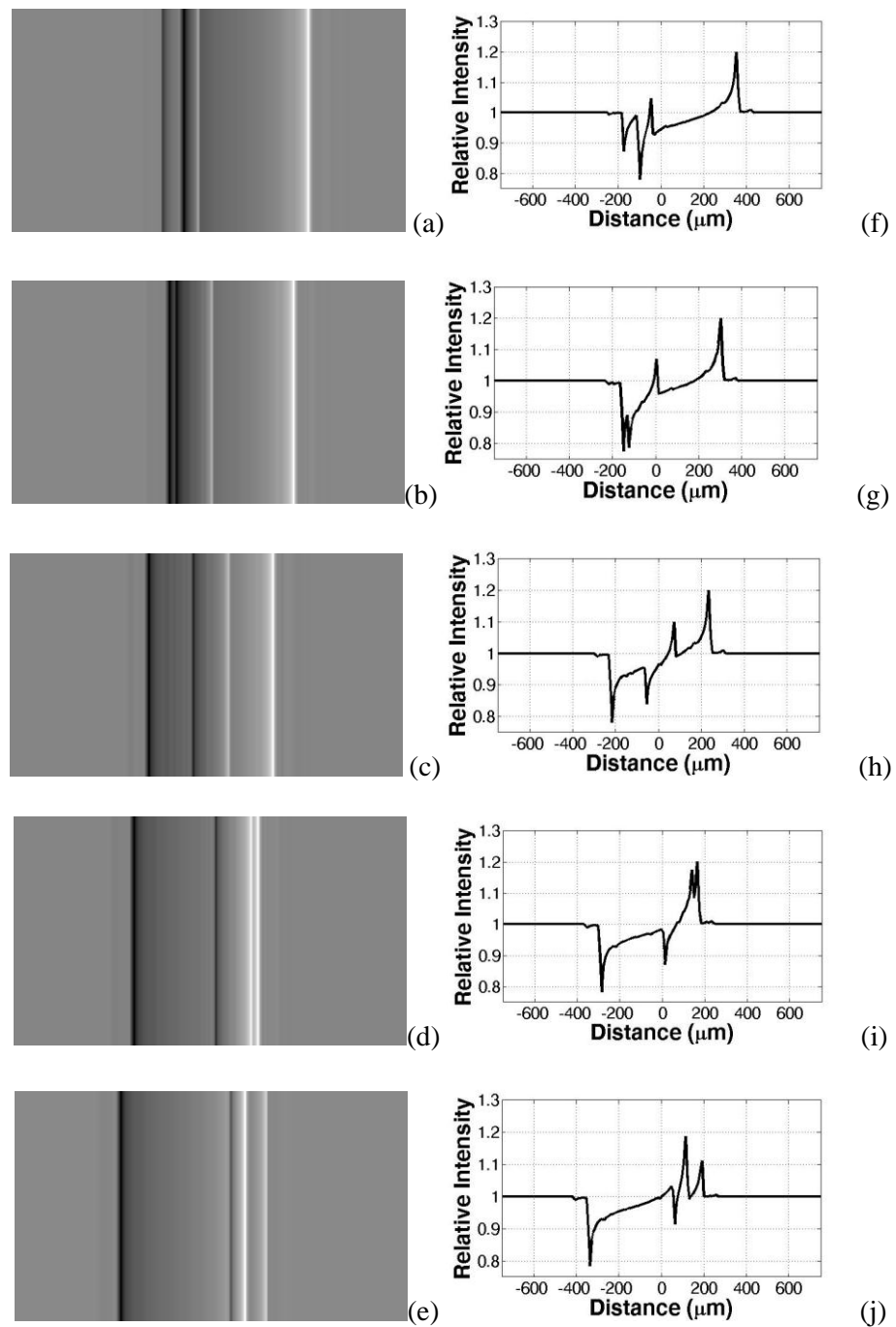


Figure 5.12 Simulated phase contrast tomography projections (a-e) of the wires and the corresponding profiles (f-j)

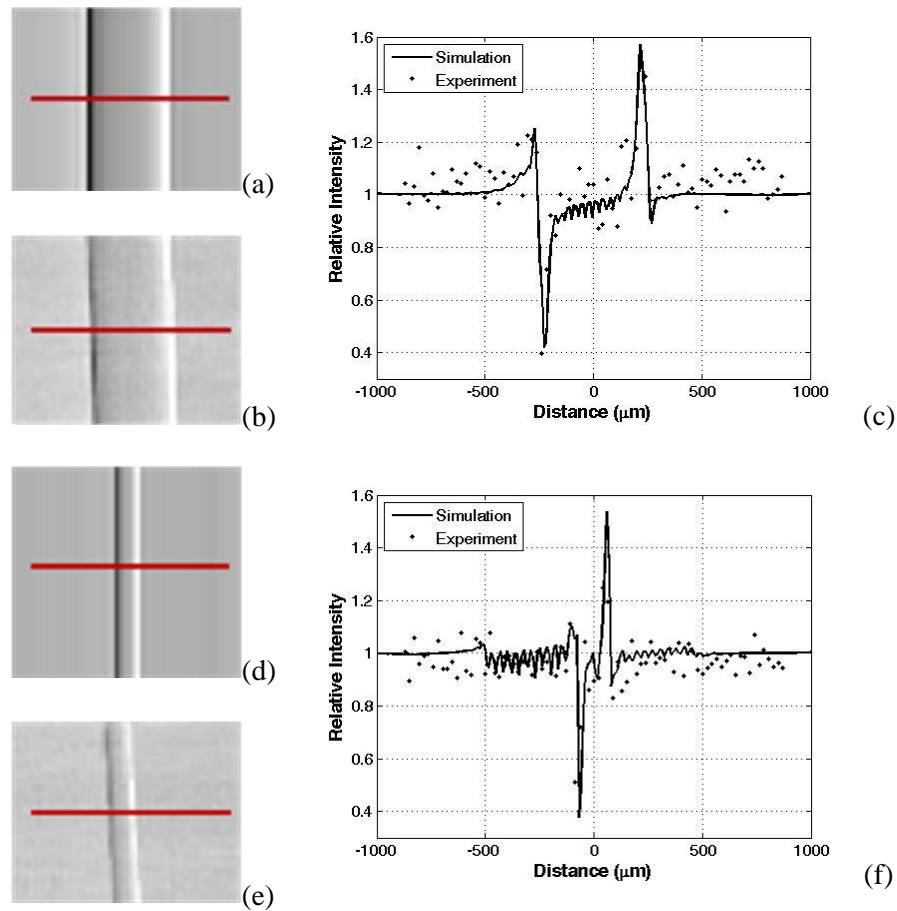


Figure 5.13 Reconstructed simulated (a) and experimental (b) images of the large wire, and corresponding profiles (c); reconstructed simulated (d) and experimental (e) images of the thin wire, and corresponding profiles (f).

5.4 Coded Apertures Phase Contrast Tomosynthesis

5.4.1 CAXPC Tomosynthesis of a “double” TORMAM phantom

The next step of the validation of the proposed method consisted in performing a CAPCTS acquisition of a more realistic sample. Two overlapping mammographic TORMAM phantoms (since now referred to as “double” TORMAM phantom) were used for this purpose. The phantom contains six groups of multidirectional filaments, six groups of micro calcifications and six groups of low contrast detail disks to simulate filaments, micro calcifications and tumour masses, respectively. Two phantoms were horizontally shifted with respect to each other, so that different features overlapped. A region of interest (ROI) of 6 cm by 6 cm in the phantom was chosen for the experiments

(see Figure 5.14). Two experiments were carried out with this “double” TORMAM phantom. In the first one, the sample was rotated within an angular range of 15° in 1° steps with a total exposure time of 105 seconds. In the second experiment, the same acquisition was carried out as previously, except that, for each individual tomosynthesis projection, i.e. at each angle, the sample was scanned in four steps across the masks (“dithering”) for finer sampling of the phase contrast profiles resulting in a stronger phase signal, but at a cost of a longer acquisition (21 minutes). The mean glandular dose delivered to the 33mm thick phantom in a single projection was estimated for a 50% glandular and 50% adipose tissue to be 0.26 mGy with the ESAK of 0.76 mGy. The MGD of 3.86 mGy for the tomosynthesis scan was calculated as a sum of the MGD in 15 projections with an assumption that each projection had the same dose.

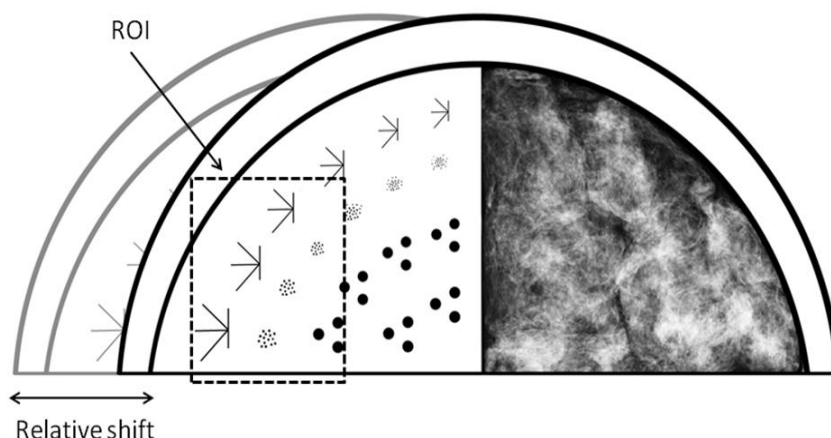


Figure 5.14 TORMAM phantom with an ROI selected for experiments

Figure 5.15 shows vertical slices through the reconstructed tomosynthesis scan of the “double” TORMAM phantom and a single projection from the same scan. The features belonging to the two superimposed TORMAM phantoms which overlap in a single projection image (disks and fibres, Figure 5.15a) are clearly separated by the tomosynthesis reconstruction (Figure 5.15b and c). The phase contrast enhancement visible in the planar image (bright and dark fringes at the edge of the objects) can also be seen in the reconstructed tomosynthesis slices, even though a conventional reconstruction algorithm was used. This demonstrates preservation of the phase-induced image enhancement also following tomosynthesis acquisition and reconstruction, which was the main aim of this work.

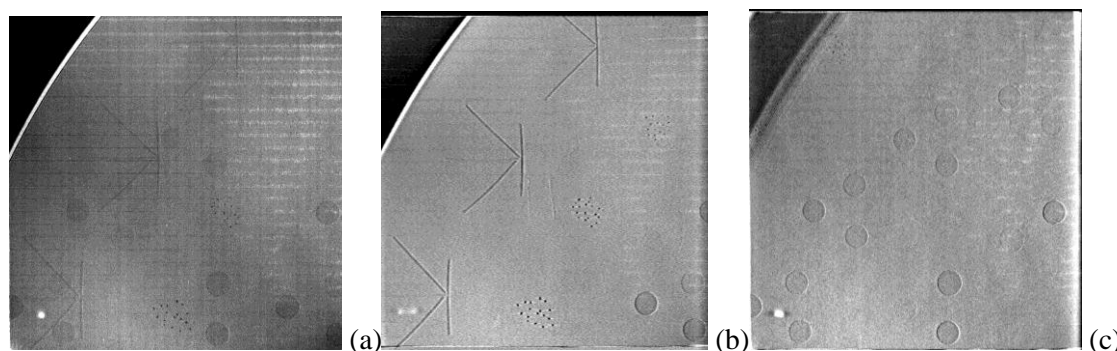


Figure 5.15 Single projection image and two reconstructed slices of the sample built of two TOMAM phantoms ((a), (b), (c), respectively). The visible horizontal lines are due to defects in the masks.

Figure 5.16 shows a single projection image and two reconstructed planes from the same tomosynthesis scan of a ROI of the “double” TOMAM phantom. This ROI features three multi-directional filaments above three low contrast disks. The phase contrast signal (see positive and negative peaks in of Figure 5.16f) is clearly visible at the edges of the objects in the projection images, despite the relatively high noise (due to the fact that this is a single frame of the tomosynthesis scan).

The reconstructed planes from the “dithered” images (see above) are shown in Figure 5.16b and c. The corresponding profile plots (Figure 5.16g and h) show that the phase contrast signal from the two overlapping structures can be effectively separated. This “dithered” acquisition was performed to highlight the preserved visibility of the edge-enhancement effects in the reconstructed image. This requires an increase in the exposure time, with regards to a non-dithered image, equal to the number of dithering steps (4 in this case).

Phase contrast effects, however, are also visible in the non-dithered reconstructions. This has been observed previously with a different application of the method (Olivo et al. 2011). Figure 5.16d and e show images reconstructed from a scan where no dithering was applied, and in which only one frame per angle was taken to minimize the exposure time, which in this case was less than 2 minutes, and Figure 5.16i and j contain the corresponding profiles.

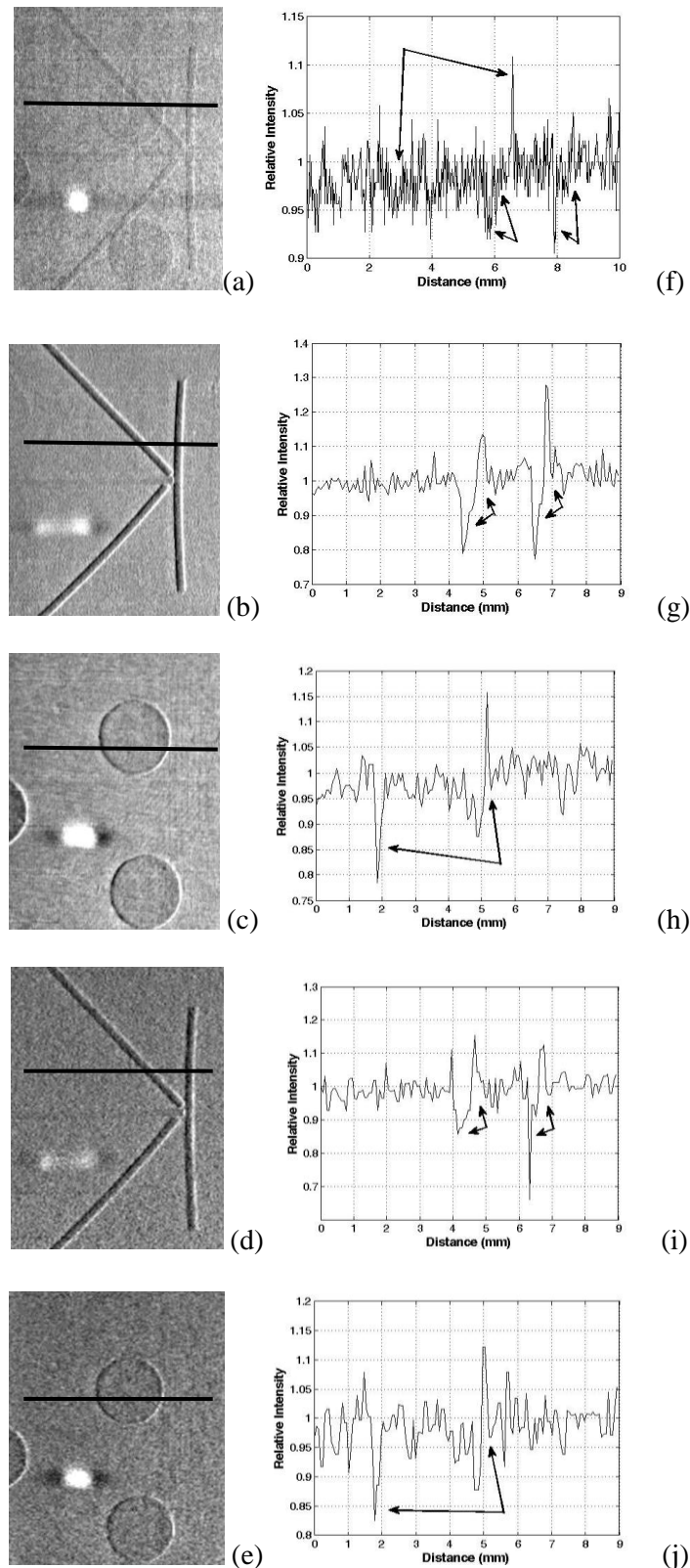


Figure 5.16 Single projection extracted from the tomosynthesis scan (a) and tomosynthesis reconstructions (b - e), and the corresponding profile plots (f - j) of an ROI of the double TORMAM phantom. (b) and (c) are reconstructed slices from “dithered” projections, while (d) and (e) are the reconstructed slices from a single frame with no dithering. The arrows in the profile plots indicate the peaks of the phase contrast signal at the edges of the details. The white spot visible in the planar image is due to a defect in one of the masks. This is blurred in the reconstructions.

5.4.2 Results of the clinical Tomosynthesis of the “double” TORMAM phantom

A Tomosynthesis scan of the “double” TORMAM phantom was also obtained with a commercial system (Giotto, IMS Italy). The details of this system are given in the previous chapter. The sample was placed at a distance of 674mm from the source. This is the typical distance from the source to the carbon fibre plate of the detector, upon which the breast is positioned in a clinical scan. The axis of rotation is about 26mm above the surface of the detector. An angular range of 40° was used for the acquisition of a total of 13 projections. Also in this case, images were reconstructed with the Dexela SPS algorithm. Note that this reconstruction method is different than that actually used in the commercial system. Ten iterations were performed and the z-resolution was set to 1mm.

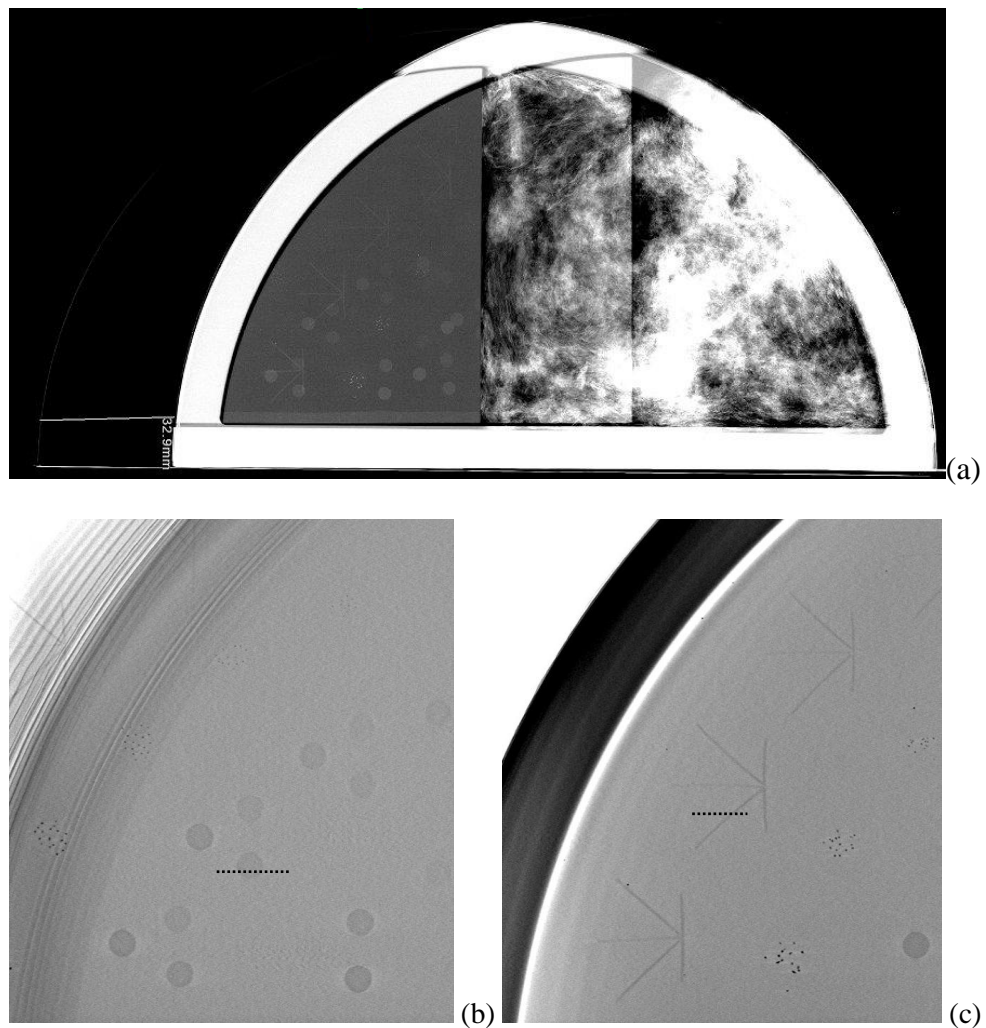


Figure 5.17 Mammography image obtained with IMS system (a) and two reconstructed tomosynthesis slices (b) and (c) of the sample built of two TORMAM phantoms

Two reconstructed images showing a slice from each of the two superimposed TORMAM phantoms are presented in Figure 5.17 (as previously done for the CAXPCi TS scans, see figures Figure 5.15 and Figure 5.16). Note that there is no phase contrast signal present in the images, as these were obtained with a conventional tomosynthesis system based on absorption. Figure 5.18 shows a profile plot measured along the dotted lines shown in Figure 5.17. The image contrast calculated as a difference of the intensity of the object and the background is 14% and 8% for the disk and fibre, respectively.

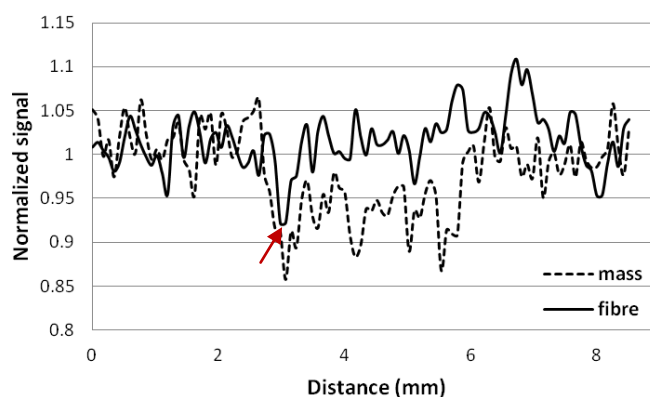


Figure 5.18 Experimental clinical profiles of a mass and a fibre taken along the lines in Figure 5.17. The arrow indicates the position of the fibre.

5.5 Summary and discussion

The work shown in this chapter presents proof-of-concept results on the implementation of CAXPCi based Tomosynthesis. First, the system setup and the dose measurements were described. Second, results were shown for the modelling of the phase contrast signal in tomosynthesis geometry, alongside their experimental validation, through a simple, geometric “double wire” phantom. Finally, the results of tomosynthesis imaging of a more complex “double” TORMAM phantom were included. It was demonstrated that strong edge-enhancement effects due to phase contrast are maintained in the reconstructed tomosynthesis slices, also following full separation of the overlapping structures.

An advantage of using the proposed technique is the relatively short exposure time required to collect full phase contrast tomosynthesis scans compared to other lab based x-ray phase contrast techniques. It should be noted, for example, that our already relatively short exposure time of 105 seconds for the non-dithered TORMAM phantom

acquisition has the potential to be reduced further. A shorter exposure time of 3 seconds instead of 7 seconds could be used with the Anrad SMAM detector used in this study, although this would possibly compromise the image quality. Alternatively, one could use the Anrad LMAM detector designed specifically for tomosynthesis, which provides 1 to 2 frames per second instead of 1 frame every 7 seconds. In order to reduce the total acquisition time, fewer projection angles could be used. The fine adjustment of these parameters will be the subject of future work.

With the proof-of concept set-up used in this case, we already demonstrate dose figures roughly compatible with clinically acceptable levels. However, the sample used in this case had a total thickness slightly lower than a real compressed breast, which would have an effect on the reported dose figures. However, the measures which will be put into place to reduce the exposure time would also have an effect on the dose. This is a delicate balance between dose and image quality, which will require thorough investigations on real breast tissue samples as part of the future work. Moreover, the reduced sensitivity of phase effects to increased x-ray energy could be used to obtain more advantageous dose/image quality balances.

As expected, the sampling of the phase contrast signal in the individual, single projections is of course lower than that of “dithered” projections. However, this is partially solved by the tomosynthesis reconstruction, as the missing signal is partly restored from the differently sampled phase information coming from different angles. This is shown by the undithered images of the TORMAM phantom obtained in 105 s (Figure 5.16d and e), which still show strong phase effects despite the possible undersampling in the individual projections.

For what concerns the modelling part of the work, the results of the two simulations were found to be in a good agreement with the experiments, and gave almost identical results. This “benchmarks” the McXtrace based model against the simpler one developed by Olivo and Speller, which was previously experimentally verified. We expect that the higher flexibility of the former model will allow for the simulation of more complex phantoms to support future developments.

The purpose of this work was to obtain the proof of concept on the viability of Coded-Aperture (or “Edge-Illumination”) Phase Contrast Tomosynthesis. In a first study, the results of two different simulation models of the phase signal from two plastic wires

were verified experimentally, showing that both models can be used to simulate the phase contrast signal. To describe how the phase contrast signal changes with the angle, an extended version of the model developed by Olivo and Speller (Olivo and Speller 2007) for tomosynthesis geometry was used. Two superimposed wires were scanned in the tomosynthesis geometry, and separated by means of an iterative reconstruction algorithm.

In a second study, these results were extended to a thicker sample, made of two superimposed TORMAM phantoms. The phase contrast signal is still clearly visible in the reconstructions, also with no sample dithering and with a single frame per angle. In the latter case, the total acquisition time was just over 1.5 minutes with the current set-up. Simple improvements in the detector technology (e.g. use of the Anrad LMAM which can acquire 2 frames per second) could already reduce this acquisition time.

As demonstrated by both studies, the new approach effectively combines phase contrast enhancement and 3D information, leading to higher detail detectability than conventional absorption based Tomosynthesis. The “coded-aperture” method allows the exploitation of phase effects outside synchrotrons, and shows promise for translation into a clinical environment: for example, the system used in this experiment was completely built using off-the-shelf equipment. Although in this case the sample was rotated for simplicity’s sake, it should be noted that a commercial system would only require a lateral displacement of the pre-sample mask, synchronized with the source angular movement at each frame. It has shown previously that a tolerance of a few microns would be sufficient for this movement (Olivo et al. 2011), which is well within reach of current technology. The detector mask is fixed at the centre of the detector pixels, and in a commercial device it could be directly laminated onto the detector surface.

Chapter 6

6 Comparison between different reconstruction algorithms

6.1 Introduction

A Tomosynthesis dataset is highly incomplete due to the limited number of projection angles at which data are acquired. As a consequence, no exact analytic solution exists for a quantitative image reconstruction. However, it has been shown (Wu et al. 2004) that iterative methods provide “visually” improved images compared to those obtained with non-iterative techniques.

The purpose of this chapter is to compare reconstruction methods that have been proposed for the conventional absorption-based tomosynthesis reconstruction on images acquired with the CAXPC based tomosynthesis method. Three reconstruction algorithms were evaluated: FBP (implemented with an *iradon* function in Matlab, R2010b), SPS (Dexela Ltd.) and CG (UCL Toolkit, CMIC, UCL London, (Yang et al. 2010)). The comparison is based on two overlapping mammographic TORMAM phantoms imaged under the conditions described in the previous chapter. The comparison was focused on the same ROI as discussed before, containing two features mimicking clinical relevance: a disk representing a tumour mass and a set of multidimensional fibres. Obviously, the two features overlapped in the individual projections. Figure 6.1 shows the reconstructed structures within planes at $z=7\text{mm}$ (left) and $z=24\text{mm}$ (right) reconstructed with the FBP (a, b), SPS (c, d) and CG (e, f) algorithms. It is immediately obvious that the amount of phase contrast signal is different in all three reconstructions. To describe this difference quantitatively, a contrast to noise ratio (CNR) parameters can be calculated. Further, due to the high data incompleteness typical of tomosynthesis, all reconstructed images contain artefacts, such as ghosting artefacts created by out of plane objects. These artefacts are obvious in all three reconstructions, but are most

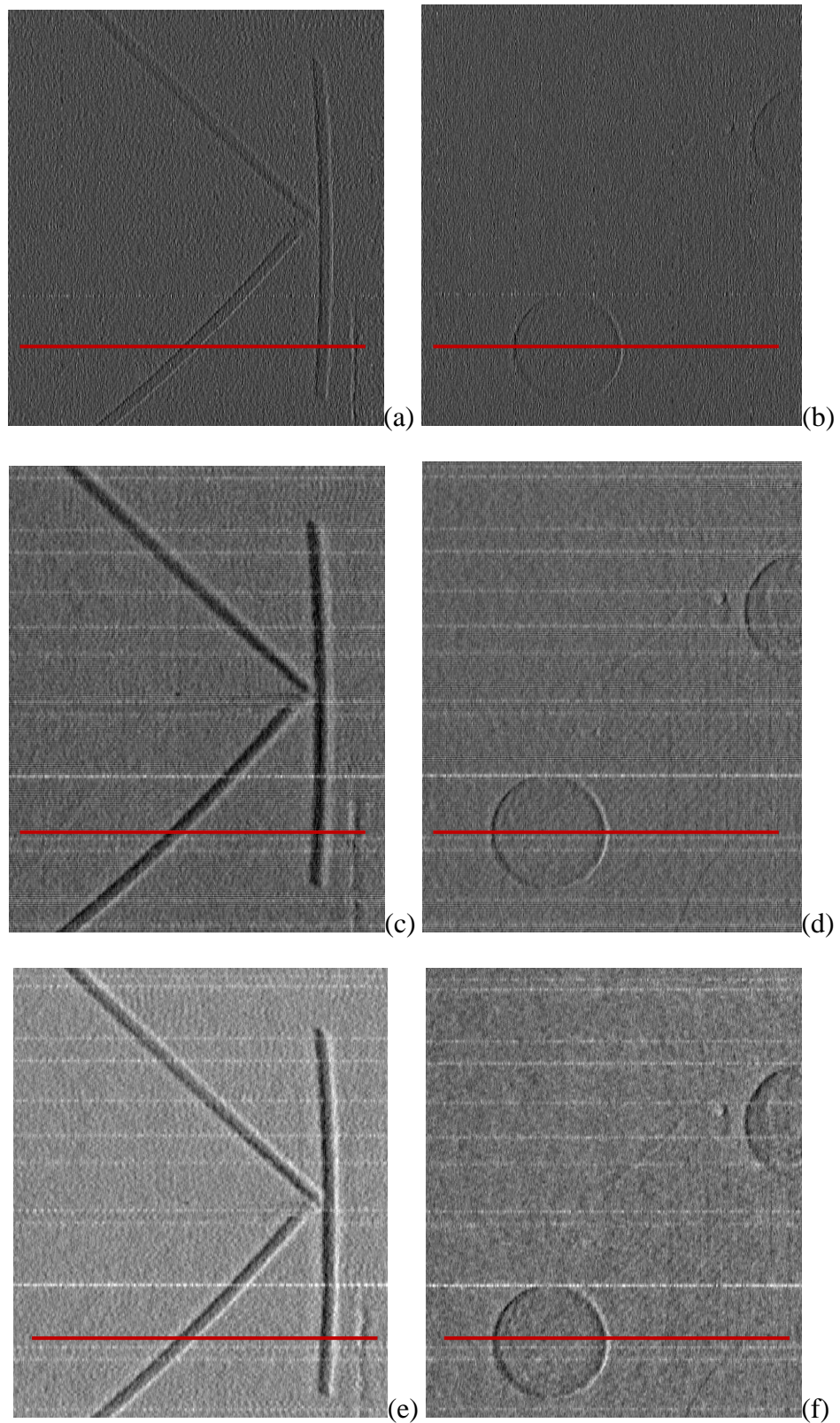


Figure 6.1 Tomosynthesis reconstructions of a ROI of the “double” TORMAM phantom performed with FBP (a, b), CG (c, d) and SPS (e, f) algorithms. The white horizontal lines are defects in the masks, and are thus not included in the evaluation of the reconstruction-induced image artefacts (see definition of ASF).

severe in the FBP case. These artefacts are usually quantified by means of an artefact spread function (ASF).

Figure 6.2 shows the image profiles through individual details in the reconstructed images in Figure 6.1. The value of the mean intensity in the background was taken on both sides of the phase contrast peaks, without including the details. As it can be seen, the noise is highest in the FBP reconstruction. This is expected, as the ramp filter used in this reconstruction tends to amplify the noise. It can be also seen that the phase contrast peaks in the reconstructed plots are smoothed in both iterative methods compared to the FBP one. The main reason for this is the regularization process in the iterative reconstructions. In the SPS method, the regularization process involves adding the penalty function, which takes into account the prior information about the object and favours reconstructed images that are piecewise smooth. If the regularization coefficient β is large, image noise is reduced at the price of a reduced spatial resolution (Sonka 2009)). In this way a low probability is assigned to the images that contain fine details, as these are considered to be likely to be due to noise (Miles N. Wernick 2004). The phase contrast images are not piecewise smooth as they contain positive and negative peaks, which, for small objects, can be only a few pixels apart. These peaks may be mistaken for noise in the iterative reconstruction. Moreover, in the SPS algorithm, a “voting strategy” (Wu et al. 2006) is used to remove ghosting artefacts caused by high absorbing objects in the projections. A technique similar to the projection segmentation method described in (Wu et al. 2006) is used. The basic idea is to analyze contributions to a given voxel coming from all projections and find the “abnormal” ones. The projections whose contribution is considered “abnormal”, are then excluded from the reconstruction. Usually, high-attenuation features are detected with an edge detection method, and a map is created for each projection. Next, if the contribution from a given projection to a reconstruction voxel contains high-attenuation values, then this projection is not used. However, if all the projections contain similar high-attenuation values, then the voxel is reconstructed from all projections, under the assumption that it really does contain information about a high-attenuating feature. In the phase contrast projections, the high frequency signal, which appears at the boundaries of the objects, can be easily mistaken for signal from high-attenuating features. Furthermore, the intensity of this refraction signal may be different in each projection, i.e. there may not

be an even contribution from all the projections to a given voxel. This eventually causes smoothing out of the high frequency peaks in the reconstructed images.

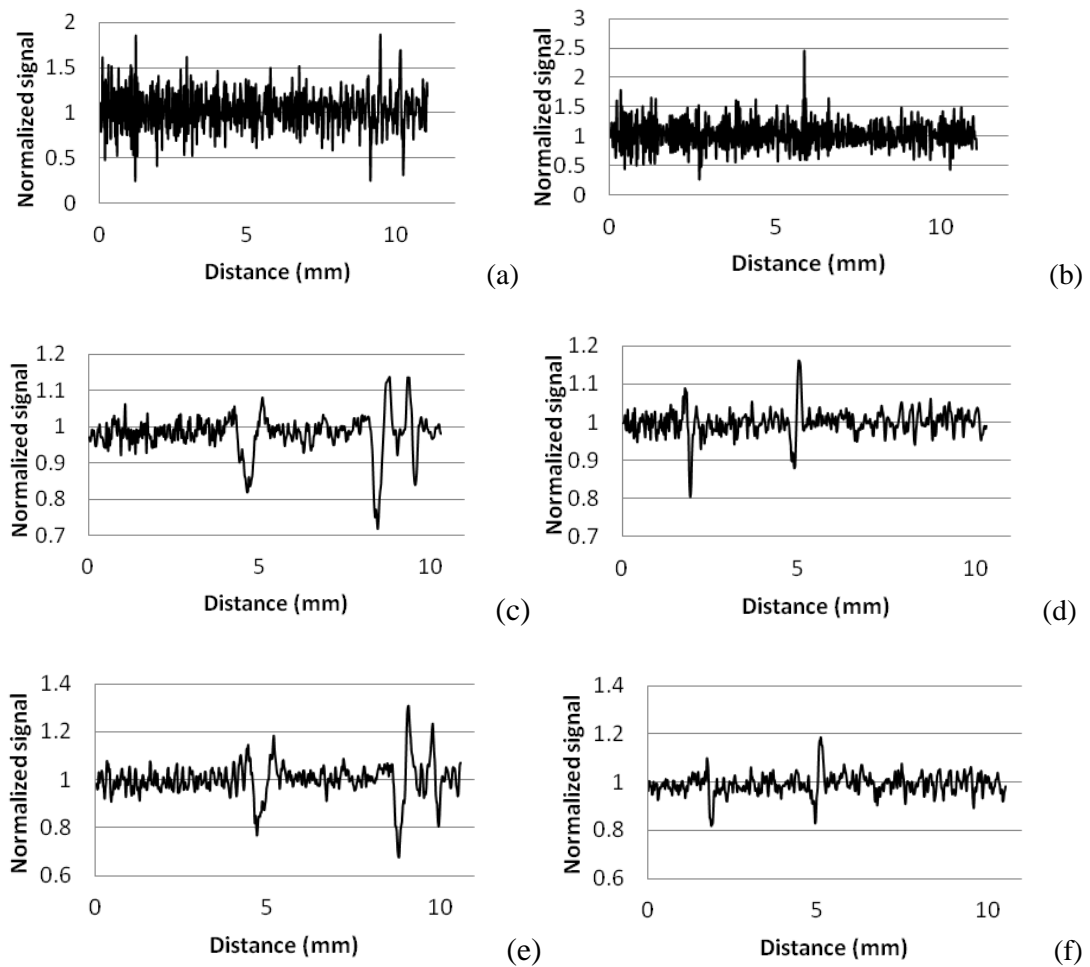


Figure 6.2 Profile plots extracted from the tomosynthesis reconstructions along the red lines in Figure 6.1 obtained with the FBP (a, b), CG (c, d) and SPS (e, f) algorithms. Note that the scale on the y-axis is substantially different for the analytical (FBP) and the iterative (CG and SPS) methods.

6.2 Quantitative comparison between FBP, CG and SPS algorithms

6.2.1 CNR

The in-plane image quality was evaluated by two parameters: image contrast and contrast-to-noise ratio, defined previously in chapter 2. The image contrast is a measure of the relative intensity of the signal created by an object in a reconstructed plane, while the CNR takes into account also the background noise and is directly linked to detail visibility. Figure 6.3 shows the difference in image contrast (left) and CNR (right) for

two details (the tumour mass and fibre), and for the three reconstruction algorithms evaluated. The results show that the contrast is much higher for the FBP method than for both the SPS and CG methods. The results of CNR, however, are similar for the SPS and CG methods, being 12.6 and 15 for the mass and 12.9 and 10.1 for the fibre, respectively. On the contrary, FBP gives lower CNR values: 5.4 and 10.5 for the mass and fibre, respectively. Hence, the contrast is much higher for the analytical method than for the iterative ones; as previously mentioned, this can be due to the way in which iterative methods aim at reducing the noise, which the phase contrast signal could be mistaken for. However, if one also takes into account the noise appearing in the reconstructions, then it can be seen that the iterative methods are ultimately “preferable” as the CNR is higher.

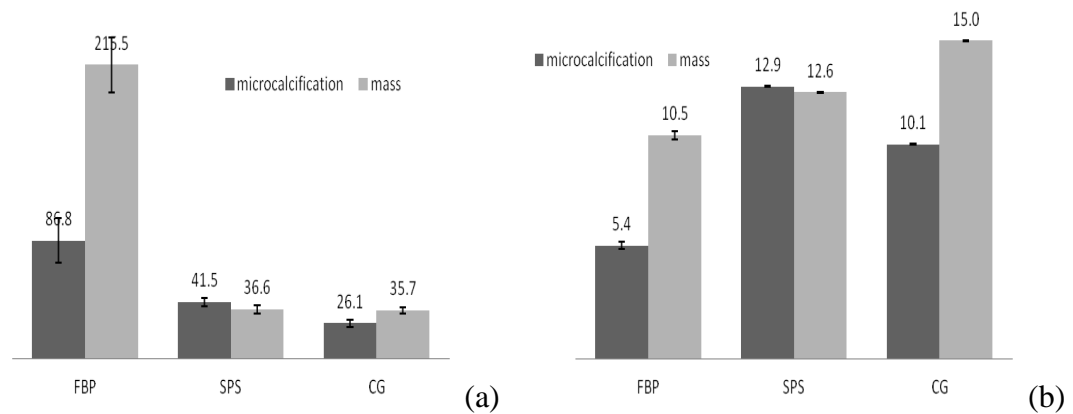


Figure 6.3 Contrast shown in % (a) and CNR (b) calculated for the fibre and mass object obtained with the three evaluated reconstruction methods: FBP, SPS and CG.

6.2.2 ASF

An example of the ghosting artefact and the results of the ASF calculations for the tumour mass measured from the reconstructions obtained with the three evaluated methods are presented in Figure 6.4. The chart shows the ASF as a function of distance from the in-focus plane, which is indicated as the zero position. For each reconstruction method, the in-focus slice was chosen as the one with highest phase contrast signal. The results show that: the tails of the ASF of the two iterative algorithms are close together, and drop down smoothly with increasing distance from the plane-in-focus, while the tail of the FBP becomes noisier for a distance larger than 1mm from the in-focus plane. Both iterative methods remove the ghosting artefacts equally well. In the analytical method, no further improvement was seen above 1mm distance from the plane in focus.

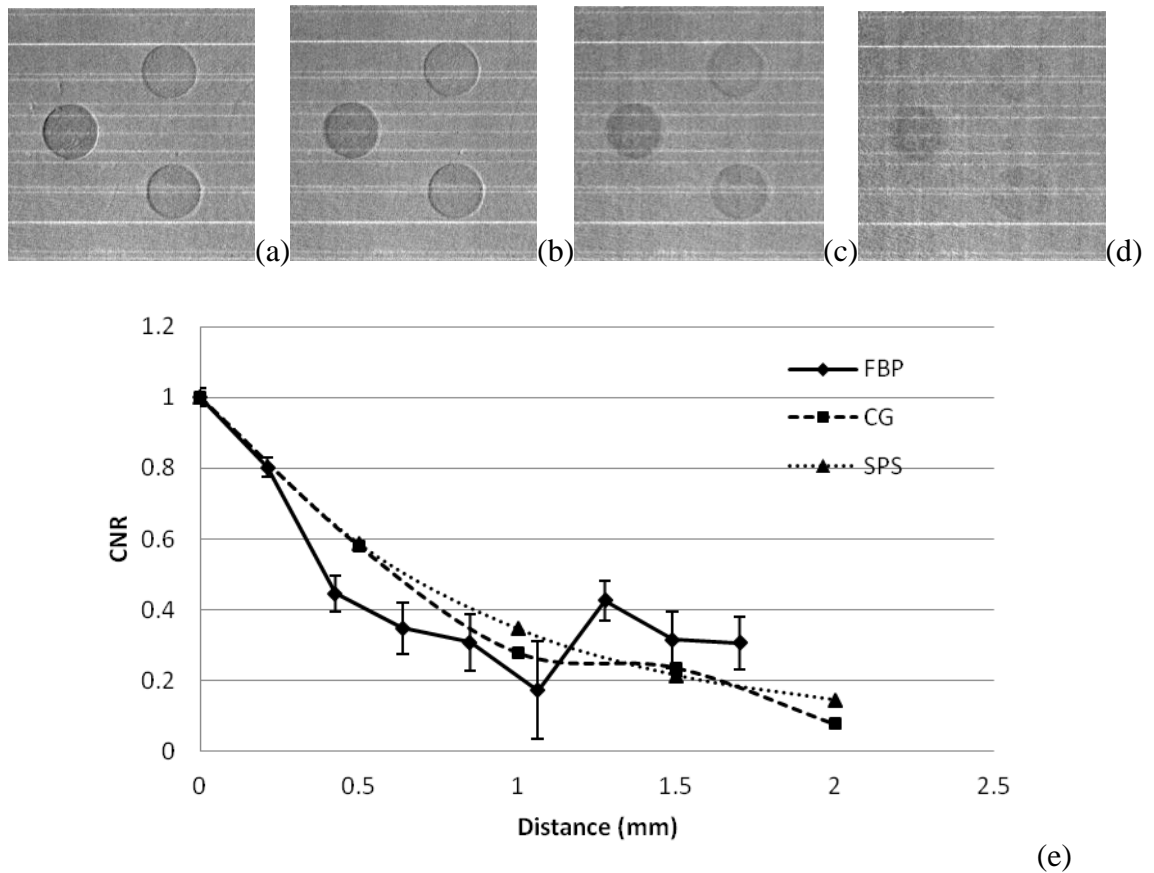


Figure 6.4 Example of a ghosting artefact of the tumour-like object (a-d) and an artefact spread function (ASF) versus distance from the in-focus plane of a tumour-like object measured from FBP, CG and SPS reconstructions

6.2.3 Regularization study

In the two iterative algorithms used in this study (SPS and regularized CG), a Huber function was chosen as the penalty function. The weight of this function is controlled by the parameter β . Figure 6.5 shows the contrast and the CNR values in the reconstructed slices as a function of parameter β for the regularized CG and the SPS algorithms. The results show that the higher the amount of regularization applied, the lower the contrast and the CNR.

The major issue with the Huber function reported in the literature (Mumcuoglu et al. 1996; Yu and Fessler 2002) is the correct choice of the parameter ε . As mentioned previously in chapter 2, this parameter is a scale applied to the potential function of the Huber penalty. In this study, different values in the range of from 0 to 1.5 were tested for the regularized CG algorithm. Figure 6.6 shows the contrast and the CNR values in the reconstructed slices as a function of parameter ε . In this case, β is set to 1. The best

contrast is achieved for ε equal 0, i.e. for the Huber function approaching a quadratic function. However, in this case the CNR is at its lowest, while it improves with increasing the ε until it reaches a plateau at $\varepsilon = 1$. These results are important for phase contrast imaging, as they show that the phase contrast peaks are dramatically smoothed by the regularization procedure of the “standard” iterative methods designed for the conventional absorption signal. This leads to a significant drop in both the contrast and the CNR. This does not mean, however, that the regularization process is not required in the reconstruction of images containing phase contrast information. On the contrary, the regularization would improve both contrast and the CNR of the phase contrast images, if priors were added taking into account the effects of the edge enhancement in addition to those already existing for the absorption-based imaging. Further studies need to be performed to take this into account.

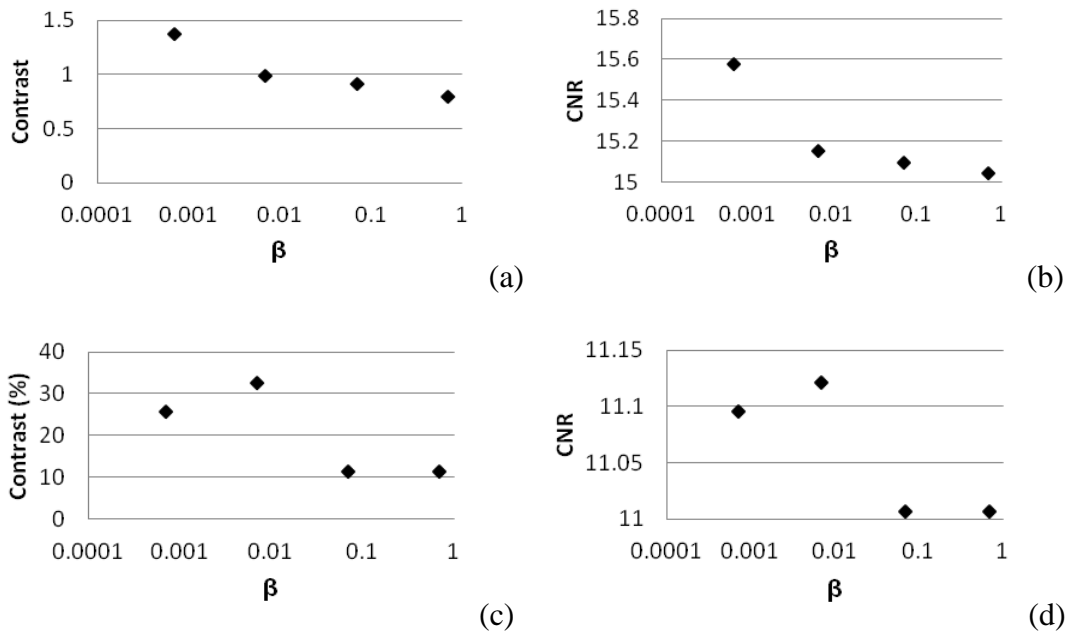


Figure 6.5 Contrast (a, c) and CNR (b, d) as a function of parameter β calculated from regularized CG (a, b) and SPS (c, d) algorithms

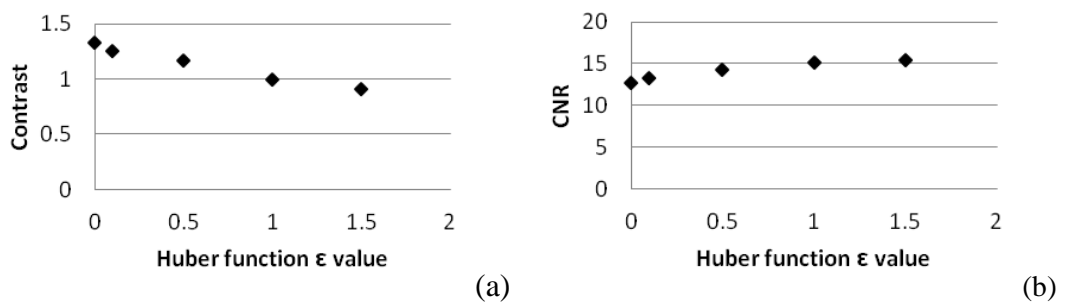


Figure 6.6 Contrast (a) and CNR (b) as a function of parameter ε of the Huber function

6.2.4 Number of iterations

The estimation of the number of iterations leading to optimized image quality is an important step in the reconstruction process. In this work, the SPS reconstruction algorithm was used for this evaluation. The CNR was calculated as a function of the iteration number for one fibre. The result is shown in Figure 6.7. The CNR increases reaching a maximum at 4 iterations, and then drops slowly as more iterations are performed. A similar trend was found for the tumour mass. The optimal number of iterations in the SPS method was therefore assumed to be 4. Successive iterations do not provide any further improvement in CNR, but do increase the noise level in the image.

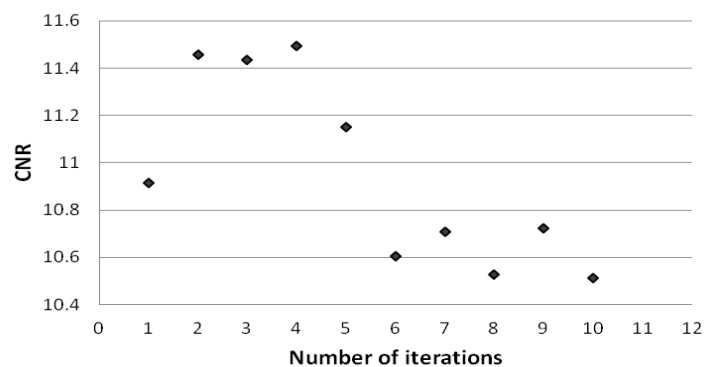


Figure 6.7 CNR as a function of iteration number.

6.3 GPU vs. CPU implementation of the iterative methods

The main limitation of iterative reconstruction methods is that they are much slower than analytical techniques. There have been a number of studies on how to overcome this problem and make iterative reconstructions faster (Jang et al. 2009; Schweiger 2011). In recent years, due to a fast developing gaming industry, graphical processing units (GPUs) are available at reasonable prices. Although originally designed to render 3D graphics scenes, GPUs can also be used for other tasks requiring high parallel processing power. This is for example possible with a *Compute Unified Device Architecture* (CUDA) from Nvidia, which is a parallel computing architecture. It enables calculations on GPU using programming languages like C, Matlab, IDL and others.

In this work, the already discussed implementation of the penalized CG algorithm was tested on both a CPU and a GPU. The workstation was equipped with a processor Intel

(R) Core (TM) i7 and a RAM memory of 16GB. Nvidia Tesla C2050 with 448 cores was used for parallel processing. Since at the time this comparison was performed no phase contrast data was available yet, a clinical dataset was used instead. 31 tomosynthesis images obtained with the Giotto tomosynthesis system from 12 patients were reconstructed. A set of 13 projections with dimensions of 2816×3584 pixels² was used in each case. Figure 6.8 shows the results of the comparison. An 3-fold gain in reconstruction time was demonstrated, with average reconstruction times of 7 minutes and 2.4 minutes for the CPU and GPU implementations, respectively. A similar increase in speed was also observed for the phase contrast images presented in this work.

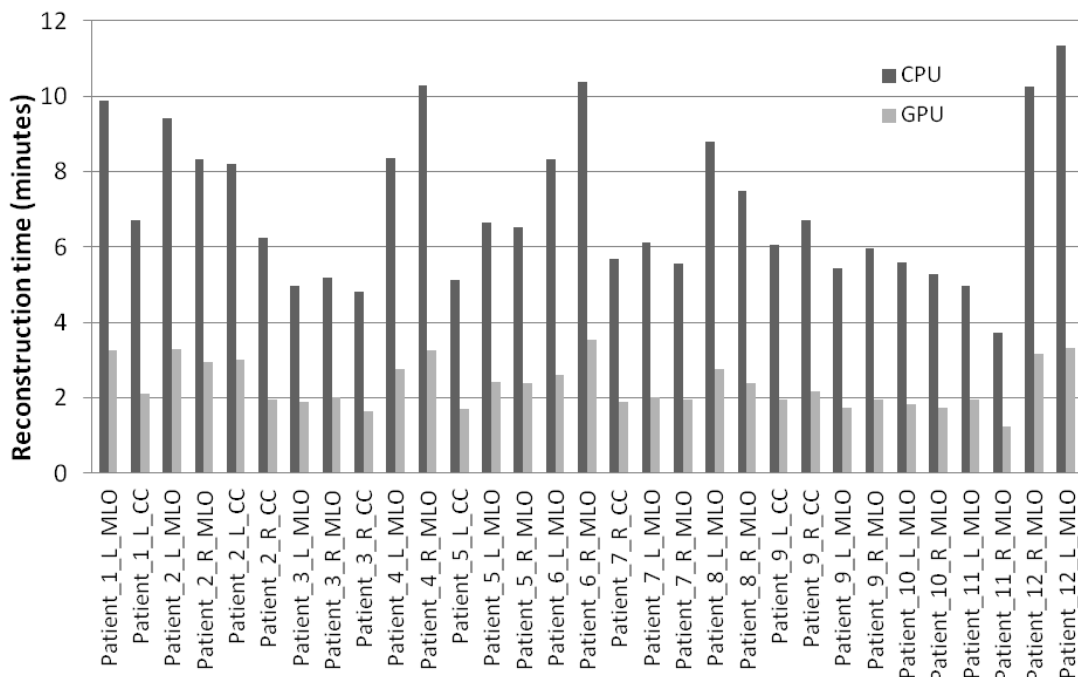


Figure 6.8 Reconstruction time of CPU and GPU implementation of the penalized CG algorithm. Absorption tomosynthesis data was used for this study.

6.4 Optimization of the acquisition geometry

It is known that the acquisition geometry can have a large impact on the reconstructed images obtained with conventional absorption-based tomosynthesis (Mertelmeier et al. 2008; Sechopoulos and Ghetti 2009), and the same can be assumed to apply also to XPCi approaches. There are a number of studies available in the literature, which aim at optimizing the acquisition range and decreasing the radiation dose delivered to the patient (Park et al. 2007; Sechopoulos and Ghetti 2009). Currently, the angular range

varies from 13° to 50° among different tomosynthesis system prototypes. In this work, three different angular sampling schemes (see Figure 6.9) were tested to optimize the acquisition geometry: 15 projections with a 1° angular step (diamonds), 8 projections with 2° angular step (squares), and 11 projections with non-equiangular sampling (triangles). The “double” TOMAM phantom was used for this evaluation.

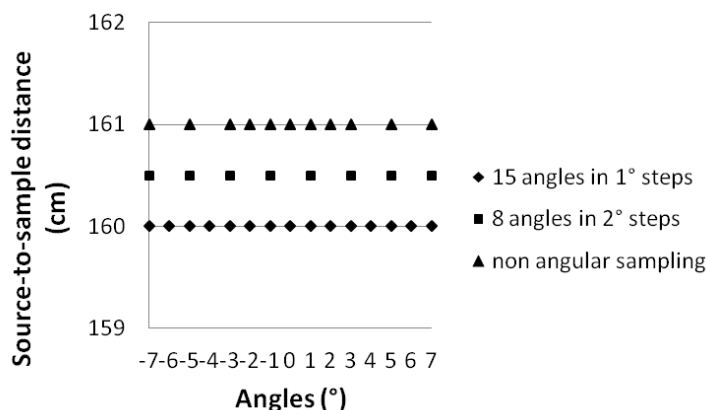


Figure 6.9 Schematic of an angular sampling. 15 angles evenly spread in 1° steps (diamonds), 8 angles evenly spread in 2° steps (squares) and 11 angles with non-equiangular sampling (triangles)

Table 6.1 lists the results of the contrast and the CNR parameters for the three angular sampling schemes tested. It can be seen that the highest CNR for both the fibre and the tumour is obtained with the full angular scanning, i.e. with 15 projections acquired in angular intervals of 1° . The highest contrast, on the other hand, is observed when a non-equiangular range is used. It should also be noted that only a small loss in CNR is observed when the number of projections is reduced from 15 to 11. The acquisition at every second angle (i.e. 8 projections over 15°), instead, results in a much poorer CNR. An additional problem in this case is that the ghosting artefacts interfere with low signal objects, thus severely affecting their visibility.

Table 6.1 Contrast and CNR for fibre and tumour calculated for different angular samplings.

		every angle	every second angle	not equiangular range
fibre	Contrast (%)	24.5 ± 2.1	25.7 ± 3.1	28.4 ± 2.8
	CNR	11.8 ± 2.1	8.3 ± 3.1	10.0 ± 2.8
tumour	Contrast (%)	12.3 ± 1.5	11.2 ± 2.1	12.6 ± 2.8
	CNR	8.4 ± 1.5	5.4 ± 2.1	7.2 ± 2.8

6.5 Optimization of the acquisition geometry

In this chapter the results of a comparison between different reconstruction algorithms were presented. A traditional FBP algorithm and two iterative statistical methods, CG and SPS, were used to reconstruct tomosynthesis phase contrast images of a “double” TORMAM phantom. Contrast and CNR were calculated in the reconstructed slices consisting of two overlapping features: a tumour mass and a fibre. The highest contrast was found for the FBP method, but at the same time the CNR was the lowest, which resulted in very noisy reconstructions. On the contrary, in the case of the iterative methods the CNR was considerably higher but the image contrast was decreased. This can be explained considering that the regularization process in the statistical methods is primarily designed for absorption-based imaging. Generally, the higher the contribution of the regularization factor to the final image, the lower the contrast and the CNR in the phase contrast images. This happens because the regularization smoothes out most of the high frequencies in the image, which are normally considered as noise in the absorption-based image. However, it also suppresses high frequency signals due to real phase contrast effects. Future work will be focused on designing an iterative PC-dedicated reconstruction algorithm.

Three reconstruction methods were also tested for their effectiveness on the removal of ghosting artefacts. It was found that the iterative algorithms were able to eliminate most of the ghosting artefacts with the ASF reaching 10% at a distance of 2 mm from the plane in focus. FBP removes the ghosting artefacts effectively up to a distance of about 0.7mm from the focal plane and with the ASF reaching about 30%. For larger distances no further improvement is achieved.

Next, a study was made on the number of iterations on image quality. This exercise was made with the SPS method and for a signal from a fibre of a double TORMAM phantom. The results showed that the optimal number of iterations was 4. For more iterations, a degradation of the image quality was observed.

Finally, three different angular acquisition schemes were tested for the CAXPCi based tomosynthesis: 15 projections with a 1° angular step, 8 projections with 2° angular step, and 11 projections with non-equiangular sampling. The results show that 15 projections taken with 1° angular steps presented the highest image contrast and CNR. Lowering

the number of projections leads to decreased both the image contrast and CNR. Optimal results were found with the non-equiangular sampling. Although, in this case the image contrast and CNR were lower than for 15 angles, the signal was preserved and the number of projections decreased to 11. This could potentially lead to shorter exposure times and lower dose.

Chapter 7

7 Proposed applications of the developed method

7.1 Mammography

As mentioned many times, phase contrast imaging provides an improved sensitivity compared to absorption-based imaging. Image contrast can be increased by orders of magnitude for light materials, which make this technique highly promising for imaging soft tissues. It should in fact be noted that, although it can be considered an effective and reliable exam, conventional mammography does not allow for an accurate diagnosis in all cases (Tartar et al. 2008). The main limitation comes from the low attenuation differences between healthy and diseased tissues potentially leading to poor image contrast. This means that, in some cases, it can be difficult to distinguish between low absorbing tumour masses and the background tissue. Moreover, small microcalcifications may not be detected due to a limited spatial resolution of the used detection systems. Finally, the superposition of healthy and malignant structures can make the diagnosis more challenging. The results of the first *in vivo* mammographic XPCi clinical trial performed at the SYRMEP beam line (Longo et al. 2007; Castelli et al. 2011) showed that superior sensitivity and specificity can be obtained with phase contrast imaging compared to the conventional absorption-based imaging. CAXPCi could allow transferring this into the laboratory environment. It could thus help with both limitations of conventional mammography, i.e. with the detection of low absorbing tumour masses and with the insufficient spatial resolution required for detection of microcalcifications. Tomosynthesis, on the other hand, removes the problem of overlapping tissues. Here, the new method is tested on the imaging of breast mastectomy tissue samples. An example of this application is shown in Figure 7.1 . Images were obtained with the setup described in chapter 5. The used angular range was

15°, and the projections taken in 1° steps. The sample was dithered along the x-axis of the system so that 4 sample steps were combined in each projection image.

The imaging of soft tissue can be extended to other cases, in which there is need to distinguish between different light materials.

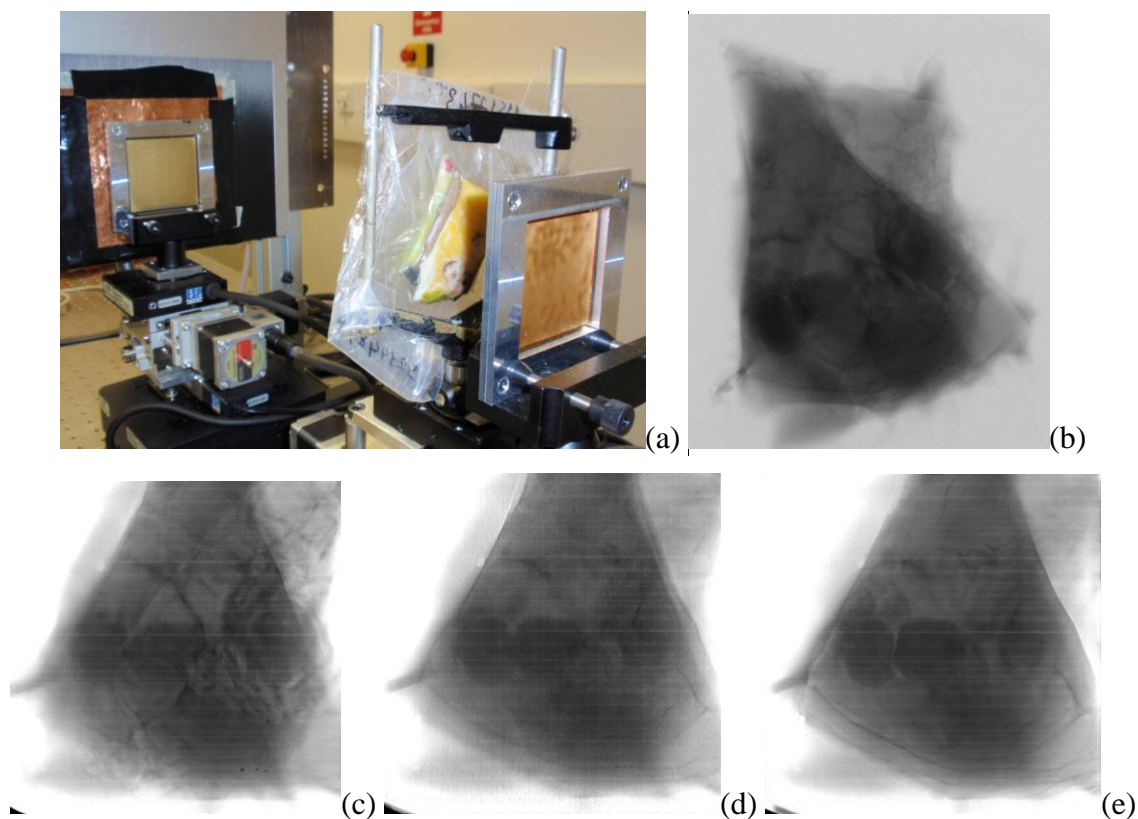


Figure 7.1 Photo of two breast samples stacked together mounted on the imaging system, (a), mammography image of the overlapping samples, (b), and three reconstructed planes (c-e), extracted from each sample (c, e) and one intermediate plane (d).

7.2 Small animal imaging

In a small animal imaging the greatest challenge is to be able to image soft tissues in the presence of high absorbing ones, such as bones. This is because the range of absorption values between soft tissue and bone is large, with soft tissues all “squeezed” together at one end of the scale. CAXPCi could provide a solution to this problem as it can provide high contrast of soft tissue also in the vicinity of bones. For this application, not only is high image contrast required, but also good spatial resolution, as the size of the structures imaged is typically very small. Figure 7.2 shows an image of a mouse obtained in the absorption mode (a) and with CAXPCi (b). The phase contrast images

where obtained at an x-ray Mo spectrum of 40kV and with a current of 25mA. The pixel illuminated fraction was set to 50%. The absorption mode was obtained with the same x-ray spectrum but with a current of 10mA. In the absorption mode, the sample was also moved as close as possible to the detector surface to avoid possible FSP XPCi effects, however weak. In both modes, ten images were taken at each of eight dithering steps.

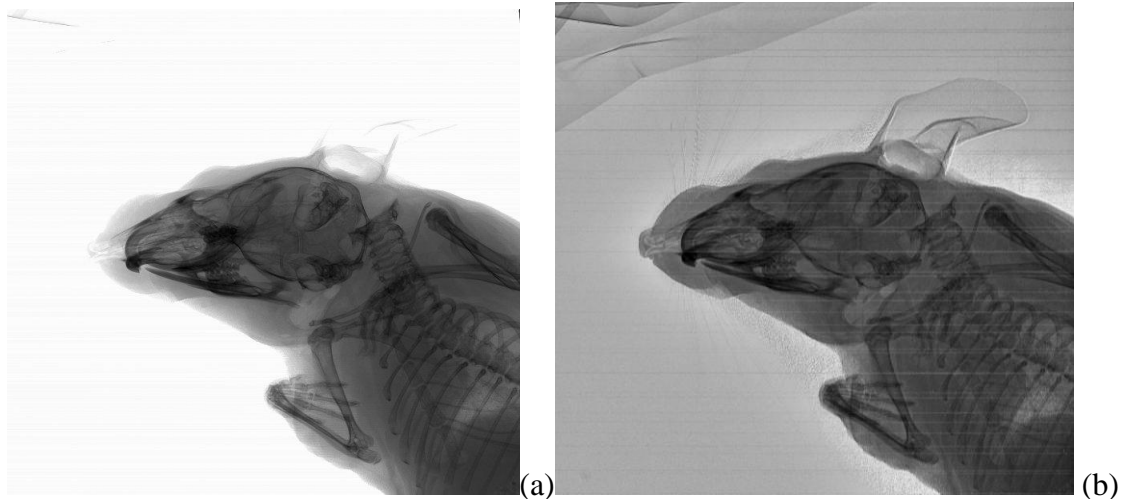


Figure 7.2 Absorption image (a) and phase contrast image of a mouse (b)

Figure 7.3 shows a zoom up of the head. This shows clearly how the areas inside the head are better defined in the phase contrast image than in the absorption one. For example, in the phase contrast image the whiskers and the fur are visible, and many features are more clearly visible such as for example the details of the hearing apparatus.

Also in small animal imaging, if combined with TS, not only can CAXPCi provide a high image contrast, but also depth information about the imaged sample. Figure 7.4 shows tomosynthesis slices through a mouse. The projections were acquired in 0.25° steps within an angular range of 25° . The setup used for the experiment was described previously in chapter 5. The reconstructed slices show different anatomical structures inside the mouse as we move through the volume (a-f). Moreover, the soft tissue structures are well defined. Particularly, the bright and dark fringes at the edges of the digestive apparatus and the bubbles inside it are clearly visible.

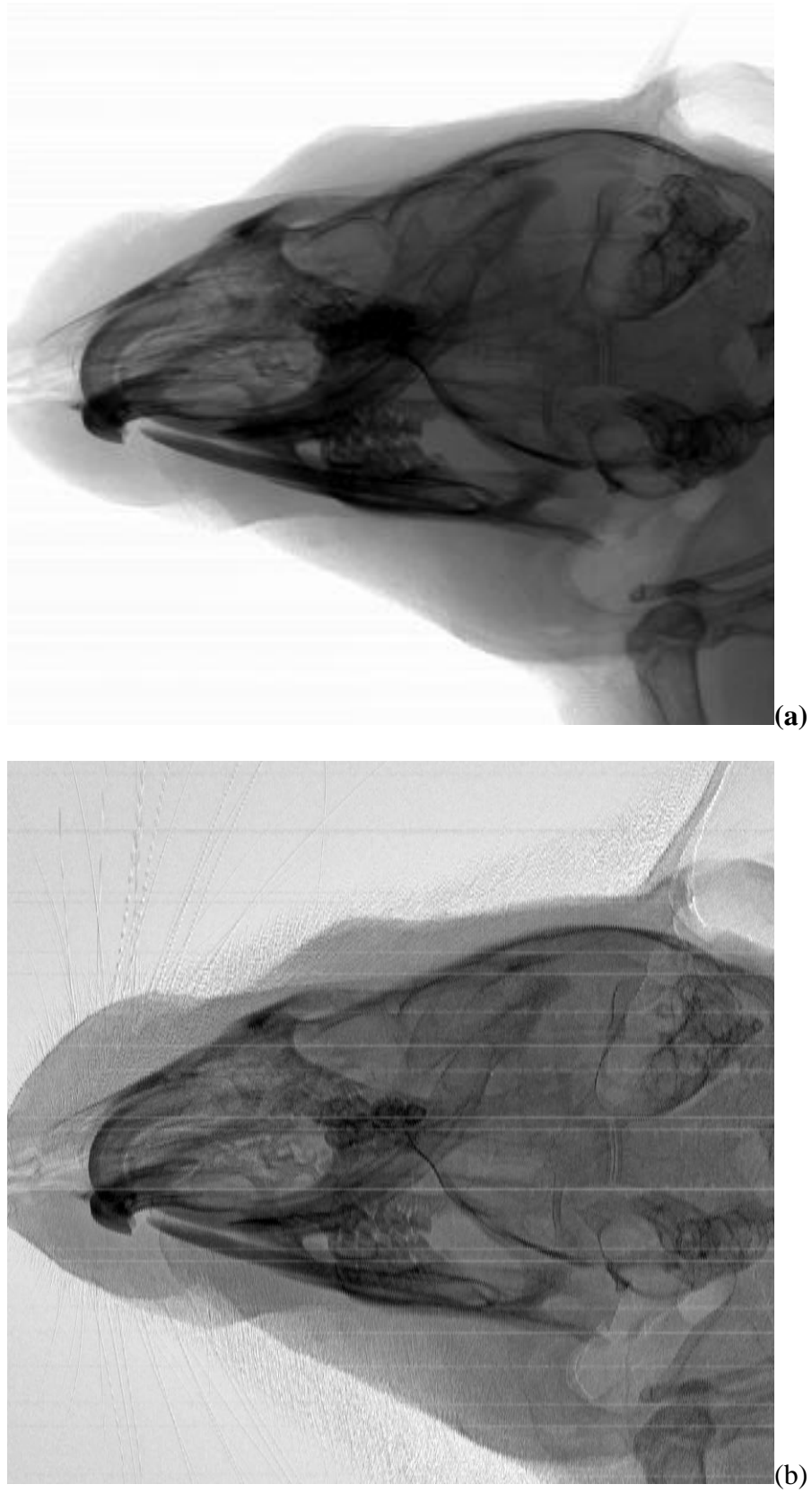


Figure 7.3 Head of the mouse acquired in the absorption mode (a) and in the phase contrast mode (b)

A number of studies exist, in which accurate soft tissue imaging is needed in the vicinity high absorbing structures (Langer et al. 2010). The proposed method could provide a solution to this problem in application to small animal imaging, due to the low delivered dose and relatively fast exposure times.

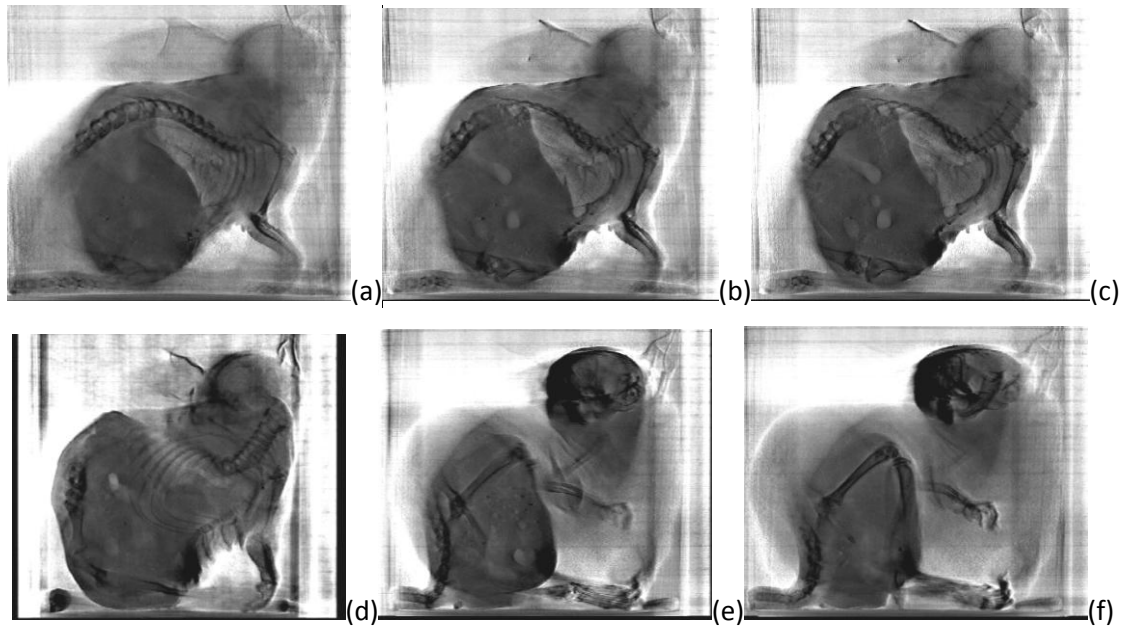


Figure 7.4 Phase contrast tomosynthesis reconstructions of a mouse.

Chapter 8

8 Summary and suggestions for the future work

8.1 Summary and key contribution to the field

In this work, a CAXPC Tomosynthesis technique was proposed. The principles of the CAXPCi method and a theoretical description of the tomosynthesis reconstruction methods used in this work have been given in chapter 2. Next, three different aspects of the implementation of CAXPC TS method were studied in detail: detector characterization, simulation of the CAXPCTS signal and its experimental verification, and the comparison of different reconstruction methods. Relatively complex phantoms like the “double” TORMAM phantom, breast tissue samples and small animals were imaged to show some possible applications of the method. The main contributions of this thesis to the medical imaging field are summarized below as well as my own input to this work.

8.1.1 Choice of the detector for CAXPC Tomosynthesis

The first step towards a fully working CAXPCi TS prototype system was the choice of the detector. This was an important step for two reasons. First, it has been previously shown (Olivo and Speller 2007; Ignatyev et al. 2011) how the choice between a direct and indirect conversion detector can have a major impact on the acquired phase contrast signal. Secondly, digital tomosynthesis requires a detector with fast acquisition and high spatial resolution. The detectors investigated in the study were: Anrad SMAM, Dexela and Hamamatsu C9732DK. Along the x-ray characterization, which involved MTF, NPS and DQE measurements, the effect of the signal spill-out between adjacent pixels on the phase contrast signal was investigated. My personal contribution to this area of the investigation was to measure all of these parameters. For the calculations of the DQE values, a MATLAB code developed by Konstantinidis (Konstantinidis, 2011) used

and modified by me for the evaluation of three detectors tested, a Total Filtration Calculator from (Reilly, 1999) and a Spektr software from (Siewerdsen et al, 2004). The results showed that the indirect conversion detector from Dexela featured the best DQE at high frequencies, but was not the best one with respect to spatial resolution and signal spill-out. The Hamamatsu detector, which is also an indirect conversion system, had the worst performance. The direct conversion Anrad SMAM was eventually chosen for the CAXPC TS prototype mainly for two reasons. 1) It featured lower signal spill-out than the other two systems, which translates directly into better image contrast. 2) It also featured the highest spatial resolution, important in mammography and small animal imaging, and relatively fast acquisition.

8.1.2 CSetting-up the CAXPC Tomosynthesis system and dose measurements.

Once the detector was selected, the CAXPC Tomosynthesis system was set up. This entailed challenges like the alignment of the masks, which is made difficult by the small size of the apertures and the five possible degrees of freedom along which these have to be moved. This meant that a complete procedure of the mask alignment had to be developed and applied before each acquisition. Compared to standard planar imaging, the Tomosynthesis imaging required adding a rotation motor and two cradles for the alignment of the axis of rotation, as well as programming the image acquisition procedure. Moreover, exposures and MGD had to be measured for the new setup. For this task, I used three different dosimeters: an ion chamber, TLDs and a solid state detector. The exposure measured with the TLDs was read out by Clare Ovenden - a Medical Physics Technician at St Bartholomew's Hospital in London. The results showed that the MGD estimated a typical CAXPC Tomosynthesis scan is roughly three times larger than that from a conventional absorption-based tomosynthesis system.

8.1.3 Simulations of the phase contrast signal and their experimental verification

Two models were used to simulate the phase contrast signal in the CAXPCi system. My own contribution consisted in the extension of a 2D model from (Olivo and Speller 2007) to a 3D case. The results simulated with both models show a good agreement with the experimental data, demonstrating that two models can be used to effectively

simulate CAXPCi in a 3D geometry. A sample consisting of two overlapping wires was simulated, and these were effectively separated while preserving intense PC features on each reconstructed image layer. Finally, reconstructed XPC Tomosynthesis slices obtained from simulated data agreed well with their experimental correspondents. I had full responsibility for the simulations and acquisition of the data experimentally. In order to reconstruct the images I have used already developed software from Dexela Ltd that employs a statistical algorithm.

8.1.4 Imaging of complex samples

Strong PC was also observed in the reconstructed tomosynthesis slices of the “double” TORMAM phantom and in vitro breast tissues, providing a preliminary demonstration that the technique can work under mammographic conditions. Details which fully overlapped in the individual projections were separated without affecting the PC signal.

The new technique was also tested on the imaging of a small animal. Example results obtained on a mouse were presented in this thesis. Although these samples were more complex than the TORMAM phantoms, the phase contrast signal was still observed, and a clear separation of the overlapping structures was achieved. These results give a preliminary but already robust demonstration of the feasibility of CAXPCi based tomosynthesis.

The development of a significant TS phantom by overlapping two TORMAM phantoms, the imaging and reconstruction of this phantom and of the breast and small-animal samples were all my original contributions.

8.1.5 Comprehensive study of different reconstruction algorithms for the new method

Four different reconstruction techniques were tested on the images obtained with the CAXPCi based tomosynthesis: FBP, CG, penalized CG and SPS. In order to perform the FBP, I have used the built-in MATLAB function called iRadon. The SPS and penalized CG methods are used in two independent reconstruction software developed at Dexela Ltd. The CG algorithm was developed at the Centre of Medical Image Computing (CMIC) at UCL. After a brief introduction to the above software, I was able to use it for extensive testing on my simulated and experimental data. I have processed

the data and done the comparison of the four methods. The FBP preserved intense phase-induced edge enhancement, but at the price of high background noise. It was instead found that using iterative algorithms, which were however primarily designed for the reconstruction of absorption-based images, better CNR was achieved, but at the cost of a reduced image contrast due to the smoothing of the phase contrast peaks. The results of the ASF study showed that iterative algorithms were able to reduce out of plane artefacts in a much shorter in-depth distance than the analytical FBP method. An attempt to optimize the acquisition geometry was made by reducing the number of projections and by using a non-equiangular acquisition range. It was found that smaller number of projections led to worse image contrast and CNR in the reconstructed images, as well as to stronger ghosting artefacts. Promising results were obtained with the non equiangular acquisition scheme, where reducing the number of projections from 15 to 11 and only led to a small decrease in the CNR.

8.2 Future work

Although the technique presented in this work has great potential to improve conventional mammographic imaging, it is still very much at the proof-of-concept stage. Much work remains to be undertaken to transfer this method into clinical environment. Several suggestions for further work arise directly from the results described in this thesis.

First, it is clear that, in order for the proposed method to be clinically acceptable, larger and more complex samples must be imaged. At this early stage, proof-of-concept results on simple phantoms, small tissues and small animals were presented. This, however, is a part of larger project, in which progressively more complex and larger samples will be imaged. This implies some difficulties as far as a tomosynthesis implementation is concerned. Currently, the field of view is limited to 6cm x 6cm by the size of the masks. New, larger masks would be required to image bigger samples. Moreover, in order to reconstruct images of larger samples obtained in a cone-beam geometry, an FDK-type algorithm should be implemented and adapted to XPCi. In this work, a FBP method was used to reconstruct images as the cone-beam angle was not large enough to introduce considerable image artefacts. With larger samples, one would need to modify the reconstruction code, so that planes which are far from the optical axis could be restored

correctly. However, the three iterative methods used in this work were already optimised for the cone-beam geometry.

Other difficulties might be associated with scanning thicker samples with the current setup. The samples imaged so far, at Mo spectrum at 40kVp and a current of 25mA, were about 3-5cm thick. Good results were obtained and the phase contrast signal was clearly visible in the projections. These settings should be sufficient to image a breast with a standard thickness of 4.5cm. For thicker breasts, sufficient x-ray flux would not be guaranteed by the present setup. It should also be noted that, in CAXPCi part of the beam is absorbed in the masks (the exact amount depending on the illumination level dictated by the masks misalignment).

The results of a comparison study of four different reconstruction algorithms showed that iterative methods designed for the reconstruction of absorption images do not fully restore the phase contrast signal. This is due to the fact that they aim at smoothing the noise, which can sometimes be mistaken for the phase contrast signal. A new definition of priors would therefore be needed for phase contrast imaging.

One current downside of the use of phase contrast imaging in a clinical environment is the acquisition time. With the current setup, a full tomosynthesis scan time is about 1.5 minutes, assuming 15 projections are used. Although this is the shortest time compared to other non-synchrotron phase contrast methods, it is still long for clinical use. More work on the x-ray source is required to reduce the acquisition time, and more optimization work to reduce the dose.

The results of detectors characterization showed that the systems currently available on the market all suffer from signal spill-out between pixels. The higher this spill-out, the smaller the difference between positive and negative peaks in the phase contrast signal, i.e. the image contrast. It has been found that indirect conversion detectors suffer more from this effect, because light scattering in the scintillator used to convert the x-rays into visible light. The design of a dedicated structured scintillator could solve this problem. Also, the detector mask in the real-world system could be incorporated in the detector itself, for an easier alignment procedure requiring the handling of less optical elements.

References

"Total Filtration Calculator." from

<http://www.dundee.ac.uk/medphys/RadTools/FiltrationCalc.html>.

Arfelli, F., Assante, M., Bonvicini, V., Bravin, A., Cantatore, G., Castelli, E., Dalla Palma, L., Di Michiel, M., Longo, R., Olivo, A., Pani, S., Pontoni, D., Poropat, P., Prest, M., Rashevsky, A., Tromba, G., Vacchi, A., Vallazza, E. and Zanconati, F. (1998), "Low-dose phase contrast x-ray medical imaging", *Physics in Medicine and Biology* **43** (10), pp. 2845-2852.

Arfelli, F., Abrami, A., Bregant, P., Chenda, V., Cova, M. A., de Guarrini, F., Dreossi, D., Longo, R., Menk, R. H., Quai, E., Rokvic, T., Tonutti, M., Tromba, G., Zanconati, F. and Castelli, E. (2007), "Synchrotron radiation mammography: Clinical experimentation", *Synchrotron Radiation Instrumentation, Pts 1 and 2* **879**, pp. 1895-1898.

Arhatari, B. D., Nugent, K. A., Peele, A. G. and Thornton, J. (2005), "Phase contrast radiography. II. Imaging of complex objects", *Review of Scientific Instruments* **76** (11).

Arridge, S. R., Schweiger, M., Hiraoka, M. and Delpy, D. T. (1993), "Performance of an Iterative Reconstruction Algorithm for near-Infrared Absorption and Scatter Imaging", *Proceedings of Photon Migration and Imaging in Random Media and Tissues* **1888**, pp. 360-371.

Berghammer, P., Obwegeser, R. and Sinzinger, H. (2001), "Nuclear medicine and breast cancer: a review of current strategies and novel therapies", *Breast* **10** (3), pp. 184-197.

Beutel, J. K., Harold L.; Van Metter, Richard L. (2000). Handbook of Medical Imaging, Volume 1 - Physics and Psychophysics, SPIE.

Bick, U. and Diekmann, F. (2010). Digital Mammography. Berlin Heidelberg, Springer.

Blake, P., Lawinski, C., Mackenzie, A., Honey, I., Cole, H. and Emerton, D. (2006). Report 05078 - Full Field Digital Mammography Systems – Hologic Selenia - a technical report.

Bohndiek, S. E., Blue, A., Clark, A. T., Prydderch, M. L., Turchetta, R., Royle, G. J. and Speller, R. D. (2008), "Comparison of Methods for Estimating the Conversion Gain of CMOS Active Pixel Sensors", *IEEE Sensors Journal* **8** (9-10), pp. 1734-1744.

Bohndiek, S. E., Cook, E. J., Arvanitis, C. D., Olivo, A., Royle, G. J., Clark, A. T., Prydderch, M. L., Turchetta, R. and Speller, R. D. (2008), "A CMOS active pixel sensor system for laboratory-based x-ray diffraction studies of biological tissue", *Physics in Medicine and Biology* **53** (3), pp. 655-672.

Bonse, U. and Hart, M. (1965), "An X-Ray Interferometer", *Applied Physics Letters* **6** (8), pp. 155-&.

Boone, J. M. and Seibert, J. A. (1997), "Accurate method for computer-generating tungsten anode x-ray spectra from 30 to 140 kV", *Medical Physics* **24** (11), pp. 1661-1670.

Boone, J. M. (1998), "Spectral modeling and compilation of quantum fluence in radiography and mammography", *Proceedings of SPIE* **3336**, pp. 592-601.

Boone, J. M. (1999), "Glandular breast dose for monoenergetic and high-energy X-ray beams: Monte Carlo assessment", *Radiology* **213** (1), pp. 23-37.

Boone, J. M., Kwan, A. L. C., Yang, K., Burkett, G. W., Lindfors, K. K. and Nelson, T. R. (2006), "Computed tomography for imaging the breast", *Journal of Mammary Gland Biology and Neoplasia* **11** (2), pp. 103-111.

Born, M. and Wolf, E. (1980). Principles of optics: Electromagnetic theory of propagation, interference and diffraction of light. Oxford and New York, Pergamon Press.

Bourne, R. (2010), "Fundamentals of Digital Imaging in Medicine", *Fundamentals of Digital Imaging in Medicine*, pp. 1-200.

Bovi, M., Laitano, R. F., Pimpinella, M., Toni, M. P., Casarin, K., Quail, E., Tromba, G., Vacotto, A. and Dreossi, D. (2007). Absolute air-kerma measurement in a synchrotron light beam by ionization free-air chamber. Paris.

Bruyant, P. P. (2002), "Analytic and iterative reconstruction algorithms in SPECT", *Journal of Nuclear Medicine* **43** (10), pp. 1343-1358.

Carr, J. C., Beatson, R. K., Cherrie, J. B., Mitchell, T. J., Fright, W. R., McCallum, B. C. and Evans, T. R. (2001), "Reconstruction and representation of 3D objects with Radial Basis Functions", *Siggraph 2001 Conference Proceedings*, pp. 67-76.

Cassano, E., Rizzo, S., Bozzini, A., Menna, S. and Bellomi, M. (2006), "Contrast enhanced ultrasound of breast cancer", *Cancer Imaging* **6**, pp. 4-6.

Castelli, E., Arfelli, F., Dreossi, D., Longo, R., Rokvic, T., Cova, M. A., Quaia, E., Tonutti, M., Zanconati, F., Abrami, A., Chenda, V., Menk, R. H., Quai, E., Tromba, G., Bregant, P. and de Guarrini, F. (2007), "Clinical mammography at the SYRMEP beam line", *Nuclear Instruments & Methods in Physics Research Section a-Accelerators Spectrometers Detectors and Associated Equipment* **572** (1), pp. 237-240.

Castelli, E., Tonutti, M., Arfelli, F., Longo, R., Quaia, E., Rigon, L., Sanabor, D., Zanconati, F., Dreossi, D., Abrami, A., Quai, E., Bregant, P., Casarin, K., Chenda, V., Menk, R. H., Rokvic, T., Vascotto, A., Tromba, G. and Cova, M. A. (2011), "Mammography with Synchrotron Radiation: First Clinical Experience with Phase-Detection Technique", *Radiology* **259** (3), pp. 684-694.

Chapman, D., Thomlinson, W., Johnston, R. E., Washburn, D., Pisano, E., Gmur, N., Zhong, Z., Menk, R., Arfelli, F. and Sayers, D. (1997), "Diffraction enhanced x-ray imaging", *Physics in Medicine and Biology* **42** (11), pp. 2015-2025.

Cherepenin, V., Karpov, A., Korjenevsky, A., Kornienko, V., Mazaletskaya, A., Mazourov, D. and Meister, D. (2001), "A 3D electrical impedance tomography (EIT) system for breast cancer detection", *Physiological Measurement* **22** (1), pp. 9-18.

Chotas, H. G., Dobbins, J. T. and Ravin, C. E. (1999), "Principles of digital radiography with large-area, electronically readable detectors: A review of the basics", *Radiology* **210** (3), pp. 595-599.

Cloetens, P., Ludwig, W., Baruchel, J., Van Dyck, D., Van Landuyt, J., Guigay, J. P. and Schlenker, M. (1999), "Holotomography: Quantitative phase tomography with micrometer resolution using hard synchrotron radiation x rays", *Applied Physics Letters* **75** (19), pp. 2912-2914.

Cong, W. X., Chen, N. X. and Gu, B. Y. (1999), "Phase retrieval in the Fresnel transform system: a recursive algorithm", *Journal of the Optical Society of America a-Optics Image Science and Vision* **16** (7), pp. 1827-1830.

Dainty, J. C. (1976). *Image science: principles, analysis and evaluation of photographic-type imaging processes*.

Dance, D. R., Baker, A. M., Davis, R. and Stacey, A. J. (1980), "Monte-Carlo Calculation of Absorbed Dose in Xeromammography", *Physics in Medicine and Biology* **25** (4), pp. 760-760.

Dance, D. R. (1990), "Monte-Carlo Calculation of Conversion Factors for the Estimation of Mean Glandular Breast Dose", *Physics in Medicine and Biology* **35** (9), pp. 1211-1219.

Dance, D. R., Skinner, C. L., Young, K. C., Beckett, J. R. and Kotre, C. J. (2000), "Additional factors for the estimation of mean glandular breast dose using the UK mammography dosimetry protocol", *Physics in Medicine and Biology* **45** (11), pp. 3225-3240.

Dance, D. R., Young, K. C. and van Engen, R. E. (2009), "Further factors for the estimation of mean glandular dose using the United Kingdom, European and IAEA breast dosimetry protocols", *Physics in Medicine and Biology* **54** (14), pp. 4361-4372.

Dance, D. R., Young, K. C. and van Engen, R. E. (2011), "Estimation of mean glandular dose for breast tomosynthesis: factors for use with the UK, European and IAEA breast dosimetry protocols", *Physics in Medicine and Biology* **56** (2), pp. 453-471.

Dilmanian, F. A., Zhong, Z., Ren, B., Wu, X. Y., Chapman, L. D., Orion, I. and Thomlinson, W. C. (2000), "Computed tomography of x-ray index of refraction using the diffraction enhanced imaging method", *Physics in Medicine and Biology* **45** (4), pp. 933-946.

Dobbins, J. T. and Godfrey, D. J. (2003), "Digital x-ray tomosynthesis: current state of the art and clinical potential", *Physics in Medicine and Biology* **48** (19), pp. R65-R106.

Douiri, A., Schweiger, M., Riley, J. and Arridge, S. (2005), "Local diffusion regularization method for optical tomography reconstruction by using robust statistics", *Optics Letters* **30** (18), pp. 2439-2441.

Dreossi, D., Abrami, A., Arfelli, F., Bregant, R., Casarin, K., Chenda, V., Cova, M. A., Longo, R., Menk, R. H., Quai, E., Quai, E., Rigon, L., Rokvic, T., Sanabor, D., Tonutti, M., Tromba, G., Vascotto, A., Zanconati, F. and Castelli, E. (2008), "The mammography project at the SYRMEP beamline", *European Journal of Radiology* **68** (3), pp. S58-S62.

EC (2006). European guidelines for quality assurance in breast cancer screening and diagnosis (fourth edn.), European Commission, Luxembourg, Office for Official Publications of the European Communities.

El Gamal, A. and Eltoukhy, H. (2005), "CMOS image sensors", *Circuits and Devices Magazine, IEEE* **21** (3), pp. 6 - 20

Erdogan, H. and Fessler, J. A. (1999), "Monotonic algorithms for transmission tomography", *Ieee Transactions on Medical Imaging* **18** (9), pp. 801-814.

Fantini, S., Heffer, E. L., Pera, V. E., Sassaroli, A. and Liu, N. (2005), "Spatial and spectral information in optical mammography", *Technology in Cancer Research & Treatment* **4** (5), pp. 471-482.

Feldkamp, L. A., Davis, L. C. and Kress, J. W. (1984), "Practical Cone-Beam Algorithm", *Journal of the Optical Society of America a-Optics Image Science and Vision* **1** (6), pp. 612-619.

Ferlay, J., Shin, H. R., Bray, F., Forman, D., Mathers, C. and Parkin, D. M. (2010), "Estimates of worldwide burden of cancer in 2008: GLOBOCAN 2008", *International Journal of Cancer* **127** (12), pp. 2893-2917.

Ferlay, J., Hery, C., Autier, P. and Sankaranarayanan, R. (2010), "Global Burden of Breast Cancer", *Breast Cancer Epidemiology*, pp. 1-19.

Fessler, J. A. and Erdogan, H. (1998). A Paraboloidal Surrogates Algorithm for Convergent Penalized-Likelihood Emission Image Reconstruction. IEEE Nuc.Sci.Symp. and Med. Im. Conf. **2**: 1132 - 1135.

Fiedler, S., Bravin, A., Keyrilainen, J., Fernandez, M., Suortti, P., Thomlinson, W., Tenhunen, M., Virkkunen, P. and Karjalainen-Lindsberg, M. L. (2004), "Imaging lobular breast carcinoma: comparison of synchrotron radiation DEI-CT technique with clinical CT, mammography and histology", *Physics in Medicine and Biology* **49** (2), pp. 175-188.

Forsberg, F., Piccoli, C. W., Merton, D. A., Palazzo, J. J. and Hall, A. L. (2007), "Breast lesions: Imaging with contrast-enhanced subharmonic US - Initial experience", *Radiology* **244** (3), pp. 718-726.

Fossum, E. R. (1997), "CMOS image sensors: Electronic camera-on-a-chip", *IEEE Transactions on Electron Devices* **44** (10), pp. 1689-1698.

Geman, S. and Geman, D. (1984), "Stochastic Relaxation, Gibbs Distributions, and the Bayesian Restoration of Images", *Ieee Transactions on Pattern Analysis and Machine Intelligence* **6** (6), pp. 721-741.

Gordon, R., Bender, R. and Herman, G. T. (1970), "Algebraic Reconstruction Techniques (Art) for 3-Dimensional Electron Microscopy and X-Ray Photography", *Journal of Theoretical Biology* **29** (3), pp. 471-&.

Greer, P. B. and van Doorn, T. (2000), "Evaluation of an algorithm for the assessment of the MTF using an edge method", *Medical Physics* **27** (9), pp. 2048-2059.

Groso, A., Stampanoni, M., Abela, R., Schneider, P., Linga, S. and Muller, R. (2006), "Phase contrast tomography: An alternative approach", *Applied Physics Letters* **88** (21).

Gureyev, T. E., Roberts, A. and Nugent, K. A. (1995), "Phase Retrieval with the Transport-of-Intensity Equation - Matrix Solution with Use of Zernike Polynomials", *Journal of the Optical Society of America a-Optics Image Science and Vision* **12** (9), pp. 1932-1941.

Gureyev, T. E. and Wilkins, S. W. (1998), "On x-ray phase imaging with a point source", *Journal of the Optical Society of America a-Optics Image Science and Vision* **15** (3), pp. 579-585.

Hendrick, R. E., Pisano, E. D., Averbukh, A., Moran, C., Berns, E. A., Yaffe, M. J., Herman, B., Acharyya, S. and Gatsonis, C. (2010), "Comparison of Acquisition Parameters and Breast Dose in Digital Mammography and Screen-Film Mammography in the American College of Radiology Imaging Network Digital Mammographic Imaging Screening Trial", *American Journal of Roentgenology* **194** (2), pp. 362-369.

Henke, B. L., Gullikson, E. M. and Davis, J. C. (1993), "X-ray Interactions - Photoabsorption, Scattering, Transmission and Reflection at E=50-30,000 EV, Z=1-92 (VOL 54, PG 181, 1993)", *Atomic Data and Nuclear Data Tables* **55** (2), pp. 349-349.

Holder, D. (2002), "Editorial: Biomedical applications of electrical impedance tomography", *Physiological Measurement* **23** (1).

Honey, I., Lawinski, C., Blake, P., Mackenzie, A., Cole, H. and Emerton, D. (2006). Report 06045 – Full Field Digital Mammography Systems Sectra MicroDose - A technical report.

Hsieh, Y. L., Gullberg, G. T., Zeng, G. L. and Huesman, R. H. (1996), "Image reconstruction using a generalized natural pixel basis", *Ieee Transactions on Nuclear Science* **43** (4), pp. 2306-2319.

Hsieh, Y. L., Gullberg, G. T., Zeng, G. L. and Huesman, R. H. (1996), "Fan beam image reconstruction using generalized natural pixel bases", *1995 Ieee Nuclear Science Symposium and Medical Imaging Conference Record, Vols 1-3*, pp. 1189-1192.

IAEA (2006). Dosimetry in diagnostic radiology: an international code of practice Technical Reports Series no 457 (Vienna: IAEA) Vienna: IAEA, International Atomic Energy Agency (IAEA); <http://www-pub.iaea.org/>

MTCD/publications/PDF/TRS457_web.pdf.

IAEA (2007). Dosimetry in Diagnostic Radiology: An International Code of Practice. IAEA.

IEC (2003). Medical electrical equipment – Characteristics of digital X-ray imaging devices – Part 1: Determination of the detective quantum efficiency. Geneva, Switzerland.

IEC (2007). 62220-1-2 Medical electrical equipment – Characteristics of digital X-ray imaging devices – Part 1-2:

Determination of the detective quantum efficiency – Detectors used in mammography. Geneva, Switzerland.

Ignatyev, K., Munro, P. R., Speller, R. D. and Olivo, A. (2011), "Effects of signal diffusion on x-ray phase contrast images", *Rev Sci Instrum* **82** (7), pp. 073702.

IPEM (2005). Recommended Standards for Routine Performance Testing of Diagnostic Imaging Equipment, IPEM Report 91, Institute of Physics and Engineering in Medicine.

Janesick, J. R. (2007). Photon transfer: $DN \rightarrow [\lambda]$.

Jang, B., Kaeli, D., Do, S. and Pien, H. (2009), "Multi Gpu Implementation of Iterative Tomographic Reconstruction Algorithms", *2009 Ieee International Symposium on Biomedical Imaging: From Nano to Macro, Vols 1 and 2*, pp. 185-188.

Johns, H. E. (1983). The physics of radiology.

Kak, A. C. and Slaney, M. (2001). Principles of computerized tomographic imaging. Philadelphia, Society for Industrial and Applied Mathematics.

Kang, K. J., Huang, Z. F., Zhu, P. P., Zhang, L. and Ieee (2009), "DEI-based Phase-contrast Tomosynthetic Experiment on Biological Samples with High Resolution X-ray CCD Camera", *2008 Ieee Nuclear Science Symposium and Medical Imaging Conference (2008 Nss/Mic), Vols 1-9*, pp. 726-729.

Knudsen, E. B., Prodi, A., Willendrup, P., Lefmann, K., Baltser, J., Gundlach, C., del Rio, M. S., Ferrero, C. and Feidenhans'l, R. (2011), "McXtrace: a modern ray-tracing package for x-ray instrumentation", *Advances in Computational Methods for X-Ray Optics II* **8141**.

Kolitsi, Z., Panayiotakis, G., Anastassopoulos, V., Scodras, A. and Pallikarakis, N. (1992), "A multiple projection method for digital tomosynthesis", *Medical Physics* **19** (4), pp. 1045-1050.

Konstantinidis, A. C., Szafraniec, M. B., Speller, R. D. and Olivo, A. (2012), "The Dexela 2923 CMOS X-ray detector: A flat panel detector based on CMOS active pixel sensors for medical imaging applications", *Nuclear Instruments & Methods in Physics Research Section a-Accelerators Spectrometers Detectors and Associated Equipment* **689**, pp. 12-21.

Kuhl, C. K., Schild, H. H. and Morakkabati, N. (2005), "Dynamic bilateral contrast-enhanced MR imaging of the breast: Trade-off between spatial and temporal resolution", *Radiology* **236** (3), pp. 789-800.

Lange, K. and Carson, R. (1984), "Em Reconstruction Algorithms for Emission and Transmission Tomography", *Journal of Computer Assisted Tomography* **8** (2), pp. 306-316.

Langer, M., Cloetens, P., Guigay, J. P. and Peyrin, F. (2008), "Quantitative comparison of direct phase retrieval algorithms in in-line phase tomography", *Medical Physics* **35** (10), pp. 4556-4566.

Langer, M., Boistel, R., Pagot, E., Cloetens, P. and Peyrin, F. (2010), "X-ray in-line phase microtomography for biomedical applications", *Microscopy: Science, Technology, Applications and Education* **1**, pp. 391-402.

Lazzari, B., Belli, G., Gori, C. and Del Turco, M. R. (2007), "Physical characteristics of five clinical systems for digital mammography", *Medical Physics* **34** (7), pp. 2730-2743.

Lewis, R. A., Hall, C. J., Hufton, A. P., Evans, S., Menk, R. H., Arfelli, F., Rigon, L., Tromba, G., Dance, D. R., Ellis, I. O., Evans, A., Jacobs, E., Pinder, S. E. and Rogers, K. D. (2003), "X-ray refraction effects: application to the imaging of biological tissues", *British Journal of Radiology* **76** (905), pp. 301-308.

Lewis, R. A. (2004), "Medical phase contrast x-ray imaging: current status and future prospects", *Physics in Medicine and Biology* **49** (16), pp. 3573-3583.

Longo, R., Pani, S., Arfelli, F., Dreossi, D., Olivo, A., Poropat, P., Quaia, E., Rigon, L., Zanconati, F., Dalla Palma, L. and Castelli, E. (2003), "Morphological breast imaging: tomography and digital mammography with synchrotron radiation", *Nuclear Instruments & Methods in Physics Research Section a-Accelerators Spectrometers Detectors and Associated Equipment* **497** (1), pp. 9-13.

Longo, R., Abrami, A., Arfelli, F., Bregant, P., Chenda, V., Cova, M. A., Dreossi, D., Guarrini, F., Menk, R. H., Quai, E., Quaia, E., Rokvic, T., Tonutti, M., Tromba, G., Zanconati, F. and Castelli, E. (2007), "Phase contrast mammography with synchrotron radiation: Physical aspects of the clinical trial", *Medical Imaging 2007: Physics of Medical Imaging, Pts 1-3* **6510**, pp. U282-U289.

Lynch, P. (2009). "www.patricklynch.net."

Maksimenko, A., Yuasa, T., Ando, M. and Hashimoto, E. (2007), "Refraction-based tomosynthesis: Proof of the concept", *Applied Physics Letters* **91** (23).

Marshall, N. W. (2006), "Retrospective analysis of a detector fault for a full field digital mammography system", *Physics in Medicine and Biology* **51** (21), pp. 5655-5673.

Martin, G., Martin, R., Brieva, M. J. and Santamaria, L. (2002), "Electrical impedance scanning in breast cancer imaging: correlation with mammographic and histologic diagnosis", *European Radiology* **12** (6), pp. 1471-1478.

Mertelmeier, T., Ludwig, J., Zhao, B. and Zhao, W. (2008), "Optimization of tomosynthesis acquisition parameters: Angular range and number of projections", *Digital Mammography, Proceedings* **5116**, pp. 220-227.

Miles N. Wernick, J. N. A. (2004). Emission Tomography: The Fundamentals of PET and SPECT. London, Elsevier Inc.

Millard, T. (2012). CAXPCi Dark Field Imaging. Department of Medical Physics and Bioengineering. London, University College London. **PhD**.

Momose, A. and Fukuda, J. (1995), "PHASE-CONTRAST RADIOGRAPHS OF NONSTAINED RAT CEREBELLAR SPECIMEN", *Medical Physics* **22** (4), pp. 375-379.

Momose, A., Takeda, T., Yoneyama, A., Koyama, I. and Itai, Y. (2001), "Wide-area phase-contrast X-ray imaging using large X-ray interferometers", *Nuclear Instruments & Methods in Physics Research Section a-Accelerators Spectrometers Detectors and Associated Equipment* **467**, pp. 917-920.

Monnin, P., Gutierrez, D., Bulling, S., Guntern, D. and Verdun, F. R. (2007), "A comparison of the performance of digital mammography systems", *Medical Physics* **34** (3), pp. 906-914.

Moy, J. P. and Bosset, B. (1999), "How does real offset and gain correction affect the DQE in images from X-ray flat detectors?", *Medical Imaging 1999: Physics of Medical Imaging, Pts 1 and 2* **3659**, pp. 90-97.

Mumcuoglu, E. U., Leahy, R. M., Zhou, Z. Y. and Cherry, S. R. (1996), "A phantom study of the quantitative behavior of Bayesian PET reconstruction methods", *1995 Ieee Nuclear Science Symposium and Medical Imaging Conference Record, Vols 1-3*, pp. 1703-1707.

Naday, S., Bullard, E. F., Gunn, S., Brodrick, J. E., Otuairisg, E. O., McArthur, A., Amin, H., Williams, M. B., Judy, P. G. and Konstantinidis, A. (2010), "Optimised Breast Tomosynthesis with a Novel CMOS Flat Panel Detector", *Digital Mammography* **6136**, pp. 428-435.

Niklason, L. T., Christian, B. T., Niklason, L. E., Kopans, D. B., Castleberry, D. E., OpsahlOng, B. H., Landberg, C. E., Slanetz, P. J., Giardino, A. A., Moore, R., Albagli, D., DeJule, M. C., Fitzgerald, P. F., Fobare, D. F., Giambattista, B. W., Kwasnick, R. F., Liu, J. Q., Lubowski, S. J., Possin, G. E., Richotte, J. F., Wei, C. Y. and Wirth, R. F. (1997), "Digital Tomosynthesis in breast imaging", *Radiology* **205** (2), pp. 399-406.

Olivo, A., Arfelli, F., Cantatore, G., Longo, R., Menk, R. H., Pani, S., Prest, M., Poropat, P., Rigon, L., Tromba, G., Vallazza, E. and Castelli, E. (2001), "An innovative digital imaging set-up allowing a low-dose approach to phase contrast applications in the medical field", *Medical Physics* **28** (8), pp. 1610-1619.

Olivo, A. and Speller, R. (2006), "Experimental validation of a simple model capable of predicting the phase contrast imaging capabilities of any x-ray imaging system", *Physics in Medicine and Biology* **51** (12), pp. 3015-3030.

Olivo, A. and Speller, R. (2007), "Modelling of a novel x-ray phase contrast imaging technique based on coded apertures", *Physics in Medicine and Biology* **52** (22), pp. 6555-6573.

Olivo, A. and Speller, R. (2007), "Polychromatic phase contrast imaging as a basic step towards a widespread application of the technique", *Nuclear Instruments & Methods in Physics Research Section a-Accelerators Spectrometers Detectors and Associated Equipment* **580** (2), pp. 1079-1082.

Olivo, A. and Speller, R. (2007), "A coded-aperture technique allowing x-ray phase contrast imaging with contrast imaging with conventional sources", *Applied Physics Letters* **91**.

Olivo, A., Chana, D. and Speller, R. (2008), "A preliminary investigation of the potential of phase contrast x-ray imaging in the field of homeland security", *Journal of Physics D-Applied Physics* **41** (22).

Olivo, A. and Speller, R. (2008), "Image formation principles in coded-aperture based x-ray phase contrast imaging", *Physics in Medicine and Biology* **53** (22), pp. 6461-6474.

Olivo, A., Ignatyev, K., Munro, P. R. and Speller, R. D. (2011), "Noninterferometric phase-contrast images obtained with incoherent x-ray sources", *Appl Opt* **50** (12), pp. 1765-1769.

Orel, S. G. and Schnall, M. D. (2001), "MR imaging of the breast for the detection, diagnosis, and staging of breast cancer", *Radiology* **220** (1), pp. 13-30.

Park, J. M., Franken, E. A., Garg, M., Fajardo, L. L. and Niklason, L. T. (2007), "Breast tomosynthesis: Present considerations and future applications", *Radiographics* **27**, pp. S231-S240.

Peterzol, A., Olivo, A., Rigon, L., Pani, S. and Dreossi, D. (2005), "The effects of the imaging system on the validity limits of the ray-optical approach to phase contrast imaging", *Medical Physics* **32** (12), pp. 3617-3627.

Pfeiffer, F., Weitkamp, T., Bunk, O. and David, C. (2006), "Phase retrieval and differential phase-contrast imaging with low-brilliance X-ray sources", *Nature Physics* **2** (4), pp. 258-261.

Pfeiffer, F., Kottler, C., Bunk, O. and David, C. (2007), "Hard X-ray phase tomography with low-brilliance sources", *Physical Review Letters* **98** (10).

Pisano, E. D. and Yaffe, M. J. (2005), "Digital mammography", *Radiology* **234** (2), pp. 353-362.

Pogany, A., Gao, D. and W., W. S. (1997), "Contrast and resolution in imaging with a microfocus x-ray source", *Rev. Sci. Instrum.* **68** (7), pp. 2774-2782.

Pogue, B. W., McBride, T. O., Prewitt, J., Osterberg, U. L. and Paulsen, K. D. (1999), "Spatially variant regularization improves diffuse optical tomography", *Applied Optics* **38** (13), pp. 2950-2961.

Price, B. D., Esbrand, C. J., Olivo, A., Gibson, A. P., Hebden, J. C., Speller, R. D. and Royle, G. J. (2008), "Assessing the validity of modulation transfer function evaluation techniques with application to small area and scanned digital detectors", *Review of Scientific Instruments* **79** (11), pp. 113103-113101-113103-113106.

Reilly, A. (1999). "<http://www.dundee.ac.uk/medphys/RadTools/FiltrationCalc.html>."

Rivetti, S., Lanconelli, N., Bertolini, M., Borasi, G., Golinelli, P., Acchiappati, D. and Gallo, E. (2009), "Physical and psychophysical characterization of a novel clinical system for digital mammography", *Medical Physics* **36** (11), pp. 5139-5148.

Rudin, L. I., Osher, S. and Fatemi, E. (1992), "Nonlinear Total Variation Based Noise Removal Algorithms", *Physica D* **60** (1-4), pp. 259-268.

Samei, E. and Flynn, M. J. (2002), "An experimental comparison of detector performance for computed radiography systems", *Medical Physics* **29** (4), pp. 447-459.

Schweiger, M. (2011), "GPU-Accelerated Finite Element Method for Modelling Light Transport in Diffuse Optical Tomography", *Int J Biomed Imaging* **2011**, pp. 403892.

Sechopoulos, I. and Ghetti, C. (2009), "Optimization of the acquisition geometry in digital tomosynthesis of the breast", *Med Phys* **36** (4), pp. 1199-1207.

Sehgal, C. M., Weinstein, S. P., Arger, P. H. and Conant, E. F. (2006), "A review of breast ultrasound", *Journal of Mammary Gland Biology and Neoplasia* **11** (2), pp. 113-123.

Shewchuk, C. F. and Morton, W. (1994), "The Evolution of an Online Model-Based Optimization System - It Offers a Valuable Tool for Process Design", *Pulp & Paper-Canada* **95** (6), pp. 29-34.

Siewerdsen, J. H., Waese, A. M., Moseley, D. J., Richard, S. and Jaffray, D. A. (2004), "Spektr: A computational tool for x-ray spectral analysis and imaging system optimization", *Medical Physics* **31** (11), pp. 3057-3067.

Snigirev, A., Snigireva, I., Kohn, V., Kuznetsov, S. and Schelokov, I. (1995), "On the possibilities of x-ray phase contrast microimaging by coherent high-energy synchrotron radiation", *Review of Scientific Instruments* **66** (12), pp. 5486-5492.

Sonka, M. F., J. Michael ((2009)). Handbook of Medical Imaging, Volume 2 - Medical Image Processing and Analysis., SPIE.

Tartar, M., Comstock, C. E. and Kipper, M. S. (2008). Breast cancer imaging : a multidisciplinary, multimodality approach. St. Louis, Mo. ; London, Mosby.

Thacker, S. C. and Glick, S. J. (2004), "Normalized glandular dose (DgN) coefficients for flat-panel CT breast imaging", *Physics in Medicine and Biology* **49** (24), pp. 5433-5444.

Tikhonov, A. N. (1963), "Regularization of Incorrectly Posed Problems", *Doklady Akademii Nauk SSSR* **153** (1), pp. 49-&.

Tromberg, B. J. (2005), "Optical scanning and breast cancer", *Academic Radiology* **12** (8), pp. 923-924.

Turbell, H. (2001). Cone-beam reconstruction using filtered backprojection, Linköping University. **PhD**.

Wang, J. Y., Zhu, P. P., Yuan, Q. X., Huang, W. X., Shu, H., Hu, T. D. and Wu, Z. Y. (2006), "Design and construction of an X-ray phase contrast CT system at BSRF", *Radiation Physics and Chemistry* **75** (11), pp. 1986-1989.

Wang, Z. T., Kang, K. J., Huang, Z. F., Zhang, L., Chen, Z. Q., Ding, F., Fang, Q. G. and Ieee (2009), "Differential phase-contrast tomosynthetic experimental system with weakly coherent hard X-rays", *2008 Ieee Nuclear Science Symposium and Medical Imaging Conference (2008 Nss/Mic), Vols 1-9*, pp. 3164-3166.

Weitkamp, T., Diaz, A., David, C., Pfeiffer, F., Stampanoni, M., Cloetens, P. and Ziegler, E. (2005), "X-ray phase imaging with a grating interferometer", *Optics Express* **13** (16), pp. 6296-6304.

Wilkins, S. W., Gureyev, T. E., Gao, D., Pogany, A. and Stevenson, A. W. (1996), "Phase-contrast imaging using polychromatic hard X-rays", *Nature* **384** (6607), pp. 335-338.

Wilkins, S. W., Gao, D., Gureyev, T., Pogany, A. and Stevenson, A. W. (1997), "X-ray phase-contrast radiography", *Radiology* **205**, pp. 907-907.

Williams, M. B., Krupinski, E. A., Strauss, K. J., Breeden, W. K., 3rd, Rzeszotarski, M. S., Applegate, K., Wyatt, M., Bjork, S. and Seibert, J. A. (2007), "Digital radiography image quality: image acquisition", *J Am Coll Radiol (Journal of the American College of Radiology)* **4** (6), pp. 371-388.

Wu, T., Moore, R. H., Rafferty, E. A. and Kopans, D. B. (2004), "A comparison of reconstruction algorithms for breast tomosynthesis", *Medical Physics* **31** (9), pp. 2636-2647.

Wu, T., Moore, R. H. and Kopans, D. B. (2006), "Voting strategy for artifact reduction in digital breast tomosynthesis", *Medical Physics* **33** (7), pp. 2461-2471.

Wu, X. and Liu, H. (2003), "A general theoretical formalism for X-ray phase contrast imaging", *Journal of X-Ray Science and Technology* **11** (1), pp. 33-42.

www.diamond.ac.uk.

Yang, G., Hipwell, J. H., Clarkson, M. J., Tanner, C., Mertzaniidou, T., Gunn, S., Ourselin, S., Hawkes, D. J. and Arridge, S. R. (2010). Combined reconstruction and registration of digital breast tomosynthesis: sequential method versus iterative method. Medical Image Understanding and Analysis (MIUA) 2010. University of Warwick, Coventry.

Yorker, J. G., Jeromin, L. S., Lee, D. L. Y., Palecki, E. F., Golden, K. P. and Jing, Z. X. (2002), "Characterization of a full field digital mammography detector based on direct x-ray conversion in selenium", *Medical Imaging 2002: Physics of Medical Imaging* **4682**, pp. 21-29.

Young, K., Strowig, M. and Mills, J. (2005), "Modelling of the effect of organ motion combined with field parameters on the received dose to a target region", *Radiotherapy & Oncology* **76**, pp. S156-S157.

Yu, D. F. and Fessler, J. A. (2002), "Edge-preserving tomographic reconstruction with nonlocal regularization", *Ieee Transactions on Medical Imaging* **21** (2), pp. 159-173.

Zhang, D., Donovan, M., Fajardo, L. L., Archer, A., Wu, X. Z. and Liu, H. (2008), "Preliminary feasibility study of an in-line phase contrast X-ray imaging prototype", *IEEE Transactions on Biomedical Engineering* **55** (9), pp. 2249-2257.

Zhang, X., Yang, X. R., Chen, Y., Li, H. Q., Liu, W. Y., Yuan, Q. X. and Chen, S. L. (2010), "Diffraction-Enhanced Radiography of Various Mouse Organs", *American Journal of Roentgenology* **195** (3), pp. 545-549.

Zhang, Y. H., Chan, H. P., Sahiner, B., Wei, J., Goodsitt, M. M., Hadjiiski, L. M., Ge, J. and Zhou, C. A. (2006), "A comparative study of limited-angle cone-beam reconstruction methods for breast tomosynthesis", *Medical Physics* **33** (10), pp. 3781-3795.

Zhao, B. and Zhao, W. (2008), "Three-dimensional linear system analysis for breast tomosynthesis", *Medical Physics* **35** (12), pp. 5219-5232.

Zhao, B. and Zhao, W. (2008), "Imaging performance of an amorphous selenium digital mammography detector in a breast tomosynthesis system", *Medical Physics* **35** (5), pp. 1978-1987.

Zhou, S. A. and Brahme, A. (2008), "Development of phase-contrast X-ray imaging techniques and potential medical applications", *Physica Medica* **24** (3), pp. 129-148.